

FORECASTING ATMOSPHERIC TURBULENCE CONDITIONS FROM PRIOR  
ENVIRONMENTAL PARAMETERS USING ARTIFICIAL NEURAL NETWORKS: AN  
ENSEMBLE STUDY

Thesis

Submitted to

The School of Engineering of the  
UNIVERSITY OF DAYTON

In Partial Fulfillment of the Requirements for

The Degree of

Master of Science in Electro-Optics and Photonics

By

Mitchell Gene Grose

Dayton, Ohio

May, 2021



FORECASTING ATMOSPHERIC TURBULENCE CONDITIONS FROM PRIOR  
ENVIRONMENTAL PARAMETERS USING ARTIFICIAL NEURAL NETWORKS: AN  
ENSEMBLE STUDY

Name: Grose, Mitchell Gene

APPROVED BY:

---

Edward A. Watson, Ph.D.  
Advisory Committee Chairman  
Graduate Faculty, Electro-Optics and  
Photonics

---

Vijayan K. Asari, Ph.D.  
Committee Member  
Professor, Electrical and Computer  
Engineering

---

Yakov Diskin, Ph.D.  
Committee Member  
Adjunct Professor, Electrical and  
Computer Engineering

---

Robert J. Wilkens, Ph.D., P.E.  
Associate Dean for Research and Innovation  
Professor  
School of Engineering

---

Eddy M. Rojas, Ph.D., M.A., P.E.  
Dean, School of Engineering

© Copyright by

Mitchell Gene Grose

All rights reserved

2021

## ABSTRACT

# FORECASTING ATMOSPHERIC TURBULENCE CONDITIONS FROM PRIOR ENVIRONMENTAL PARAMETERS USING ARTIFICIAL NEURAL NETWORKS: AN ENSEMBLE STUDY

Name: Grose, Mitchell Gene  
University of Dayton

Advisor: Dr. Edward A. Watson

Optical (atmospheric) turbulence ( $C_n^2$ ) is a highly stochastic process that can apply many adverse effects on imaging and laser propagation systems. Modeling atmospheric turbulence conditions has been proposed by physics-based models but they are unable to capture the many cases. Recently, machine learning surrogate models have been used to learn the relationship between local environmental (weather) and turbulence conditions. These models predict a turbulence strength at time  $t$  from weather at time  $t$ . This thesis proposes a technique to forecast four hours of future turbulence conditions at 30-minute intervals from prior environmental parameters using artificial neural networks. First, local weather and turbulence measurements are formatted to pairs of input sequence and output forecast. Next, a grid search is performed to find the best combination of model architecture and training parameters. The architectures investigated are the Multilayer Perceptron (MLP) and three variants of the Recurrent Neural Network (RNN). Finally, the selected model is applied to the test dataset and analyzed. It is shown that the model has generally learned the relationship between prior environmental and future turbulence conditions.

This thesis is dedicated to my parents for their unconditional love and support.

## ACKNOWLEDGMENTS

First I would like to thank my advisor, Dr. Watson, for his patience and support of my interests.

I am grateful to my colleagues at MZA Associates Corporation for their support of my continuing education. I especially want to thank Dr. Matthew Whiteley, Dr. Yakov Diskin, and Dr. Jason Schmidt for mentoring me for nearly three years at the time of this thesis. I am a better scientist because of them.

I am also grateful to Dr. David Bromwich for first accepting me as an undergraduate research assistant. I'd like to recognize Dr. Sheng-Hung Wang for giving his time to work with me.

Finally, I'd like to thank Dr. Shawn Ryan from my undergraduate studies for first introducing me to research and continuing to provide thoughtful advice many years later.

## TABLE OF CONTENTS

ABSTRACT . . . . .	iii
DEDICATION . . . . .	iv
ACKNOWLEDGMENTS . . . . .	v
LIST OF FIGURES . . . . .	viii
LIST OF TABLES . . . . .	x
CHAPTER I. BACKGROUND AND PROBLEM STATEMENT . . . . .	1
1.1 Turbulence ( $C_n^2$ ) Background . . . . .	1
1.1.1 What is Turbulence ( $C_n^2$ )? . . . . .	1
1.1.2 State of Turbulence ( $C_n^2$ ) Modeling . . . . .	3
1.2 Thesis Overview . . . . .	5
1.2.1 Machine Learning Modeling Review (Ch. 2) . . . . .	5
1.2.2 Dataset (Ch. 3) . . . . .	5
1.2.3 Grid Search (Ch. 4) . . . . .	5
1.2.4 Test Dataset Model Evaluation (Ch. 5) . . . . .	6
1.2.5 Summary and Future Work (Ch. 6) . . . . .	6
CHAPTER II. MACHINE LEARNING MODELING REVIEW . . . . .	7
2.1 Fundamentals of Model Training and Testing . . . . .	7
2.2 Machine Learning Model Architectures . . . . .	8
2.2.1 Multilayer Perceptron . . . . .	8
2.2.2 Recurrent Neural Networks . . . . .	13
2.3 Recurrent Neural Network Cells . . . . .	15
2.3.1 Simple RNN . . . . .	15
2.3.2 LSTM-RNN . . . . .	16
2.3.3 GRU-RNN . . . . .	19
2.4 Full Architectures . . . . .	21
2.5 Optimization and the Loss Function . . . . .	24
2.6 Chapter Summary . . . . .	27
CHAPTER III. DATASET . . . . .	28
3.1 Measurement Collection Setup . . . . .	28
3.1.1 Weather Measurements . . . . .	28
3.1.2 Turbulence ( $C_n^2$ ) Measurements . . . . .	30
3.1.3 Spatial Relationship of Platforms and Target . . . . .	34
3.2 Data Preprocessing . . . . .	36
3.2.1 Filtering, Window-Averaging, and Interpolating . . . . .	36
3.2.2 Formatting into Sequences and Forecasts . . . . .	39
3.2.3 Final Data Preparations for Modeling . . . . .	41
3.3 Chapter Summary . . . . .	52
CHAPTER IV. GRID SEARCH . . . . .	53

4.1	Methodology . . . . .	53
4.2	Grid Search Results . . . . .	57
4.2.1	Results Sorting . . . . .	58
4.2.2	Statistical Significance . . . . .	60
4.3	Evaluation of Best Models . . . . .	64
4.3.1	Comparative Analysis . . . . .	64
4.4	Selection of the Best Model and Chapter Summary . . . . .	70
CHAPTER V. TEST DATASET MODEL EVALUATION . . . . .		72
5.1	GRU-RNN Test Dataset Performance Summary . . . . .	72
5.2	Daily $C_n^2$ Forecasts . . . . .	77
5.3	General Forecast Analysis . . . . .	83
5.4	Individual Forecast Analysis . . . . .	88
5.4.1	Examining 2020/08/09 18:00 EST . . . . .	88
5.4.2	Examining 2020/08/06 14:00 EST . . . . .	91
5.4.3	Examining 2020/08/05 16:00 EST . . . . .	92
5.5	Chapter Summary . . . . .	93
CHAPTER VI. SUMMARY AND FUTURE WORK . . . . .		95
6.1	Summary . . . . .	95
6.2	Future Work . . . . .	96
BIBLIOGRAPHY . . . . .		98

## LIST OF FIGURES

1.1 Effect of low-strength and high-strength $C_n^2$ conditions. . . . .	2
2.1 Simple example of machine learning model training. . . . .	7
2.2 Simple example of machine learning model testing. . . . .	8
2.3 Simple MLP (multi-layer perceptron) to predict $\log_{10}(C_n^2)$ from weather inputs. . . . .	9
2.4 Sigmoid ( $\sigma$ ), hyperbolic tangent (tanh), and Rectified Linear Unit (ReLU) activation functions. . . . .	12
2.5 Unrolled single-layer RNN . . . . .	13
2.6 Unrolled multi-layer RNN . . . . .	14
2.7 Multi-layer MLP architecture with multiple time steps of weather as inputs and eight forecasts of turbulence as outputs. . . . .	22
2.8 Single-layer RNN architecture with multiple time steps of weather as inputs and eight forecasts of turbulence as outputs. . . . .	23
2.9 Multi-layer RNN architecture with multiple time steps of weather as inputs and eight forecasts of turbulence as outputs. . . . .	23
2.10 Gradient descent of a trivial loss (cost) function . . . . .	25
2.11 Gradient descent of a nontrivial loss (cost) function . . . . .	26
3.1 Weather station deployment . . . . .	30
3.2 DELTA setup for and target view for collection of minute-by-minute $C_n^2$ measurements. . . . .	32
3.3 DELTA propagation path geometry . . . . .	33
3.4 Spatial relationship between the DELTA platform, Vantage Pro2 Plus (weather) platform, and the Y-Tower (DELTA) target. . . . .	34
3.5 DELTA image and $C_n^2$ confidences. . . . .	37
3.6 Sequence data as a function of time, parsed by train, validation, and test datasets drawn in black, blue, and red, respectively. . . . .	44

3.7	Sequence data in normalized histograms, parsed by the train, validation, and test datasets drawn in black, blue, and red, respectively. . . . .	47
3.8	Turbulence ( $C_n^2$ ) forecasts as a function of time and as a normalized histogram. The train, validation, and test datasets are drawn in black, blue, and red, respectively. . . . .	50
4.1	Grid search results. . . . .	58
4.2	<i>Welch's t-test</i> of the grid search results . . . . .	62
4.3	Best 10% and worst 10% variable sets. . . . .	67
5.1	GRU-RNN train and test loss curves of 10 models. . . . .	72
5.2	GRU-RNN daily summary performance: mean, standard deviation, and min/max.	74
5.3	GRU-RNN hourly summary performance: individual and average. . . . .	75
5.4	August 03 and 05 - 07 daily $C_n^2$ forecasts. . . . .	78
5.5	August 08 - 10 daily $C_n^2$ forecasts. . . . .	82
5.6	Scatter plots. . . . .	85
5.7	Average performance as a function of forecast length. . . . .	87
5.8	GRU-RNN performance analysis of the August 9th 18:00 EST forecast. . . . .	90
5.9	GRU-RNN performance analysis of the August 6th 14:00 EST forecast. . . . .	91
5.10	GRU-RNN performance analysis of the August 5th 16:00 EST forecast. . . . .	93

## LIST OF TABLES

3.1	Davis Instruments Vantage Pro2 Plus Weather Station Measurements . . . . .	29
4.1	Top GRU-RNN Model Parameters . . . . .	64
4.2	Top MLP Model Parameters . . . . .	65

# CHAPTER I

## BACKGROUND AND PROBLEM STATEMENT

### 1.1 Turbulence ( $C_n^2$ ) Background

#### 1.1.1 What is Turbulence ( $C_n^2$ )?

Optical (atmospheric) turbulence is caused by naturally occurring small variations in air temperature ( $< 1^\circ\text{C}$ ) which cause random variations in wind velocity (eddies) which we view as turbulent motion in the atmosphere. The temperature differences cause small differences in atmospheric density and therefore in refractive index. These index changes are moved around by the random variations in wind eddies and can accumulate to cause significant inhomogeneities in the index profile of the atmosphere which can cause the wavefront of a beam to significantly change in propagation. The effects are high spatial frequency beam spreading, low spatial frequency beam wander, and intensity variations (scintillation) [1]. Atmospheric turbulence strength is characterized by the refractive-index structure constant,  $C_n^2$  ( $m^{-2/3}$ ). Turbulence strength is highly variable with season, time of day, geographical location, altitude, and local weather patterns. Generally,  $C_n^2$  varies in value from  $1 \times 10^{-12}(m^{-2/3})$  (very strong) to  $1 \times 10^{-17}(m^{-2/3})$  (very weak).

Atmospheric turbulence can have many adverse affects on optics in imaging and laser systems. All imaging through a non-negligible distance of the Earth's atmosphere is impacted by atmospheric turbulence, leading to a blurring effect in an image. An example of this is shown in Figure 1.1. Both images in Figure 1.1 are of the same target on the same day but during low-strength turbulence (left) and high-strength turbulence (right) conditions. There are many developed and developing technologies which are highly impacted by atmospheric turbulence.



(a) Low-strength ( $C_n^2$ )

(b) High-strength ( $C_n^2$ )

Figure 1.1: Effect of low-strength and high-strength  $C_n^2$  conditions.

In imaging applications, the image degradation in Figure 1.1b due to strong turbulence can significantly impact feature extraction and target recognition. The twinkling of celestial objects in the night sky is also due to atmospheric turbulence. Observatories (astronomy) are frequently built at high altitude geographical locations in part to avoid light pollution, but also to reduce amount of turbulence degradation by shortening the distance the incoming light must propagate through the atmosphere. In laser propagation applications, the degradation of the wavefront can significantly reduce the power of the beam from a high energy laser (HEL) weapon system on the target, or disrupt the transfer of signal in optical communication.

Atmospheric turbulence is important to measure and model because its impact can be compensated with adaptive optics (AO). The strength of the atmospheric turbulence is proportional to the amount of adaptive optics compensation needed to correct for the

aberrations. Using astronomy as an example, the basic components of an adaptive optics system consists of a wavefront sampler, a wavefront sensor (WFS), a corrector such as a deformable mirror, and a control computer to perform real-time numerical calculations. Light from an astronomical object is captured by the optical system consisting of a telescope and imager (camera). Part of the light is sampled by the WFS and this data is sent to the computer to calculate the necessary corrections in the deformable mirror to sharpen the image [1]. A similar AO system exists for a laser propagation setup. Another application of the measurement of turbulence is when an optical system requires parameter tuning at a specific strength of turbulence. Finally, the use of a laser weapon system might be best for turbulence conditions weaker than a specific strength, so knowledge of the current conditions can decide whether to use the laser system or traditional weapons.

### 1.1.2 State of Turbulence ( $C_n^2$ ) Modeling

There is no theoretical (physical) model for turbulence which is accurate for the many cases, but many have been developed for specific cases. One such model is the Hufnagel-Valley boundary model that calculates  $C_n^2$  as a function of altitude [2]. Another is the submarine laser communications (SLC)-Night model which associates  $C_n^2$  strengths with specific altitude intervals [1].

Another approach to modeling turbulence ( $C_n^2$ ), specifically at the surface level, is by the use of machine learning. This approach acts as a surrogate model of the relationship between the local environmental (weather) and  $C_n^2$  conditions. Typical weather measurements are air temperature, pressure, relative humidity or dew point, wind speed and direction, and solar irradiance. The time-correlated atmospheric turbulence ( $C_n^2$ ) measurements are typically taken with a scintillometer [3, 4, 5]. The machine learning approach commonly employs the

Multilayer Perceptron (MLP) which is an Artificial Neural Network (ANN) optimized by a gradient descent algorithm [4, 5].

This type of approach associates a set of environmental (weather) measurements with a time-correlated  $C_n^2$  measurement and is most useful as a surrogate model to predict  $C_n^2$  for comparison with measurements. This technique illustrates the capability of a model, but its primary use is if current  $C_n^2$  measurements are desired but a sensor is not deployed. A more useful model *forecasts* future  $C_n^2$  instead of making predictions while measuring weather conditions. One approach to forecasting is to train a regression model on time-correlated weather and  $C_n^2$  measurements, then apply it to weather forecasts from a numerical weather prediction (NWP) data source to yield a  $C_n^2$  forecast.

The work in this thesis develops a novel machine learning approach to forecast future daytime  $C_n^2$  conditions from *prior* environmental (weather) and  $C_n^2$  measurements. Deep learning is used to create a low-altitude model capable of forecasting 4 hours of future daytime  $C_n^2$  conditions with estimates every 30 minutes using no more than 16 hours of prior environmental measurements. This technique is ideal for any application that uses near-term future  $C_n^2$  predictions and bypasses the need to download and format NWP data for model inference. Several major architectures including the Multilayer Perceptron and Recurrent Neural Network, multiple weather variables, and a small parameter space are explored in a grid search to find an effective combination.

All of the work in this thesis is done in Python with the exception of a few graphs made with Matlab. The modeling work uses PyTorch [6]. All code is available on GitHub at [https://github.com/mgrose31/cn2\\_forecast](https://github.com/mgrose31/cn2_forecast).

## 1.2 Thesis Overview

This section provides a brief chapter-by-chapter overview of the work in this thesis.

### 1.2.1 Machine Learning Modeling Review (Ch. 2)

Chapter II steps through a review of machine learning modeling. First, the basics of model training and testing is summarized. Next, the fundamental machine learning architectures used throughout this work are described in detail. Additionally, fundamental matrix math in applying the model to inputs is reviewed. Finally, a brief overview of optimization algorithms is presented.

### 1.2.2 Dataset (Ch. 3)

Chapter III first summarizes the weather and  $C_n^2$  data sources and their geographical relationship to each other. Chapter III then details the data preprocessing techniques including confidence filtering, window averaging, and interpolating. Finally presented is a description of the methodology to format the data into model input/output pairs and parse into train, validation, and test datasets.

### 1.2.3 Grid Search (Ch. 4)

Chapter IV details the grid search technique used to find the best architecture, input variables, and training parameters to best forecast  $C_n^2$ . A statistical test, the *Student's t-test*, is described then employed as a significance test of the grid search results. The top performing models in the grid search are then compared and a single model is selected.

#### 1.2.4 Test Dataset Model Evaluation (Ch. 5)

Chapter V first trains an ensemble of models to evaluate consistency of convergence. Then the model is applied to the test dataset to illustrates performance. This Chapter then details an analysis on the overall model performance to show general model capabilities. Finally an analysis of three specific forecasts is presented to evaluate why the model performs well and poorly in specific cases.

#### 1.2.5 Summary and Future Work (Ch. 6)

Chapter VI summarizes this thesis and details items for future work encountered throughout this effort.

## CHAPTER II

### MACHINE LEARNING MODELING REVIEW

This section first introduces the fundamentals of machine learning model training and testing, then details the fundamental architectures relevant to this work, and finally reviews the core components in model training.

#### 2.1 Fundamentals of Model Training and Testing

Figure 2.1 is a simple diagram of how a machine learning model iteratively improves from examples, a process called “training” or “learning.” Inputs and weights are sent into the model which applies the weights to the inputs to produce a result. The result is analyzed for performance, and based on the performance an update is applied to the weights which will improve model performance. This process is done iteratively until model performance

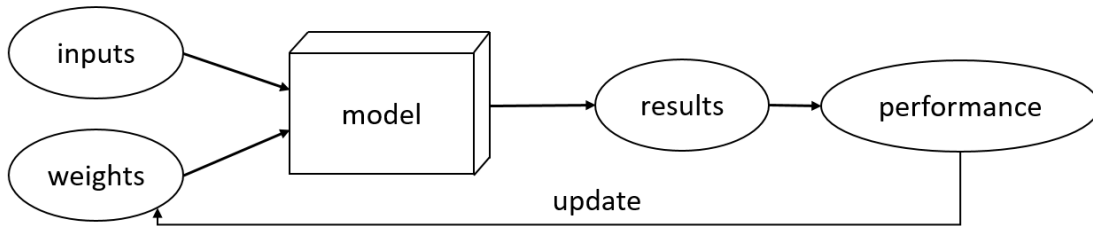


Figure 2.1: Simple example of machine learning model training.

stops improving, i.e., the model has converged to a solution. The final set of weights are the model’s trained, or learned, parameters. The modeling described is an example of “supervised learning” in which a set of inputs is associated with a known (truth) value

trying to be modeled. The performance analysis compares the model output with the truth value.

The trained model is then ready for testing, or inference, on another set of inputs. Figure 2.2 illustrates this process. The learned parameters from the training process are

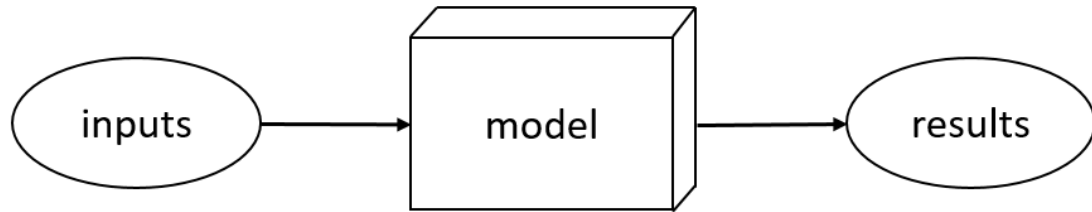


Figure 2.2: Simple example of machine learning model testing.

static in the model and are applied to the inputs to produce a result. The test inputs must be in the same format of the inputs used during training. While not required, it is highly desirable for the test inputs to be of similar magnitudes as the train inputs.

## 2.2 Machine Learning Model Architectures

The section reviews the fundamental architectures explored in this work: the Multilayer Perceptron and the Recurrent Neural Network. Additionally presented is a brief overview of how a model processes from input to output.

### 2.2.1 Multilayer Perceptron

The MLP is a feedforward ANN consisting of at least three layers of nodes: an input layer, a hidden layer, and an output layer. The number of hidden layers in an MLP is

adjustable to be greater than one. Each node in the MLP is a value, also called the node's activation. Each node in the input layer represents an input variable. Each node in the hidden and output layers represent the weighted sum of the activations from the previous layer. The MLP is described as "fully-connected" because each node in one layer connects with a specific weight  $w_{ij}$  to every node in the following layer.

Figure 2.3 is a simple 2-layer MLP for turbulence ( $C_n^2$ ) modeling. The input layer, which is not counted towards the depth (number of layers) of the neural network (NN), is five nodes wide. Each input node represents a weather variable measurement: temperature, pressure, relative humidity, wind speed, and solar irradiance. The input layer is fully-connected to

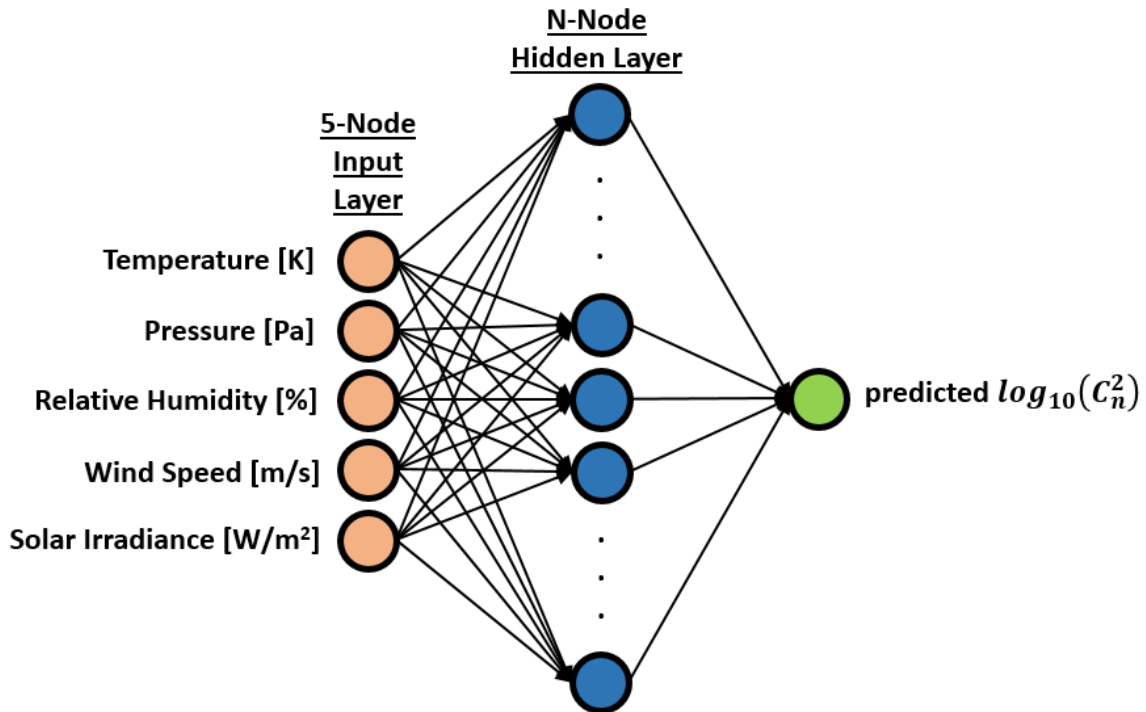


Figure 2.3: Simple MLP (multi-layer perceptron) to predict  $\log_{10}(C_n^2)$  from weather inputs.

the only hidden layer which is N-nodes wide. In application the researcher sets N. The

hidden layer is described as “hidden” because its nodes are buried in the model, i.e., are not part of the *inputs* or the *outputs*. The arrows from input layer to hidden layer in Figure 2.3 illustrate the concept of an MLP being fully-connected: an arrow points from each node in the input layer to each node in the hidden layer. This is further shown in the full connection between the hidden layer and output layer which has only a single node. The NN in Figure 2.3 is a single-output *regression* MLP because the output layer is a single node of *continuous* values. Specifically, the MLP in Figure 2.3 models the relationship between a set of weather inputs and  $\log_{10}C_n^2$  value. The other major NN type is *classification* which predicts/classifies *discrete* values or labels. Only regression NN is used in this work.

When fully-connected, the activations of a layer of nodes are calculated from the prior layer’s node activations by

$$\vec{y} = \sigma(\mathbf{W}\vec{x} + \vec{b}), \quad (2.1)$$

where  $\vec{x}$  is the input vector of prior layer node activations,  $\vec{y}$  is the output vector of next layer node activations,  $\mathbf{W}$  and  $\vec{b}$  are the learnable matrix weights and vector biases, and  $\sigma$  is a non-linear activation function. In matrix notation, Equation 2.1 for a 2-node layer fully-connected to another 2-node layer is written as

$$\begin{bmatrix} y_1 \\ y_2 \end{bmatrix} = \sigma \left( \begin{bmatrix} w_{1,1} & w_{1,2} \\ w_{2,1} & w_{2,2} \end{bmatrix} \begin{bmatrix} x_1 \\ x_2 \end{bmatrix} + \begin{bmatrix} b_1 \\ b_2 \end{bmatrix} \right). \quad (2.2)$$

The matrix-vector product  $\mathbf{W}\vec{x}$  is the weighted sum of the learnable weights and the input layer node activations. The notation of the weight matrix elements  $w_{ij}$  is such that  $i$  is the  $i^{th}$  node of the output layer and  $j$  is the  $j^{th}$  node of the input layer. The elements in the bias vector  $\vec{b}$  are similar to the constant  $b$  of a linear function

$$y = ax + b$$

that allows the model to best fit for the given data. The size of the learnable weight matrix ( $\mathbf{W}$ ) is [output size  $\times$  input size], and the size of the learnable bias vector ( $\vec{b}$ ) is [output size]. “Input size” is the number of nodes in the first layer, and “output size” is the number of nodes in the second layer.

The matrix-vector product of the weights and inputs and the addition of the bias vector are purely linear which constrains the model to learn only linear relationships. The  $\sigma$  in Equations 2.1 and 2.2 is a non-linear activation function applied element-wise to the values calculated from

$$\begin{bmatrix} w_{1,1} & w_{1,2} \\ w_{2,1} & w_{2,2} \end{bmatrix} \begin{bmatrix} x_1 \\ x_2 \end{bmatrix} + \begin{bmatrix} b_1 \\ b_2 \end{bmatrix}$$

to allow the model to learn non-linear relationships. The particular non-linear activation function  $\sigma$  is the sigmoid which squishes its argument between 0 (zero) and 1 by

$$\text{sigmoid}(x) = \sigma(x) = \frac{1}{1 + \exp(-x)}. \quad (2.3)$$

Figure 2.4a [6] illustrates the effect of the sigmoid activation function. Two additional activation functions used in this work are the hyperbolic tangent (tanh) defined as

$$\tanh(x) = \frac{\exp(x) - \exp(-x)}{\exp(x) + \exp(-x)}, \quad (2.4)$$

and the Rectified Linear Unit (ReLU) defined as

$$\text{ReLU}(x) = \max(0, x). \quad (2.5)$$

The tanh is similar to the sigmoid but is a smoother zero-centered activation function whose range lies between -1 and +1 as illustrated in Figure 2.4b. The ReLU is a piecewise linear function that returns a positive input as itself but returns 0 (zero) if the input is negative as shown in Figure 2.4c. The nearly linear ReLU preserves the properties of linear models that make them easy to optimize with gradient descent methods. The Recurrent Neural

Network (RNN) architectures explored in this work use the sigmoid and tanh activation functions, and the MLP architectures use the ReLU which is the most commonly used activation function in deep learning models. Details on the advantages and disadvantages of these activation functions are explored by Nwankpa et al [7].

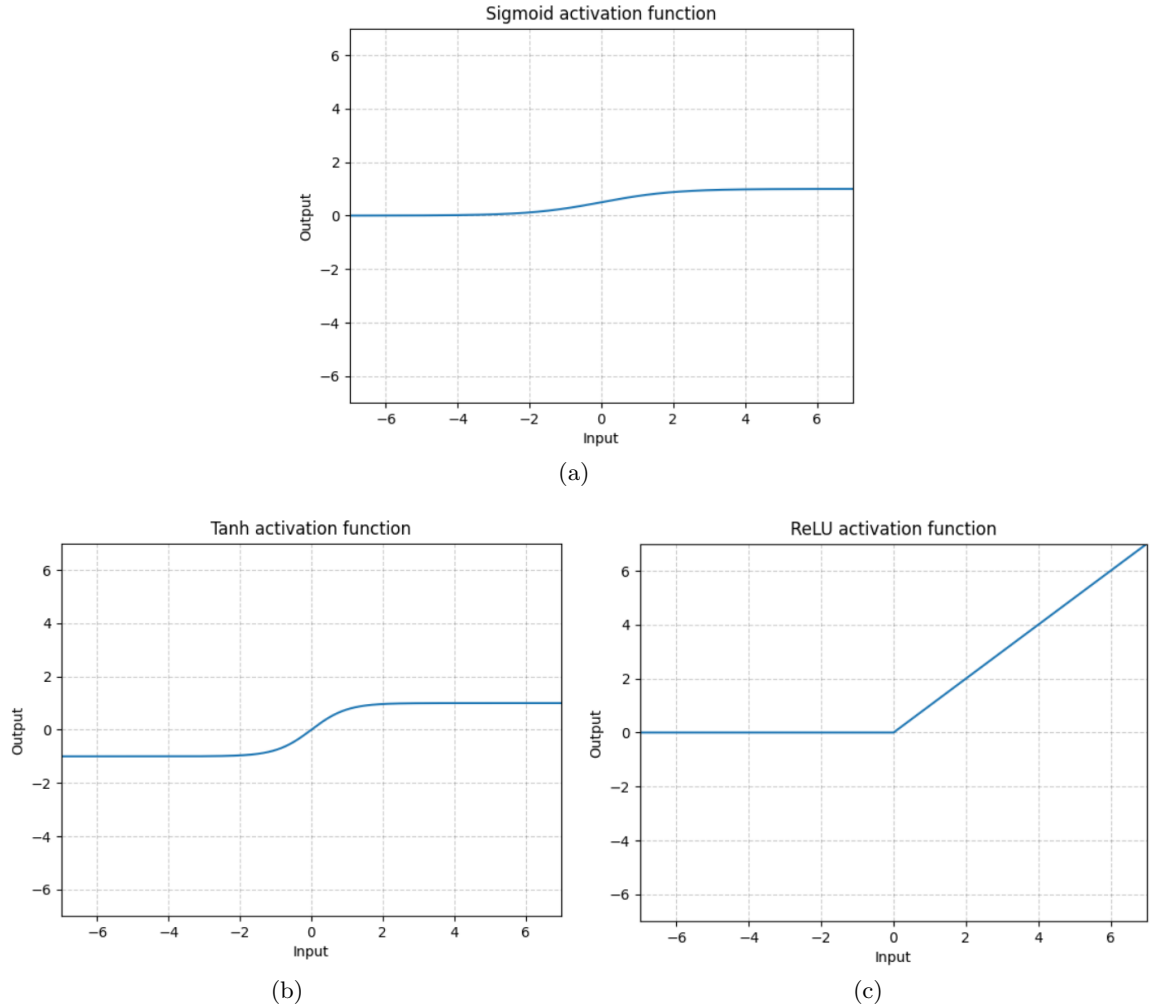


Figure 2.4: Sigmoid ( $\sigma$ ), hyperbolic tangent (tanh), and Rectified Linear Unit (ReLU) activation functions.

## 2.2.2 Recurrent Neural Networks

A RNN is an extension of a conventional feedforward neural network which is able to handle a variable-length sequence input. The RNN handles the variable-length sequence by having a recurrent hidden state whose activation (value) at each time is dependent on that of the previous time [8]. This processing is illustrated in Figure 2.5 where  $x_t$  is the set of inputs at time  $t$  and  $h_t$  is the resulting hidden state at time  $t$ . The left side of Figure 2.5 is the rolled version of the RNN processing and the right side is the unrolled version. At time

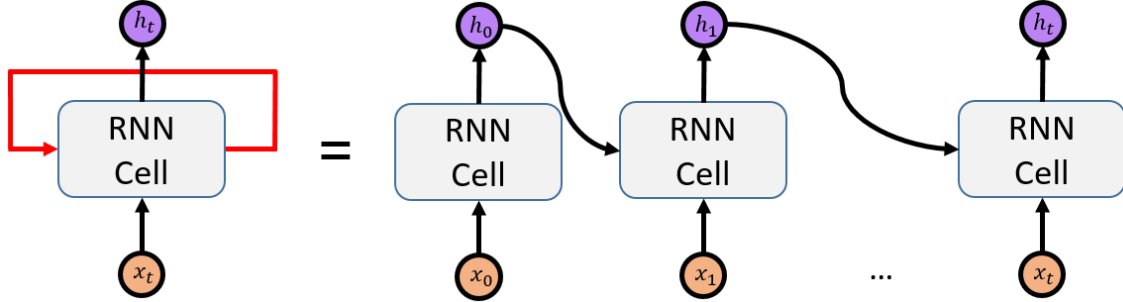


Figure 2.5: Unrolled single-layer RNN

$t = 0$  the inputs are fed into the RNN cell which calculates hidden state  $h_0$ . This hidden state is then fed into the RNN cell in combination with the inputs at time  $t = 1$  to calculate the hidden state  $h_1$ . This process continues until the final input of the time series  $x_t$  is sent into the RNN cell with hidden state  $h_{(t-1)}$  to calculate the final hidden state  $h_t$  which can be the model output or further manipulated in a more complex architecture. The internal processing of the RNN cell is discussed later.

The architecture in Figure 2.5 is a single-layer RNN that behaves similarly to the MLP in Figure 2.3 which has only a single hidden layer. More hidden layers are needed to add

complexity (depth) to the NN. Additional hidden layers in a RNN look like Figure 2.6. Like the single-layer RNN, the first layer of the multi-layer RNN processes prior hidden state  $h_{(t-1)}$  and current input  $x_t$  to hidden state  $h_t$ . After the inputs from each step

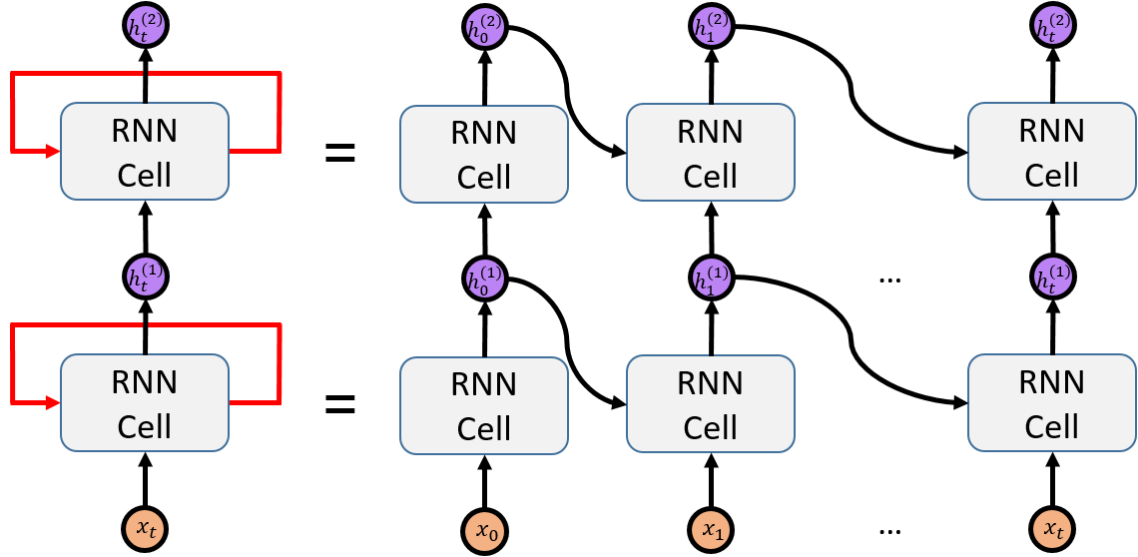


Figure 2.6: Unrolled multi-layer RNN

are processed the result is sent to the next layer. In this layer the processing is done in the exact same fashion but the inputs are now the hidden state at each time  $h_t$  from the prior layer instead of the input variables  $x_t$ . In the left of Figure 2.6 is the rolled version of the multi-layer RNN which shows  $x_t$  being repeatedly processed by the RNN cell to  $h_t^{(1)}$  which is the first-layer hidden state.  $h_t^{(1)}$  is then the input to the second layer RNN which processes the data to second-layer hidden state  $h_t^{(2)}$ . The right of Figure 2.6 is the unrolled version which further illustrates the multi-layer RNN processing.

## 2.3 Recurrent Neural Network Cells

There are many variants of the RNN cells in Figures 2.5 and 2.6 that process each time step of the input sequence. This thesis explores three of the cell variants: the simple (original) RNN, the Long Short-Term Memory RNN (LSTM-RNN), and the Gated Recurrent Unit RNN (GRU-RNN). The LSTM-RNN and GRU-RNN are two of the most widely used RNN cell variants.

### 2.3.1 Simple RNN

At each time step  $t$  the hidden state  $\vec{h}_t$  of the simple RNN is updated by

$$\vec{h}_t = \tanh \left( \mathbf{W}_{ih} \vec{x}_t + \vec{b}_{ih} + \mathbf{W}_{hh} \vec{h}_{(t-1)} + \vec{b}_{hh} \right) \quad (2.6)$$

where  $\tanh$  is the activation function that bounds the outputs from -1 to +1,  $\vec{x}_t$  is the input at time  $t$ ,  $\vec{h}_{(t-1)}$  is the hidden state at time  $t - 1$  or the initial state at time 0 (zero),  $\mathbf{W}_{ih}$  is the learnable input-hidden weights,  $\vec{b}_{ih}$  is the learnable input-hidden bias,  $\mathbf{W}_{hh}$  is the learnable hidden-hidden weights, and  $\vec{b}_{hh}$  is the learnable hidden-hidden bias. These learnable parameters are described as “shared through time” because the same parameters are applied to the inputs regardless of the time step of the input time series. Equation 2.6 and upcoming LSTM-RNN and GRU-RNN equations are PyTorch implementations [6].

According to PyTorch, the size of the learnable parameters goes as follows. The learnable input-hidden weights ( $\mathbf{W}_{ih}$ ) are of size [hidden size  $\times$  input size] for the single-layer RNN or first layer of the stacked RNN. The input-hidden weights are of size [hidden size  $\times$  hidden size] for the subsequent layers of the stacked RNN. The learnable hidden-hidden weights ( $\mathbf{W}_{hh}$ ) are of size [hidden size  $\times$  hidden size] for each layer of the RNN. The learnable input-hidden bias ( $\vec{b}_{ih}$ ) of each layer is of size [ $1 \times$  hidden size], and the learnable hidden-hidden bias ( $\vec{b}_{hh}$ )

of each layer is of size  $[1 \times \text{hidden size}]$ . Note that “input size” is the number of features (variables) in the input vector, and “hidden size” is the number of hidden nodes per RNN layer.

One significant issue with the simple RNN is its struggle to capture long-term dependencies because the gradients tend to either vanish or explode. Training an RNN with gradient-based optimization methods is a challenge because of the variations in gradient magnitudes and because the long-term dependencies are hidden by the effect of short-term dependencies [8]. The other variants explored in this work are designed to handle this vanishing/exploding gradient problem.

### 2.3.2 LSTM-RNN

The LSTM-RNN [9] deals with the vanishing/exploding gradient problem by proposing a new architecture and gradient-based learning algorithm. The LSTM-RNN can learn to bridge time intervals in excess of 1000 steps by utilizing a constant (neither vanishing nor exploding) error flow throughout the architecture. The core idea behind the LSTM-RNN is its *cell state* whose size is the number of hidden LSTM-RNN nodes specified by the researcher. The architecture removes or adds information to the cell state by the use of *gates*.

The first step in the LSTM-RNN is the forget gate  $\vec{f}_t$  which decides what information is thrown away or “forgotten” from the cell state. It combines the prior hidden state  $\vec{h}_{t-1}$  and the current input  $\vec{x}_t$  with learnable weights and biases  $\mathbf{W}_{if}$ ,  $\mathbf{W}_{hf}$ ,  $\vec{b}_{if}$ , and  $\vec{b}_{hf}$  in

$$\vec{f}_t = \sigma \left( \mathbf{W}_{if} \vec{x}_t + \vec{b}_{if} + \mathbf{W}_{hf} \vec{h}_{(t-1)} + \vec{b}_{hf} \right). \quad (2.7)$$

The non-linear activation function is the sigmoid which squishes the values inside from 0 (zero) to 1. An output of 1 indicates to completely keep the prior information and an output of 0 (zero) indicates to completely remove the prior information.

The next step in the LSTM-RNN combines the input gate  $\vec{i}_t$  and cell gate  $\vec{g}_t$  to determine what new information is passed into the cell state. The calculation of these gates is

$$\vec{i}_t = \sigma \left( \mathbf{W}_{ii} \vec{x}_t + \vec{b}_{ii} + \mathbf{W}_{hi} \vec{h}_{(t-1)} + \vec{b}_{hi} \right) \quad (2.8)$$

$$\vec{g}_t = \tanh \left( \mathbf{W}_{ig} \vec{x}_t + \vec{b}_{ig} + \mathbf{W}_{hg} \vec{h}_{(t-1)} + \vec{b}_{hg} \right), \quad (2.9)$$

where  $\mathbf{W}_{ii}$ ,  $\mathbf{W}_{hi}$ ,  $\mathbf{W}_{ig}$ , and  $\mathbf{W}_{hg}$  are the learnable weights and  $\vec{b}_{ii}$ ,  $\vec{b}_{hi}$ ,  $\vec{b}_{ig}$ , and  $\vec{b}_{hg}$  are the learnable biases. Like the forget gate, these learnable weights and biases are applied to the inputs  $\vec{x}_t$  and prior hidden state  $\vec{h}_{(t-1)}$ . The  $\sigma$  activation function around the input gate  $\vec{i}_t$  decides how much to update the cell state where a value of 1 indicates to completely update the cell state and a value of 0 does not update at all. The tanh activation around the cell gate  $\vec{g}_t$  squishes the values between -1 and +1 to be the new candidate node activations [10].

The input gate  $\vec{i}_t$  controls how much of the candidate node activations from cell gate  $\vec{g}_t$  are passed into the cell state  $C_t$  by

$$\vec{C}_t = \vec{f}_t \odot \vec{C}_{(t-1)} + \vec{i}_t \odot \vec{g}_t, \quad (2.10)$$

where  $\vec{f}_t$  is the forget gate that controls how much information is kept from the prior cell state  $\vec{C}_{(t-1)}$ , and  $\odot$  is element-wise multiplication. As an example, if the LSTM-RNN calculated to keep 25% of the prior cell state and update with 50% of the new candidate activations then Equation 2.10 would update the cell state by

$$\vec{C}_t = 0.25 \odot \vec{C}_{(t-1)} + 0.50 \odot \vec{g}_t.$$

The final calculation in the LSTM-RNN updates the hidden state  $\vec{h}_t$  by combining the updated cell state  $C_t$  with the output gate  $\vec{o}_t$  by

$$\vec{o}_t = \sigma \left( \mathbf{W}_{io} \vec{x}_t + \vec{b}_{io} + \mathbf{W}_{ho} \vec{h}_{(t-1)} + \vec{b}_{ho} \right) \quad (2.11)$$

$$\vec{h}_t = \vec{o}_t \odot \tanh \left( \vec{C}_t \right), \quad (2.12)$$

where  $\mathbf{W}_{io}$  and  $\mathbf{W}_{ho}$  are the learnable weights, and  $\vec{b}_{io}$  and  $\vec{b}_{ho}$  are the learnable biases. The output gate combines these learnable parameters with the input  $\vec{x}_t$  and prior hidden state  $\vec{h}_{(t-1)}$  then squishes them from 0 (zero) to 1 with the  $\sigma$  activation function. This gate controls how much of the updated cell state  $\vec{C}_t$  (squished between -1 and +1 with the tanh) is passed to the updated hidden state  $\vec{h}_t$ . A value of 0 (zero) for the output gate passes none of the cell state and a value of 1 passes everything from the cell state to the updated hidden state.

The calculations outlined in this section are performed in every step of the input time series. Like in the simple RNN, the learnable weights and biases are shared through time, i.e., they do not change between hidden state updates. According to PyTorch [6] the number of learnable parameters goes as follows. The learnable input-hidden weights ( $\mathbf{W}_{ii}$ ,  $\mathbf{W}_{if}$ ,  $\mathbf{W}_{ig}$ ,  $\mathbf{W}_{io}$ ) are of size  $[4 \times \text{hidden size} \times \text{input size}]$  in the first LSTM-RNN layer and  $[4 \times \text{hidden size} \times \text{hidden size}]$  in subsequent layers of a stacked LSTM-RNN. The learnable hidden-hidden weights ( $\mathbf{W}_{hi}$ ,  $\mathbf{W}_{hf}$ ,  $\mathbf{W}_{hg}$ ,  $\mathbf{W}_{ho}$ ) are of size  $[4 \times \text{hidden size} \times \text{hidden size}]$  in each layer of the LSTM-RNN. The learnable input-hidden bias of each LSTM-RNN layer ( $\vec{b}_{ii}$ ,  $\vec{b}_{if}$ ,  $\vec{b}_{ig}$ ,  $\vec{b}_{io}$ ) are of size  $[4 \times \text{hidden size}]$ , and the learnable hidden-hidden bias of each LSTM-RNN layer ( $\vec{b}_{hi}$ ,  $\vec{b}_{hf}$ ,  $\vec{b}_{hg}$ ,  $\vec{b}_{ho}$ ) are also of size  $[4 \times \text{hidden size}]$ . Note that the multiplication by 4 does not apply to each weight or bias, but rather accounts for the combined size of all the biases. So for example bias  $\vec{b}_{hi}$  is of size  $[1 \times \text{hidden size}]$ , but all four hidden-hidden biases are of combined size  $[4 \times \text{hidden size}]$ . “Hidden size” in this

context is the number of hidden nodes in the LSTM-RNN layer, and “input size” is the number of features (variables) of the input vector.

### 2.3.3 GRU-RNN

The last variant of the RNN cell is the GRU-RNN that is motivated by the LSTM-RNN but is much simpler to compute and implement [11]. Instead of incorporating a cell state like the LSTM-RNN, this cell architecture only applies updates to the hidden state. There are three gates in the GRU-RNN architecture that are more general than the LSTM-RNN gates: the reset gate  $\vec{r}_t$ , update gate  $\vec{z}_t$ , and the new gate  $\vec{n}_t$ .

The first calculation in the hidden state update for a single time step is the reset gate  $r_t$  computed by

$$\vec{r}_t = \sigma \left( \mathbf{W}_{ir} \vec{x}_t + \vec{b}_{ir} + \mathbf{W}_{hr} \vec{h}_{(t-1)} + \vec{b}_{hr} \right), \quad (2.13)$$

where  $\sigma$  is the sigmoid activation function, and  $\vec{x}_t$  and  $\vec{h}_{t-1}$  are the input and previous hidden state, respectively.  $\mathbf{W}_{ir}$  and  $\mathbf{W}_{hr}$  are the learnable input and hidden weight matrices, and  $\vec{b}_{ir}$  and  $\vec{b}_{hr}$  are the learnable input and hidden bias vectors.

Next, the update gate is computed by

$$\vec{z}_t = \sigma \left( \mathbf{W}_{iz} \vec{x}_t + \vec{b}_{iz} + \mathbf{W}_{hz} \vec{h}_{(t-1)} + \vec{b}_{hz} \right), \quad (2.14)$$

where  $\sigma$  is again the sigmoid activation function, and  $\vec{x}_t$  and  $\vec{h}_{t-1}$  are the input and previous hidden state, respectively.  $\mathbf{W}_{iz}$  and  $\mathbf{W}_{hz}$  are again the learnable input and hidden weight matrices, and  $\vec{b}_{iz}$  and  $\vec{b}_{hz}$  are the learnable input and hidden biases.

The proposed new hidden state is computed by

$$\vec{n}_t = \tanh \left( \mathbf{W}_{in} \vec{x}_t + \vec{b}_{in} + \vec{r}_t \odot \left( \mathbf{W}_{hn} \vec{h}_{(t-1)} + \vec{b}_{hn} \right) \right), \quad (2.15)$$

where  $\tanh$  is the activation function to range the values between -1 and +1, and  $\vec{x}_t$  and  $\vec{h}_{t-1}$  are the input and previous hidden state, respectively.  $\mathbf{W}_{in}$  and  $\mathbf{W}_{hn}$  are the learnable input and hidden weights, and  $\vec{b}_{in}$  and  $\vec{b}_{hn}$  are the learnable input and hidden biases.  $\vec{r}_t$  is the reset gate from Equation 2.13, and  $\odot$  is element-wise multiplication.

The hidden state passed through the cell is computed by

$$\vec{h}_t = (1 - \vec{z}_t) \odot \vec{n}_t + \vec{z}_t \odot \vec{h}_{(t-1)}, \quad (2.16)$$

where  $\vec{z}_t$  is the update gate,  $\vec{n}_t$  is the new gate,  $\vec{h}_{t-1}$  is the previous hidden state, and  $\odot$  is element-wise multiplication.

When the reset gate  $\vec{r}_t$  is close to 0 (zero), the hidden state is forced to ignore the previous hidden state and reset with the current input only. This effectively allows the hidden state to drop any information found to be irrelevant in the future. The update gate  $\vec{z}_j$  controls how much information from the previous hidden state carries over to the current hidden state and helps the network remember long-term information. Each node in the hidden GRU-RNN cell has separate reset and update gates, so each node learns to capture dependencies over different time scales. The nodes that learn short-term dependencies tend to have reset gates that are frequently active, but nodes that capture longer-term dependencies have update gates that are mostly active [11].

According to PyTorch [6] the number of learnable parameters goes as follows. The learnable input-hidden weights ( $\mathbf{W}_{ir}$ ,  $\mathbf{W}_{iz}$ ,  $\mathbf{W}_{in}$ ) are of size  $[3 \times \text{hidden size} \times \text{input size}]$  for the first layer and  $[3 \times \text{hidden size} \times \text{hidden size}]$  for subsequent layers in the stacked GRU-RNN. The learnable hidden-hidden weights ( $\mathbf{W}_{hr}$ ,  $\mathbf{W}_{hz}$ ,  $\mathbf{W}_{hn}$ ) in each layer are of size  $[3 \times \text{hidden size} \times \text{hidden size}]$ . The learnable input-hidden bias ( $\vec{b}_{ir}$ ,  $\vec{b}_{iz}$ ,  $\vec{b}_{in}$ ) of each layer are of size  $[3 \times \text{hidden size}]$ , and the learnable hidden-hidden bias ( $\vec{b}_{hr}$ ,  $\vec{b}_{hz}$ ,  $\vec{b}_{hn}$ ) of each

layer are of size  $[3 \times \text{hidden size}]$ . Like described for the LSTM-RNN, the multiplication by 3 is not for every weight and bias, but rather accounts for the combined size of all the weights or biases. “Input size” is the number of features (variable) in the input vector and “hidden size” is the number of hidden nodes per GRU-RNN layer.

## 2.4 Full Architectures

This section applies the fundamental architectures described in Section 2.2 to the problem addressed in this work. Described later as part of the data formatting in Chapter III and the grid search in Chapter IV, a time series (sequence) of weather variables is the input to the architectures and a time series of eight  $\log_{10}(C_n^2)$  forecast values is the output. The nodal representations of the MLP and RNN architectures applied specifically to turbulence forecasting are illustrated here.

Figure 2.7 illustrates a regression MLP with two hidden layers. The input is a flattened layer of weather variables at multiple time steps and is of size  $[N_t \times 6]$  where  $N_t$  is the number of time steps in the input sequence. The multiplication by 6 is for the number of input variables considered in this work. Thus, if 10 time steps of input variables are sent into the model, then the input layer is 60 nodes wide. The first 6 nodes are the first time step, the furthest away from the forecast. The last 6 nodes are the last time step, the closest time to the forecast. The output is a layer of eight nodes whose activations are eight time steps of measured  $\log_{10}(C_n^2)$  *after* the last time step in the input layer. The first node is the first time step in the forecast, the second node the second time step, and so on until the eighth node which is the eighth time step in the forecast. The ReLU activation function is applied to the nodes of each hidden layer, but not the output layer so the trained model is not bounded during inference.

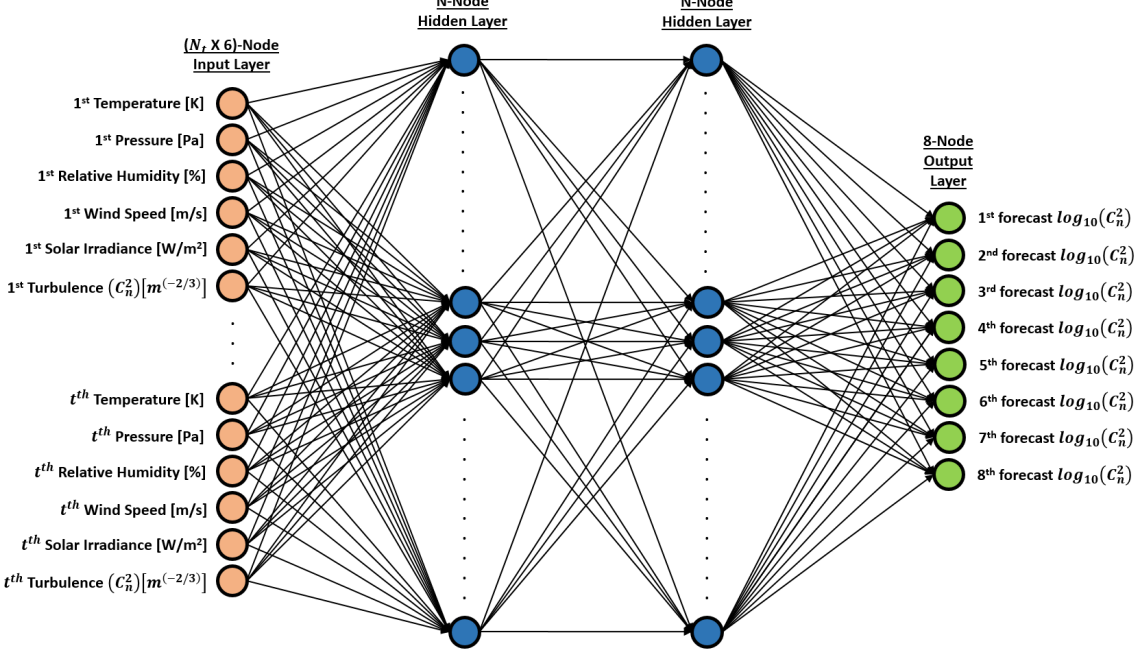


Figure 2.7: Multi-layer MLP architecture with multiple time steps of weather as inputs and eight forecasts of turbulence as outputs.

The flattening of input variables at multiple time steps to a single layer in the MLP removes all information about the temporal relationship between the nodes. The RNN architecture, however, preserves the temporal relationship of the model inputs as described above. Figure 2.8 illustrates a single-layer RNN architecture and how its final hidden state  $h_t$  is processed to predict the eight  $\log_{10}(C_n^2)$  forecasts. The input  $x_t$  is combined with the previous hidden state  $h_{t-1}$  to update the current hidden state  $h_t$  according to the type of RNN cell employed. The final hidden state is simply a single layer of N-nodes and is fully-connected to the eight nodes in the output layer like in the MLP. Throughout this manuscript, Figure 2.8 illustrates the exact architecture of an RNN model with a single hidden layer. Figure 2.9 illustrates the exact architecture when two hidden RNN layers are employed. Note that in Figures 2.8 and 2.9 the initial hidden state in the entire process is 0 (zero) as illustrated

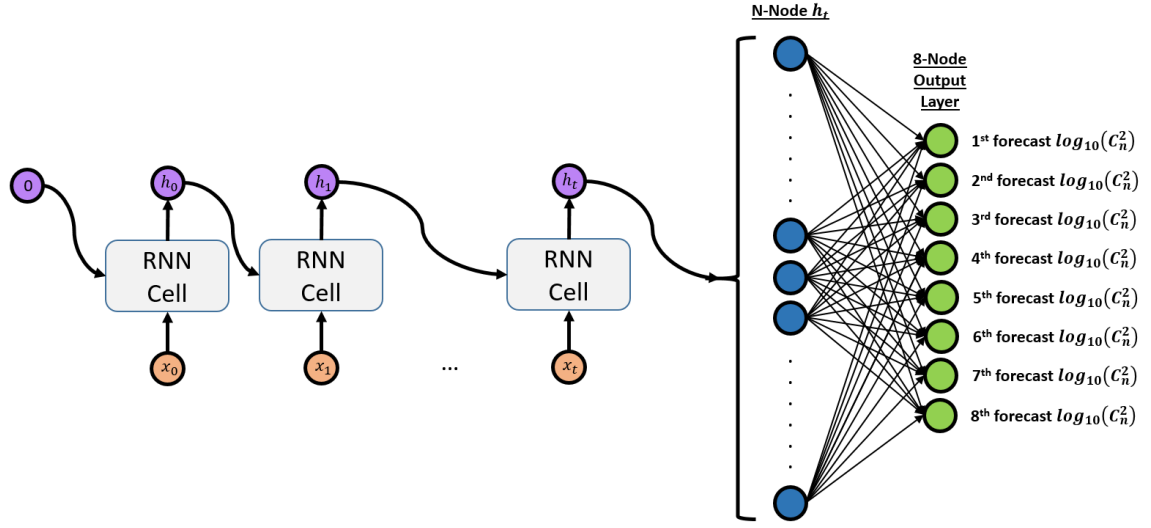


Figure 2.8: Single-layer RNN architecture with multiple time steps of weather as inputs and eight forecasts of turbulence as outputs.

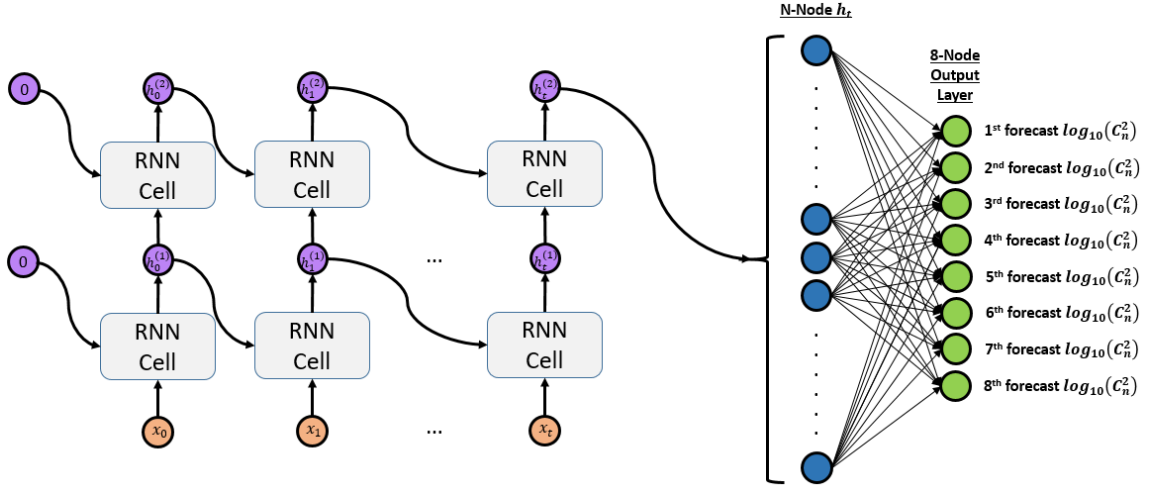


Figure 2.9: Multi-layer RNN architecture with multiple time steps of weather as inputs and eight forecasts of turbulence as outputs.

by the purple nodes on the far left of each Figure. This is the default behavior in PyTorch [6] and is used throughout this work. The RNN updating of the hidden state is considered

to be a “warming up” process to make a prediction at the end. In the application of the RNN architectures presented here,  $x_t = (\text{temp}, \text{press}, \text{rh}, \text{wind spd}, \text{solar irr}, \log_{10}(C_n^2))_t$ .

## 2.5 Optimization and the Loss Function

There are two steps in training a model. First is forward propagation in which the network makes a prediction by passing input values through the architecture and applying the learned parameters (weights and biases). The second step is backward propagation where the network adjusts its parameters according to their gradients (derivatives) with respect to the loss. The adjustment of the parameters is done by an optimization algorithm, the most common being gradient descent. Gradient descent is an algorithm used to find the values of the model parameters that minimizes the loss function (also called the cost function).

Gradient descent starts with an initial value such as 0 (zero) or a small random value. Next, the loss (cost) is calculated between model output and truth using a loss function such as mean squared error (MSE) in

$$\text{MSE} = \frac{1}{N} \sum_{n=1}^N (x_n - y_n)^2, \quad (2.17)$$

where  $x$  is model output and  $y$  is truth. MSE is a popular loss function in regression models and is used exclusively in this work for model training. The gradient (first partial derivative) of the loss with respect to each model parameter (weights and biases) is calculated and it indicates the direction and magnitude of greatest *ascent* of the loss function. Since the algorithm is trying to minimize the loss function, the negative gradient (hence gradient *descent*) is employed. One modeling hyperparameter is the *learning rate* which scales the size of the adjustment to the parameters. Figure 2.10 [12] illustrates a very simple example of gradient descent of the loss function with respect to a single parameter, weight  $w$ . The

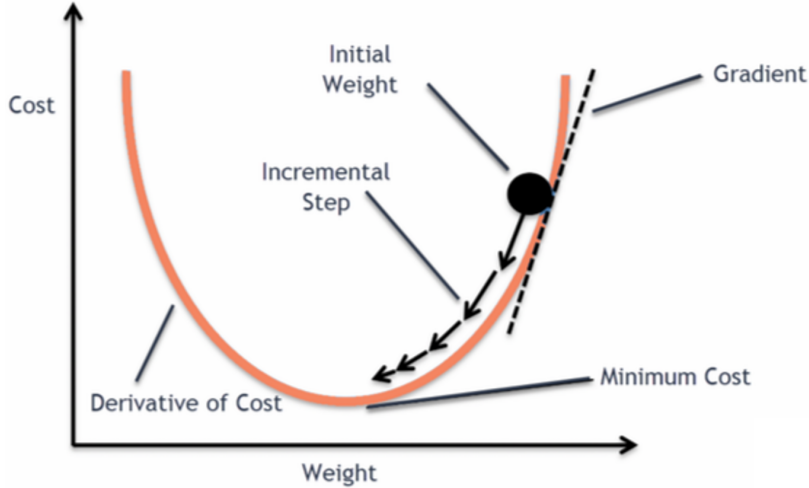


Figure 2.10: Gradient descent of a trivial loss (cost) function

loss is plotted with respect to the weight's value where the orange curve is the derivative of the loss function with respect to the weight. The initial weight is shown at the top right of the derivative curve and the gradient is the dashed tangent line. As stated, the gradient is actually the direction and magnitude of steepest *ascent* but the negative is used for steepest *descent*. Multiple incremental steps of the weight's value is shown, each getting slightly smaller than the previous because the slope of the derivative curve is less steep as the minimum is reached. The learning rate hyperparameter proportionately adjusts the size of the incremental steps in Figure 2.10.

Figure 2.10 illustrates a trivial example of gradient descent. In practice, the loss function with respect to model parameters is very complicated. A nontrivial case of gradient descent is in Figure 2.11 [13]. An arrow illustrates how gradient descent moves through this map by starting at a high loss and iteratively stepping downhill until the global minimum is reached.

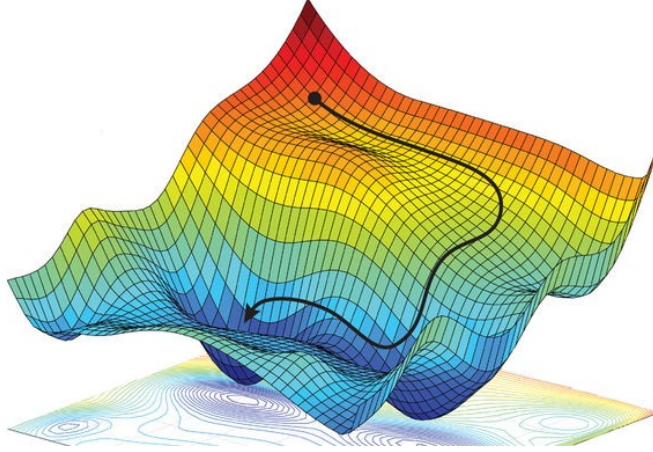


Figure 2.11: Gradient descent of a nontrivial loss (cost) function

The derivative of the loss with respect to a parameter that directly calculates the output is simple to compute. The derivative of the loss with respect to a parameter near the front of the architecture, like in the first fully-connected layer of a 5-layer MLP, is not so simple. The change in a parameter far away from the output causes a change in the parameters that are down the chain toward the output. To handle the train of changes, the chain rule is employed. PyTorch’s automatic differentiation engine *autograd* handles this entire process [6].

There are three common variations of gradient descent. *Batch* gradient descent updates the model parameters based on the loss of the entire training set. So if the model is shown the training set 10 total times, then batch gradient descent provides 10 updates. *Mini-batch* gradient descent updates the parameters every time a sub-sample of N training examples is shown to the model. In this work a mini-batch size of 32 is used exclusively. *Stochastic* gradient descent updates the parameters after every training example. If a training set has 1 million examples and the entire set is only used once, then the model parameters will update 1 million times.

The optimization algorithm used explicitly in this work is *AdamW* [14] which is a variant of the originally proposed *Adam* [15]. The name *Adam* is derived from adaptive moment estimation because it computes individual adaptive learning rates for different parameters from estimates of first and second moments of the gradients. Adaptive gradient methods have become the default method of choice for training feed-forward and recurrent neural networks. The variant AdamW modifies the original Adam to correctly apply weight decay regularization. The modification substantially improves Adam’s generalization on image classification datasets of which it previously performed worse. The improved generalization motivates the use of AdamW in this work.

## 2.6 Chapter Summary

The chapter has laid the foundation of machine learning modeling including the very basics of training and testing, the fundamental MLP and RNN architectures and how they apply to turbulence modeling, popular variants of the RNN cells, and the algorithm for parameter optimization.

## CHAPTER III

### DATASET

Data preprocessing is an essential step in producing an effective machine learning model. The data for training must be representative of the problem being modeled, and the validation and test sets should be representative of the train dataset. Failing to satisfy these conditions can lead to an ineffective model, validation results that lead to poor model and hyperparameter selection, and testing results that inaccurately represent a model's capability. This Chapter steps through the preprocessing applied to the  $C_n^2$  and weather data including filtering, window averaging, formatting into input sequences and forecasts, and parsing into train, validation, and test datasets.

#### 3.1 Measurement Collection Setup

##### 3.1.1 Weather Measurements

The entire dataset uses time correlated weather and  $C_n^2$  measurements. The weather measurements are from a Davis Instruments Vantage Pro2 Plus weather station [16] deployed in front of an office building from 12 April 2020 through 10 August 2020. The weather variables recorded by the station and considered in this work are temperature, pressure, relative humidity, wind speed, and solar irradiance. Table 3.1 lists the technical specs of the weather station including the measurement resolution, accuracy, and archive interval.

The variable resolution refers to the minimum difference measurable, for example relative humidity can distinguish between 90% and 91%, but not between 90% and 90.5%. The resolution of wind speed, 0.45 m/s, is 1 mph (mile per hour) resolution converted to m/s. Variable accuracy is the variable error per measurement, so for example a measurement of

Table 3.1: Davis Instruments Vantage Pro2 Plus Weather Station Measurements

Variable	Resolution	Accuracy $\pm$	Archive Interval
Temperature	0.1°C	0.3°C	1 min
Pressure	0.1 mb	1.0 mb	1 min
Relative Humidity	1%	2%	1 min
Wind Speed	0.45 m/s	5%	1 min
Solar Irradiance	1 W/m <sup>2</sup>	5%	1 min

relative humidity of 90% has an error range of  $\pm 2\%$ . Finally, the archive interval indicates how often the variable is reported. The archive interval is different from the measurement frequency. The anemometer measures wind speed every 2.5 to 3 seconds but the average over the archive interval, 1 minute, is reported. The archive interval of this dataset is 1 minute, the shortest interval available from the weather station.

The location of the weather station is on a storm drain surrounded by grass, about 20 feet to the southwest of a single-story office building. The weather station is not obscured by any trees or shrubbery in very close proximity. To the south of the weather station about 180° field of view is completely open space. The wind measurements are taken by an anemometer about 3 meters above ground level (AGL). The other measurements are recorded about 2.5 meters AGL. Figure 3.1 illustrates the location of the weather station and labels the key sensors and solar panel. The image in Figure 3.1 is taken from the southeast to illustrate the proximity of the station to surrounding geography to the northwest. Beyond the right of the image is the office building about 20 feet away.

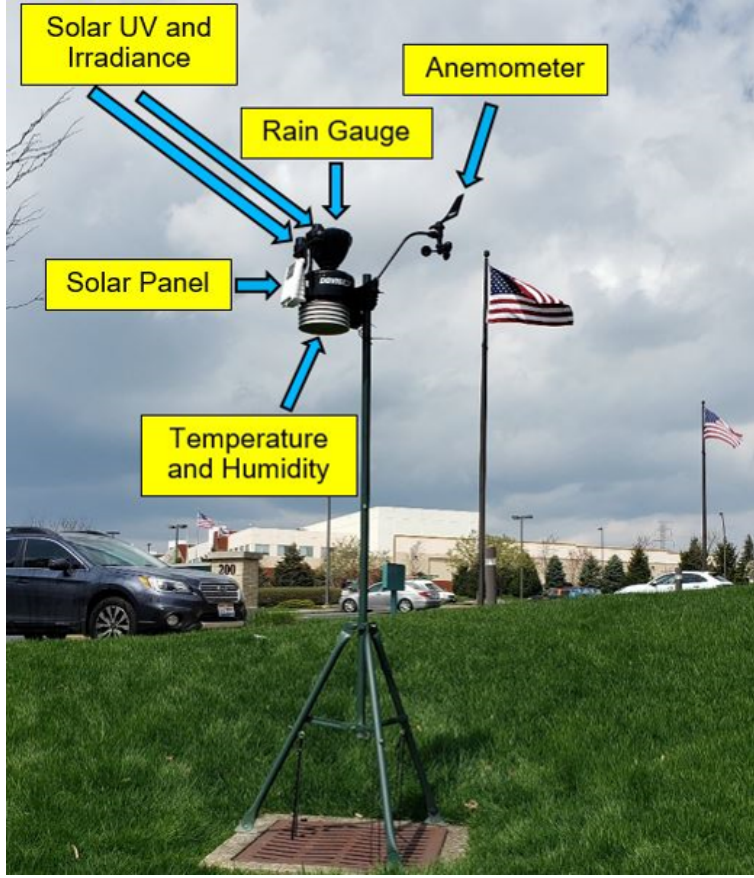


Figure 3.1: Weather station deployment

### 3.1.2 Turbulence ( $C_n^2$ ) Measurements

The other component of the dataset is minute-by-minute measurements of  $C_n^2$  as measured by Delayed Tilt Anisoplanatism (DELTA) turbulence profiler developed by MZA Associates Corporation [17]. The DELTA is a passive imaging sensor that uses a monochrome camera attached to a 6-inch telescope with a 1.5 m focal length. The DELTA collects 300 frames (images) of a target of opportunity at 100 Hz. Using these frames, DELTA calculates differential jitter of feature pairs as a function of angular separation to profile  $C_n^2$ . It is desirable for the target to have high contrast features like edges and corners throughout the

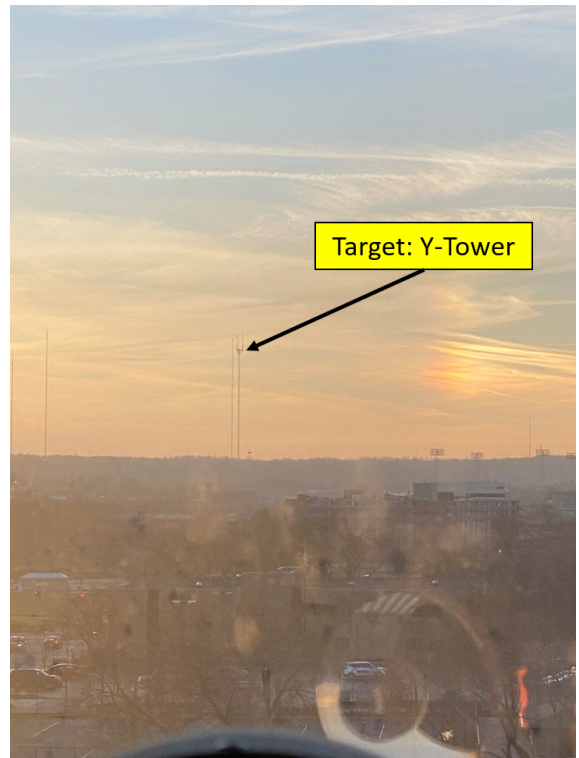
image to make measurements of differential jitter at a variety of separations. Separations of 0.5 to 20 aperture diameters are recommended, so for a 6" telescope aperture the smallest feature separation would be 3" and largest 10' apart in the target plane.

The  $C_n^2$  measurements in this work span from 12 April 2020 through 10 August 2020. During this time the DELTA was deployed on the 5th floor of Fitz Hall at University of Dayton in Dayton, Ohio. Figure 3.2a is a picture of the DELTA's deployment in Fitz Hall. The target the DELTA observes throughout the collection is the *WRGT/WKEF TV Dayton* tower to the southwest of the sensor. The range to the target is 6.4km. The platform is approximately 249 meters above mean sea level (AMSL), and the part of the target being imaged is estimated to be 566 meters AMSL. Figure 3.2b illustrates a wide field-of-view (WFOV) picture of the target being imaged by the DELTA. Figure 3.2c illustrates a narrow field-of-view (NFOV) image of the target during turbulent conditions. Figure 3.2d is a single frame from a DELTA image set during an evening neutral event (low  $C_n^2$  strength). The sharp contrast in foreground and background and the abundance of edges and corners (features) make the target in Figure 3.2d excellent for the DELTA. The tower target is dubbed the "Y-Tower" because from the view of the DELTA the target looks like a "Y" as shown in Figures 3.2c and 3.2d.

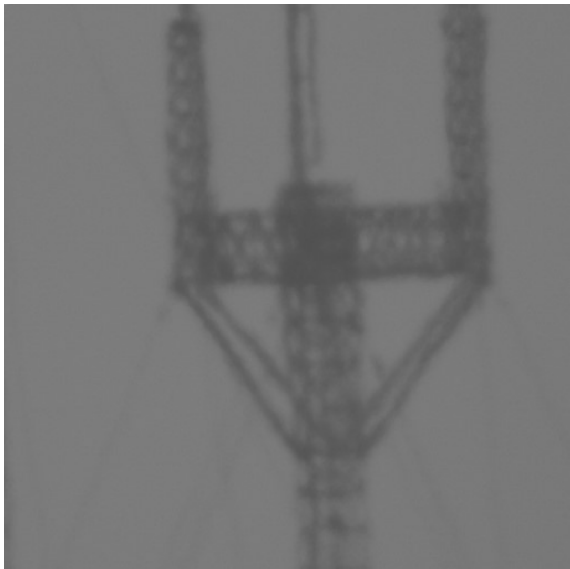
As stated above, the DELTA calculates differential jitter as a function of angular separation to measure  $C_n^2$ . The calculation of  $C_n^2$  at 10 locations along the observation path make the DELTA a turbulence *profiler* in comparison with another sensor, like a scintillometer, which reports only a single  $C_n^2$  for the entire propagation path. The locations, or screens, of these  $C_n^2$  measurements are at 5%, 15%, ..., 85%, 95% along the propagation path. In this work the profiling action is not utilized. Rather, the measurements along the path at each minute are uniform-path averaged to a single  $C_n^2$  measurement per collection that is repre-



(a) Telescope setup



(b) Wide view of target



(c) Narrow view of the target



(d) Target as seen by the DELTA

Figure 3.2: DELTA setup for and target view for collection of minute-by-minute  $C_n^2$  measurements.

sentative of the entire path. Although a uniform-path average is applied, the propagation path's geometry with respect to the terrain is highly relevant to the  $C_n^2$  measurements at each screen and the *type* of propagation path this work investigates.

Figure 3.3a illustrates the geometry of the propagation path. The y-axis is the path altitude AGL, and the x-axis is the path range. Each blue bar represents a DELTA screen at the aforementioned normalized locations along the propagation path. The average screen altitude, 175m, is drawn as a magenta dashed line. Similarly, Figure 3.3b illustrates with

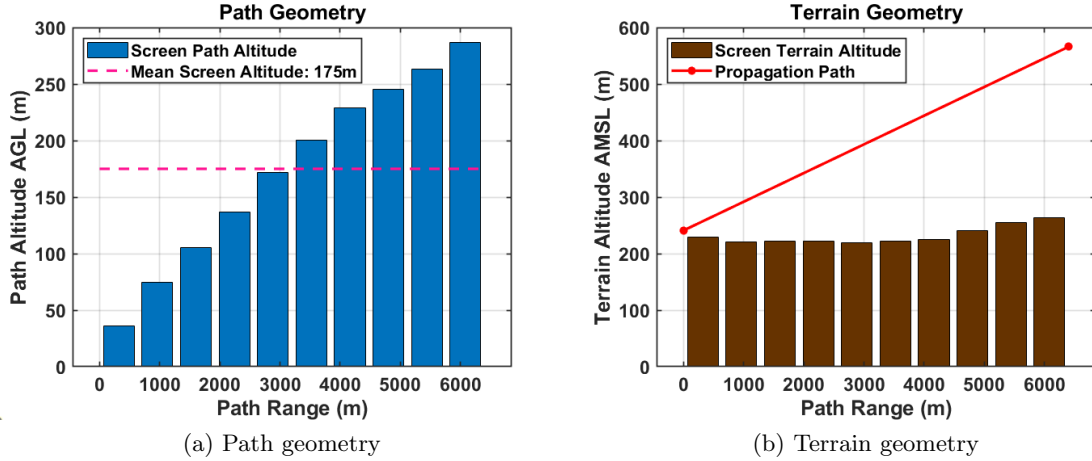


Figure 3.3: DELTA propagation path geometry

brown bars the altitude AMSL of the terrain at the DELTA screens. The propagation path is illustrated as the red line. Note that the angle of the propagation path with respect to the terrain bars in Figure 3.3b is misleading because the x-axis and y-axis limits on the plot are not scaled the same.

The DELTA screens AGL in Figure 3.3a illustrate that the altitude as a function of propagation path linearly increases for nearly the entire path. The average path altitude,

175m, is between the 5th and 6th screen. The height of the brown bars in Figure 3.3b illustrate that the altitude of the terrain as a function of the propagation path does not significantly change over the 6.4 km. This path illustrates that this work builds a machine learning model which forecasts  $C_n^2$  at an average altitude of 175m AGL over 6.4 km. This geometry is unique as many long-term  $C_n^2$  collections do not include these significant altitude changes and average altitude.

### 3.1.3 Spatial Relationship of Platforms and Target

The location of the DELTA ( $C_n^2$ ) platform is approximately 8.87 km to the west of the Vantage Pro2 Plus (weather) platform, and the Y-Tower being imaged by the DELTA is approximately 6.40 km to the southwest of the DELTA platform. The combination of these paths puts the Vantage Pro2 Plus platform approximately 15.05 km from the Y-Tower. Figure 3.4 illustrates the spatial relationship between the three locations of relevance, where each yellow circle marker is approximate location. Above each circle is a label of the location

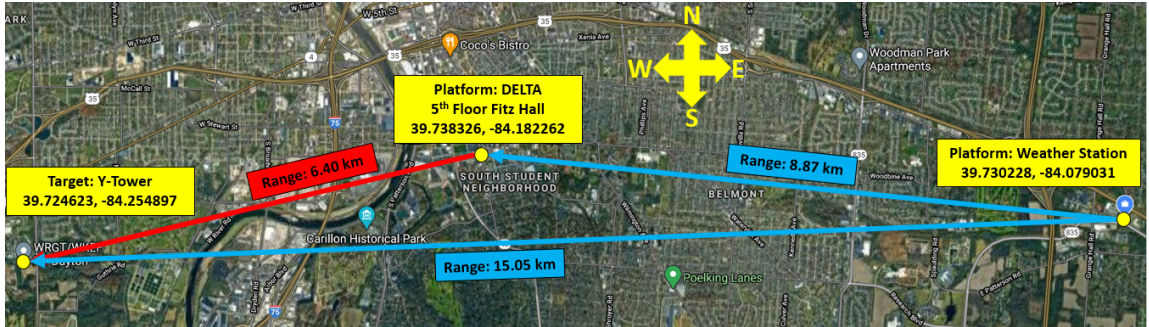


Figure 3.4: Spatial relationship between the DELTA platform, Vantage Pro2 Plus (weather) platform, and the Y-Tower (DELTA) target.

being marked with its latitude and longitude. The red arrow pointing from the DELTA platform marker to the Y-Tower marker represents the DELTA propagation path being

processed to  $C_n^2$ . The blue arrows point from the Vantage Pro2 Plus platform marker to the DELTA platform marker and Y-Tower target marker.

Figure 3.4 illustrates one of the significant challenges of this work. There is significant spatial separation of the  $C_n^2$  path and weather measurements. Turbulence by nature is a highly variable process and adding a gap between 8.87 km and 15.05 km from the weather measurements to the  $C_n^2$  path adds another layer of complexity. The weather measurements at the particular platform location may or may not be correlated with the  $C_n^2$  measurements to the west, and the degree of correlation is vulnerable to change in time. For example, on a cloudless day, the solar irradiance trends are likely highly correlated with the  $C_n^2$  trends, but on a day with scattered clouds the  $C_n^2$  measured at a particular minute might be in the sunshine but the correlated solar irradiance measurement is behind the clouds. This modeling effort is especially subject to the spatial separation since the experiment is performed in Ohio, a state known for high weather variability on day-to-day and even hour-to-hour timescales. Data processing to focus on trends is meant in part to dampen the effect of high frequency events that are not well correlated between the  $C_n^2$  path and weather measurements platform.

A theoretical advantage to modeling with the simple RNN, GRU-RNN, and LSTM-RNN is to combat against the significant spatial separation of the weather measurements and  $C_n^2$  path. Weather tends to flow from west to east, so from Figure 3.4 the  $C_n^2$  measurements will be impacted by weather that is measured at the weather platform at a later time. These architectures process the input sequences as a time-series, thus it is theorized the networks could capture the relationship between measured  $C_n^2$  and temporally offset weather conditions. The following section addresses the data preprocessing techniques applied to the data. One of the techniques is a window-average which is expected dampen some of

the high-frequency temporal differences between conditions at the weather station and  $C_n^2$  path.

### 3.2 Data Preprocessing

#### 3.2.1 Filtering, Window-Averaging, and Interpolating

##### Filtering

The MZA DELTA reports two metrics for each measurement: image confidence and  $C_n^2$  confidence. The confidence levels each range from 0% to 100% and as the names suggest report the quality of the image sequence used for the calculation of  $C_n^2$  and the quality in the  $C_n^2$  calculation. The image confidence is based on four metrics applied to the first frame in a 300-frame collection: image mean, range, entropy, and sharpness. The  $C_n^2$  confidence measure is from the differential jitter variance measurements. It quantifies the similarity between measured variances and the theoretical variances whose  $C_n^2$  profile fits the measured variances. These confidence metrics have been rigorously developed by MZA and their use for data filtering is standard practice.

The  $C_n^2$  measurements can be easily quality-filtered by only keeping measurements which satisfy two user specified thresholds. In this work the thresholds are set to 50% and 70% minimum image and  $C_n^2$  confidence, respectively. Figure 3.5 illustrates the image and  $C_n^2$  confidences of each measurement as a function of local time-of-day throughout the experiment as blue and orange markers, respectively. The black solid and dashed black lines represent the image and  $C_n^2$  thresholds. A  $C_n^2$  measurement is removed if an orange marker is below the dashed black line *or* if a blue marker is below the solid black line. The majority of the  $C_n^2$  confidences throughout the day are above the specified threshold. Most of the measurements removed due to  $C_n^2$  confidences are in the early morning and late evening

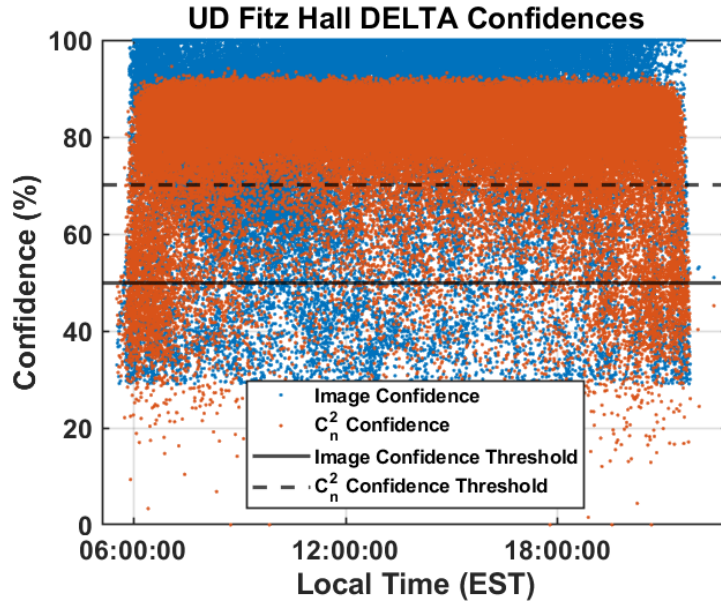


Figure 3.5: DELTA image and  $C_n^2$  confidences.

when target illumination is less than ideal resulting in poor differential jitter measurements. The image threshold filtering is more uniform across the entire day. A high  $C_n^2$  confidence is more important to a measurement than a high image confidence, so the threshold for the image confidence is lower. Of the 76,186 measurements that passed the confidence thresholds, the average image and  $C_n^2$  confidences are over 91% and 83%, respectively.

The Vantage Pro2 Plus weather station does not report data quality metrics on a per-variable basis. Evaluation of weather measurements in plots does not raise questions of data quality, both in the raw measurement value for a check of nonphysical values, and measurement trends for a check that the temporal rate of change of the measurements is realistic.

## Window-Averaging

After quality filtering, the weather and  $C_n^2$  measurements are window-averaged. Given four inputs, a written function returns an array of window-averaged datetimes (dates + times) and corresponding window-averaged measurements. The four inputs are an input array of datetimes, an input array of measurements, a window width, and an interval size. The window width determines the temporal width the function uses to calculate an average. For example, given a window width of five minutes the window will look at  $\pm 2.5$  minutes around the current time being averaged. Any measurements  $\geq$  to the current time minus 2.5 minutes and  $<$  the current time plus 2.5 minutes is included in the average. The datetime returned for this example window averaged measurement is exactly the middle of the window. The interval size determines the temporal step each iteration. For example, given an interval size of one minute, the function will perform a window average about minute 07:05 on a given day, then step to perform a window average about minute 07:06. This iteration stops when the window includes a datetime beyond the last datetime in the array of measurements.

This modeling effort focuses on learning the relationship between the trends of prior environmental measurements and future  $C_n^2$  measurements. To achieve this the window average uses a width of 30 minutes ( $\pm 15$  minutes) and interval of 1 minute. This wide window significantly smooths the weather and  $C_n^2$  measurements to dampen high-frequency events and amplify the trends. This more significantly impacts the  $C_n^2$  measurements which are highly stochastic by nature.

## Interpolating

After window averaging both sets of measurements, each is linearly interpolated to datetimes from 12 April 2020 through 10 August 2020 sampled every 30 minutes. The linear interpolation is performed by an open-source robust implementation from *NumPy* [18]. For each set of interpolations (weather and  $C_n^2$ ), only interpolations less than 30 minutes are kept. Those that do not pass this condition are simply set to Not a Number (NaN) to preserve the arrays of measurements and datetimes sampled every 30 minutes. After this step the data is reduced to 5809 measurements at a 30 minute sample rate.

### 3.2.2 Formatting into Sequences and Forecasts

#### Nighttime $C_n^2$ as Input Sequences

A limitation of the experimental setup described in Section 3.1.2 is the passive imager DELTA lacking an illuminated target. As a result,  $C_n^2$  measurements before 06:00 and after 22:00 are entirely absent. Without a method to fill the nighttime  $C_n^2$  this modeling technique is unable to incorporate prior  $C_n^2$  measurements as an input variable to the model. It is hypothesized that including prior  $C_n^2$  as an input will improve modeling performance as it will provide the model information about the trend of  $C_n^2$  leading up to the forecast. The model is expected to learn that its first forecast time step should follow the leading trend. If results indicate the inclusion of prior  $C_n^2$  improves forecasting, then a technique for filling missing nighttime data is necessary for real-world applications where a target may not be illuminated during nighttime but morning forecasts are still required. The weather measurements are taken day and night, so no fill technique is required.

The data after filtering, window-averaging, and interpolating as described in Section 3.2.1 is the basis of the nighttime  $C_n^2$  filling. Nighttime measurements are classified as an index where the measurement is before 08:00 or after 20:00, and whose  $C_n^2$  measurement is already labeled as NaN. This technique generously includes times from late evening and early morning, but only those which are already missing measurements. Of the 5809 data points, 2065 (35.5%) satisfy these conditions. Without this filling, over a third of the dataset would be removed from consideration for further processing. Of the 2065 filled measurements, 124 fall into early morning and late evening at 07:00 and 21:00, illustrating the need to be generous with the classification of “nighttime.” The effect of missing data is further amplified when complete sequences of data must be formatted in next steps.

The average of the  $C_n^2$  dataset is approximately  $9 \times 10^{-16} (m^{-2/3})$  so rounding sets the  $C_n^2$  fill-value for the qualifying indices to a constant  $1 \times 10^{-15} (m^{-2/3})$ . Every input sequence used for training will have a constant  $C_n^2$  and solar irradiance measurement of  $0 W/m^2$  during nighttime, thus it is expected the model will learn the difference between a constant sequence  $C_n^2$  and a sequence of varying  $C_n^2$  leading up to the forecast.

### Formatting into Sequences and Forecasts

The next step in the data processing is to format into input sequences (time series) and output forecasts. As part of the grid search described in Section 4.1, multiple input sequence lengths are formatted to investigate the amount of prior weather and  $C_n^2$  measurements to most effectively forecast future  $C_n^2$  conditions. The forecast length of 4 hours (eight 30-minute time steps) is held constant for every input sequence length. Sets of sequences and forecasts are formatted for input sequence lengths of 4 hours (8 time steps), 8 hours (16 time

steps), 12 hours (24 time steps) and 16 hours (32 time steps). The logic of the formatting follows.

Loop through the entire formatted dataset one time step at a time. The sequence is every input variable (temperature, pressure, relative humidity, wind speed, solar irradiance, and nighttime-filled  $C_n^2$ ) up to the desired sequence length. For example with a 4 hour sequence length, the sequence is the first 8 time steps. Then, the forecast is the measured  $C_n^2$  for the next 4 hours (8 time steps) immediately following the last time step in the input sequence. If any part of the input sequence or output forecast contains a NaN then the sequence/forecast pair is not kept. As a result of this filtering, a single NaN can cause many sequence/forecast sets to be removed because they're filtered regardless of how many NaNs are in the sequence/forecast and their location within the series. This process loops through the entire dataset until the last time step of the forecast is beyond the last time step of the dataset. This process is repeated for each of the desired sequence lengths: 4 hours, 8 hours, 12 hours, and 16 hours. Once each is formatted, only the sequence/forecasts pairs common to all sequence lengths are kept to maintain consistency in training, validating, and testing. A total of 1255 sequence/forecast pairs are common amongst each of the sequence lengths.

### 3.2.3 Final Data Preparations for Modeling

#### Parse Data into Train, Validation, and Test Sets

Proper parameter search to find the best model requires an unbiased evaluation of the models trained during the search. Once a model and parameters are selected, the model must be evaluated again without bias to form conclusions about the model's capability. To achieve this, the formatted dataset must be broken into three parts: train, validation, and test datasets. The ensemble of models for the parameter search are trained exclusively

with the train dataset. The evaluation of the models from the parameter search is based on validation dataset performance. The best model as evaluated on the validation dataset is trained on the train and validation datasets concatenated together, then applied to the test dataset for a final evaluation.

Modeling future  $C_n^2$  conditions from prior environmental measurements is dependent on the time of day and year due to daily and seasonal weather fluctuations. This feature is amplified to a significant challenge in the context of a real-world application of this problem: forecasting  $C_n^2$  conditions days or weeks beyond the last day of training examples. In this scenario the model is tasked with extrapolating forecasts given input weather conditions that are not representative of the train dataset. The input conditions could be unique in their temporal evolution or the measurements are beyond the dynamic range of the training data. An example of significant model extrapolation that could lead to poor performance is training a model on data from summertime then performing inference on data from wintertime.

As stated above, both the weather and  $C_n^2$  measurements for this work range from 12 April 2020 through 10 August 2020, springtime through summertime. Following the timeline of model training and deployment, the train, validation, and test datasets are parsed from the entire dataset in the order listed. The ensemble of models for the parameter search is trained on the train dataset which temporally spans from the beginning of the data to a selected endpoint. The models are evaluated on the validation dataset which temporally spans from immediately after the train dataset endpoint to another selected endpoint. The train and validation datasets are concatenated and applied to a test dataset which starts immediately after the validation dataset endpoint.

The train, validation, and test datasets are selected on two criteria in this work. The first is the real-world scenario of deploying sensors for 1-2 months before an experiment where forecast  $C_n^2$  conditions are relevant. Experiments of this nature are often scheduled many months in advance at minimum so sensor deployment 1-2 months before is realistic. This deployment time increases the range of unique weather and  $C_n^2$  conditions for model training examples before inference on experiment days. The second criteria is bounding the dataset to summertime to avoid model extrapolation. This scenario idealizes the model development and evaluation since evolution of weather conditions is an inherent problem, but analysis of significant model extrapolation is not within the scope of this work. Obeying this criteria, the full dataset for training through testing spans 01 June 2020 through 10 August 2020. Figure 3.6 illustrates the input sequence variables as a function of local time for the selected dataset. Temperature, pressure, relative humidity, wind speed, solar irradiance, and nighttime-filled  $C_n^2$  are in Figures 3.6a - 3.6f, respectively. The plotted measurements are after the data processing described above, so they're at 30-minute intervals after filtering, window-averaging and interpolating. Furthermore in each plot, the train, validation, and test datasets are plotted with black, blue, and red markers, respectively. The train dataset spans from 01 June through 17 July. The validation dataset spans from 18 July through 01 August. Finally, the test dataset spans from 02 - 10 August. The test dataset spans nine days, but measurements on 02 August and 04 August are absent. Of the 1255 sequence/forecast pairs, 933 (74.3%) are in the train dataset, 174 (13.9%) in the validation dataset, and 148 (11.8%) in the test dataset.

The measurements in Figure 3.6 illustrate many interesting features. First for temperature in Figure 3.6a, the benefit of only using data from June through August is shown. Across the entire dataset, except for the very first day, the temperature measurements are

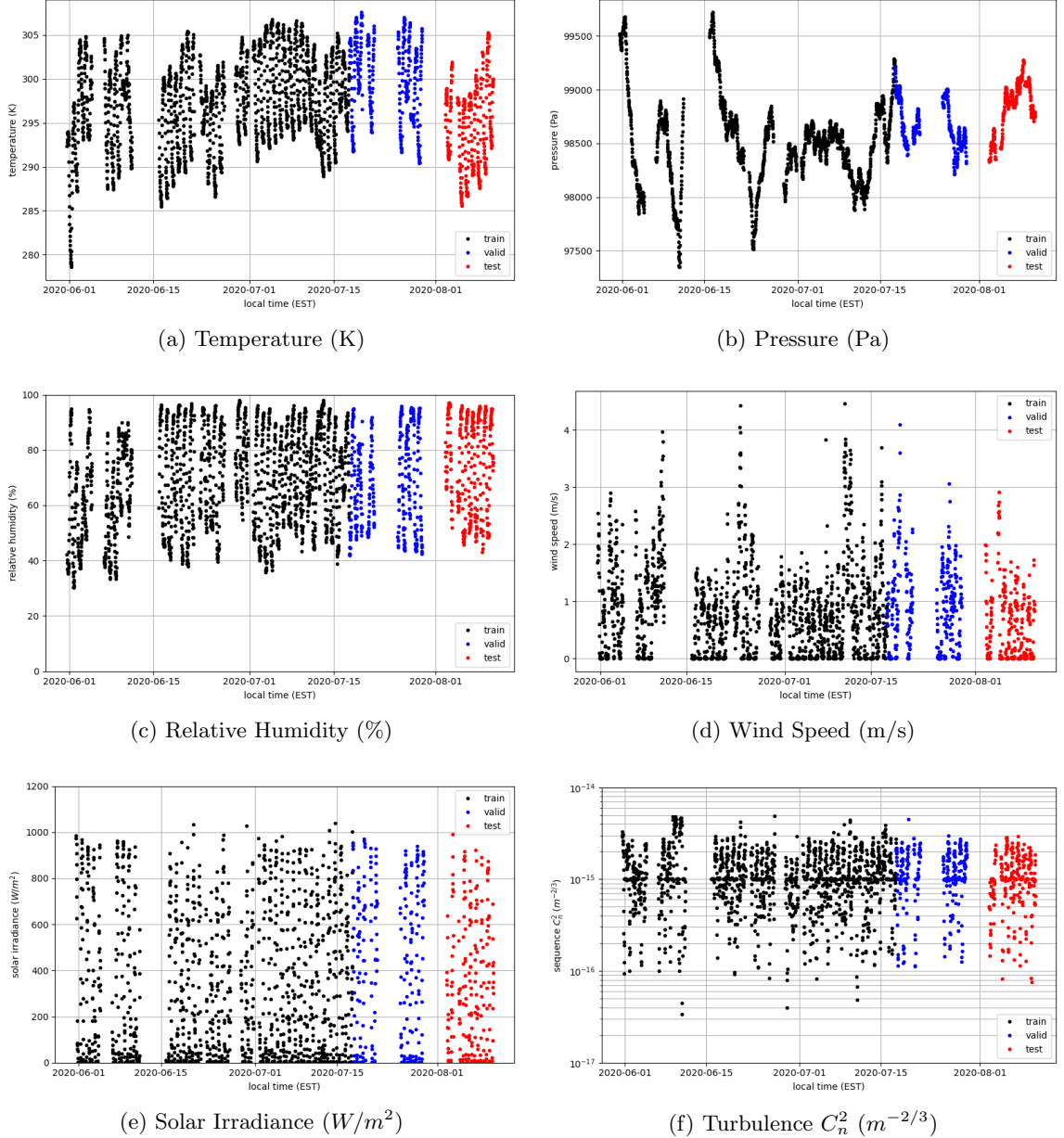


Figure 3.6: Sequence data as a function of time, parsed by train, validation, and test datasets drawn in black, blue, and red, respectively.

within about 20 Kelvin. Further, the validation dataset (blue) is a great representation of the train dataset (black). The test dataset (red) has a few cold days in the beginning, but then warms up again. This cold snap is not ideal, but is well within the dynamic range of the train and validation datasets. Pressure in Figure 3.6b shows that long, large scale measurements are made in June but in July and August the measurements are on a shorter scale. The validation and test pressure datasets are well within the dynamic range of the train dataset, but do not illustrate clearly similar trends.

Relative humidity in Figure 3.6c is a very stable weather measurement across the train, validation, and test datasets. The measurements never drop below 30%, and the validation and test datasets are within the dynamic range of the train dataset. The oscillatory nature of relative humidity is shown in Figure 3.6c and appears consistent between the three datasets. Wind speed in Figure 3.6d is not a stable measurement. An oscillatory nature is not apparent, and wind speed is a significant driver of weather events as shown by the spikes in measurements, especially in the train dataset. Commonality between the three datasets in Figure 3.6d are not clearly extracted.

Solar irradiance in Figure 3.6e is another stable weather measurement across the three datasets. The model is expected to learn the temporal aspect of solar irradiance, i.e., a measurement of 0 (zero) indicates nighttime, and also the variation from a standard diurnal trend is due to cloud conditions which is typically associated with  $C_n^2$  conditions which also deviate from a standard diurnal trend. Solar irradiance is directly impacted by the seasonal weather change (Earth's axial tilt). The highest solar irradiance measurements for a day is in summertime, specifically around the summer solstice. The highest measurement of the day gradually decreases from the summer solstice to a minimum around the winter solstice. This effect is not obviously apparent in Figure 3.6e since only summertime is considered.

Sequence  $C_n^2$  in Figure 3.6f illustrates stability and the impact of nighttime filling with  $1 \times 10^{-15}(m^{-2/3})$ . First, the test and validation datasets are strongly representative of the train dataset. Besides a few instances in the whole dataset, the maximum  $C_n^2$  does not increase above  $3 \times 10^{-15}(m^{-2/3})$ . Daily oscillation of  $C_n^2$  is apparent in Figure 3.6f and is the standard diurnal trend. The low-strength  $C_n^2$  conditions are much more variable than high-strength conditions. There are several examples of  $C_n^2$  weaker than  $1 \times 10^{-16}(m^{-2/3})$  but they are spread through the entire dataset. These events are associated with particularly strong evening neutral events that occur when atmospheric gradients, like temperature with respect to altitude, trend to zero. The line of markers at  $1 \times 10^{-15}(m^{-2/3})$  in Figure 3.6f is the nighttime padding. These padded measurements are strongly correlated with the  $0W/m^2$  solar irradiance measurements in Figure 3.6e.

The relationship of the train, validation, and test datasets is further shown in Figure 3.7 which plots probability densities of each input sequence variable. Temperature, pressure, relative humidity, wind speed, solar irradiance, and nighttime-filled  $C_n^2$  are plotted in Figures 3.7a through 3.7f, respectively. Similarly to the temporal plots, the black bars in Figure 3.7 represent the train dataset, blue bars the validation dataset, and red bars the test dataset. The bars in each plot of Figure 3.7 represent how the *distribution* of the three datasets relate to each other. They also explicitly show how the dynamic range of the validation and test datasets relate to the dynamic range of the train dataset.

Temperature in Figure 3.7a shows that the distribution of the validation dataset is near the high-temperature portion of the train dataset since the blue bars are to the right of the plot. There are even blue bars at the very high temperatures where there are no black bars which is indicative that there are measurements in the validation dataset which are hotter than anything in the train dataset. This is an example where the model is forced to extrapolate.

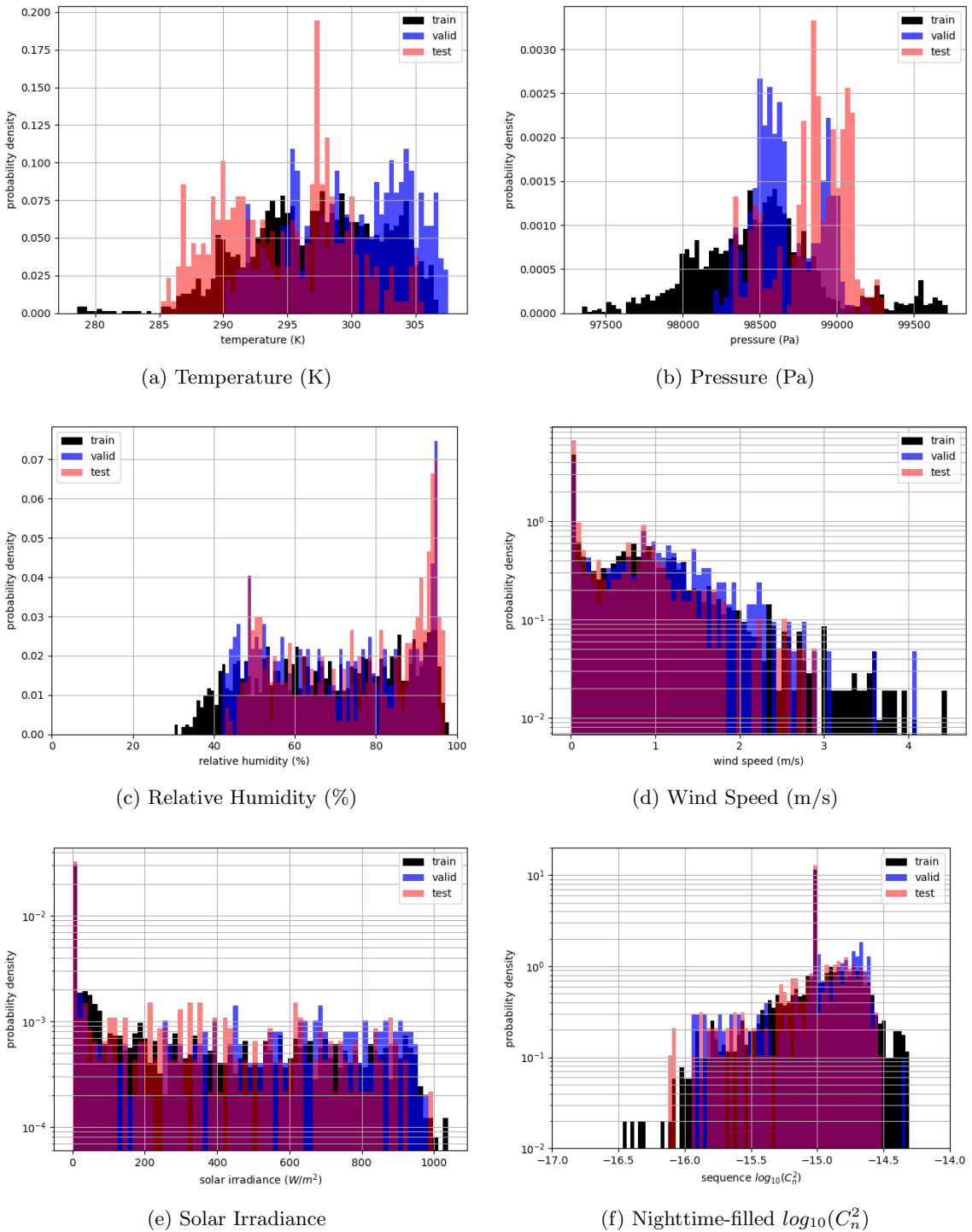


Figure 3.7: Sequence data in normalized histograms, parsed by the train, validation, and test datasets drawn in black, blue, and red, respectively.

olate given input measurements its never encountered in training. The test dataset (red bars) is at the lower end (left side) of the temperature distributions indicative that colder temperatures are part of the test measurements. These low temperature measurements are still within the bounds of the train dataset dynamic range since there are black bars to the far left of Figure 3.7a. The features of these distributions are consistent with the features noted in the temporal plot in Figure 3.6a.

Pressure in Figure 3.7b shows that the pressure distribution is most populated around 98,500 Pa and looks similar to a Gaussian distribution. The validation dataset is mostly distributed around the center of the train distribution, an encouraging feature. The test dataset is similarly distributed but a scale factor higher around 99,000 Pa. There is also a significant amount of validation dataset pressure measurements around this value.

Relative humidity in Figure 3.7c illustrates the stability between the three datasets as first described above. The distribution of the three bar sets are very similar in shape and magnitude. The spike in probability just below 100% and the slight rise around 50% is characteristic of all three datasets. The distribution between these percentages is likewise very similar. Figure 3.7c illustrates an ideal case for the datasets to be highly representative of each other.

Wind speed in Figure 3.7d is the first histogram to show comparison that is more encouraging than the temporal plots in Figure 3.6. The shape of the three distributions in Figure 3.7d are very similar from wind speeds of 0 m/s to about 2 m/s. The spike in measurements at 0 m/s is highly consistent among the three distributions. The sharp drop off, back to another increase around 1 m/s, and then the gradual decline in probability from 1 m/s to 2 m/s, is also consistent amongst the distributions. The validation distribution

continues to follow the train distribution beyond 2 m/s, but the test measurements become far more sparse. Figure 3.7d indicates that below 2 m/s the validation and test distributions are highly representative of each other. However, the temporal trends of wind speed are most relevant to this problem and that is not illustrated in the histogram. As stated earlier, the temporal trends in wind speed are not clear in Figure 3.6d.

The solar irradiance distributions in Figure 3.7e are highly representative of each other. The spike in probability density at  $0W/m^2$  is nearly identical across the three distributions. Furthermore, the shape of the distributions up to  $1000W/m^2$  are also very similar. Some gaps exist in the test dataset, but the general distribution is representative. Most importantly, the validation and test distributions are within the dynamic range of the train distribution.

Finally, nighttime-filled  $\log_{10}(C_n^2)$  in Figure 3.7f again illustrates very similar distributions between the three datasets. For the majority of the measurements from about -15.75 through -14.5 the distributions are nearly identical. The spike in probability at -15 is due to the nighttime-filling. The dynamic range of the validation and test datasets are mostly well within the bounds of the train dataset. Generally, the relationship of the distributions in Figure 3.7f is an ideal scenario.

The other part of the sequence/forecast pair is the forecasts. Figure 3.8 illustrates the temporal and histogram plots in Figures 3.8a and 3.8b. These plots are nearly identical to input sequence  $C_n^2$  Figures 3.6f and 3.7f with the primary difference being the lack of nighttime measurement filling at  $1 \times 10^{-15}(m^{-2/3})$ . This is shown as the missing line of markers in Figure 3.8a and the missing spike in Figure 3.8b. The three datasets are very similar both temporally and in their distributions, again a highly desirable quality. An

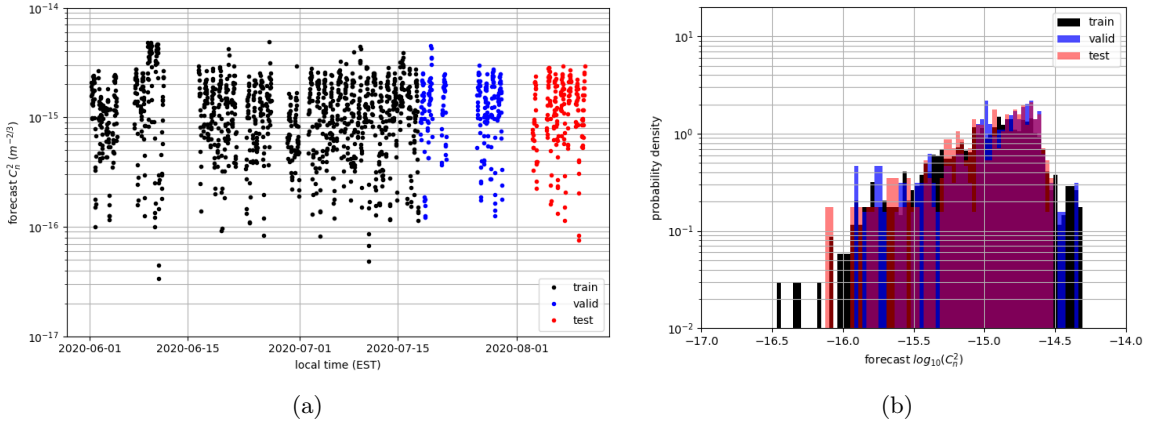


Figure 3.8: Turbulence ( $C_n^2$ ) forecasts as a function of time and as a normalized histogram. The train, validation, and test datasets are drawn in black, blue, and red, respectively.

interesting feature about the three datasets in Figure 3.8a is that the validation dataset has a measurement above  $3 \times 10^{-15}(m^{-2/3})$  but the test dataset does not. Furthermore, the validation dataset does not have any measurements weaker than  $1 \times 10^{-16}(m^{-2/3})$  but the test dataset has two. The histogram in Figure 3.8b reflects this. These features are the most significant difference between the three datasets and potentially could impact the parameter selection process and final model evaluation. The parameter selection process is evaluated on a dataset which does not have any extremely deep  $C_n^2$  events. Therefore the best model could be a model which does not learn to handle these deep neutral events at all which will result in poor performance on the deep neutral event in the test dataset. Furthermore, the validation dataset has an event of abnormally strong  $C_n^2$ . This could also lead the best model to handle these events well but will not be reflected in the final model evaluation since an event of this sort is not in the test dataset.

Overall, the sequences and forecasts presented in Figures 3.6, 3.7, and 3.8 show that the train, validation, and test datasets are strong representations of each other, and there are

no significant changes in weather patterns on a day-to-day and seasonal basis. Also, a few measurements of temperature is the only instance of a validation or test measurement being beyond the dynamic range of the train dataset. This small outlier does not propagate to the test dataset because the final model is trained on the combination of train and validation datasets. These are highly desirable characteristics for a machine learning study.

### Data Normalization

With the sequence/forecast pairs for training, validation, and testing, the final step in data processing is to normalize the data for training and inference. The normalization parameters are derived from the train dataset, but are applied to the train, validation, and test datasets. In this work each input variable and output  $C_n^2$  from the train dataset are min-max ranged between 0 (zero) and 1 using

$$\hat{x} = \frac{x - x_{min}}{x_{max} - x_{min}}, \quad (3.1)$$

where  $x$  is the variable considered,  $x_{min}$  is the minimum of  $x$ ,  $x_{max}$  is the maximum of  $x$ , and  $\hat{x}$  is the normalized variable. To ensure stability, data normalization for  $C_n^2$  is applied to the  $\log_{10}(C_n^2)$  since values associated with turbulence are most often smaller than  $1 \times 10^{-12}(m^{-2/3})$ . The normalization parameters  $x_{max}$  and  $x_{min}$  are saved then Equation 3.1 is applied to the validation and test datasets. Any measurements outside of  $x_{max}$  or  $x_{min}$  will normalize to beyond 0 (zero) and 1.

Throughout this work evaluation of model performance is done in  $\log_{10}(C_n^2)$  space so model outputs must be unnormalized by

$$x = \hat{x} \cdot (x_{max} - x_{min}) + x_{min} \quad (3.2)$$

and compared with the unnormalized measurement  $C_n^2$  forecasts.

### 3.3 Chapter Summary

This Chapter has set the foundation of the dataset used in this effort. The weather and  $C_n^2$  sensors have been described and their spatial relationship has been discussed as a significant challenge of this work. The geometry of the DELTA  $C_n^2$  sensor has been analyzed and shown to be unique. The dataset used in the modeling including the data processing techniques has been described and is shown to be nearly ideal for machine learning modeling.

## CHAPTER IV

### GRID SEARCH

This Chapter first walks through the methodology used to select the best model and parameters to forecast four hours of  $C_n^2$  given prior environmental measurements. Next, it motivates the statistical test performed to support model selection for testing. Finally, this Chapter selects a model for final evaluation and summarizes the reasons for selection.

Model performance is evaluated with the root-MSE (RMSE) between model output and truth. The RMSE is given by

$$\text{RMSE} = \sqrt{\frac{1}{N} \sum_{n=1}^N (x_n - y_n)^2}, \quad (4.1)$$

where  $x_n$  is model output,  $y_n$  is truth (measurement), and  $N$  is the total number of output/truth pairs.

#### 4.1 Methodology

Given a problem to model with machine learning there are model hyperparameters to adjust in infinitely many combinations, each of which can impact model performance. Just a few examples of these hyperparameters are the optimization algorithm, the learning rate of the optimization algorithm, the number of layers in the model architecture and the number of nodes per layer. Given the many combinations of a model’s hyperparameters, a careful method to determine the best combination must be employed. The definition of the “best” model is the model which results in the best performance when applied to the validation dataset, a subset of the entire dataset specifically held from training for hyperparameter tuning. By holding back the validation dataset, an unbiased optimization of the hyperparameters can be performed. The model and training parameters which performs best on

the validation dataset is then applied to the test dataset for a final unbiased evaluation of the selected model.

There are many methods of hyperparameter optimization, but common methods are grid search and random search. Grid search, or a parameter sweep, is an exhaustive search through manually specified hyperparameters. If iterating over only one hyperparameter, for example three different learning rates, three models are trained with the three learning rates. A model is trained with the first learning rate and its performance on the validation dataset is recorded, then another model is trained but with the second learning rate and the performance on the validation dataset is recorded. This is done once more for the third learning rate. The performance of the models with the three learning rates are compared and the best learning rate is the learning rate used by the model that performed best. This method can quickly explode in computation time as the number of hyperparameters to iterate increases. For example, iterating over two hyperparameters of three values each results in nine combinations of hyperparameters. The number of combinations is defined as the multiple of the number of values across each hyperparameter, so if there are five hyperparameters with 1, 2, 3, 4, and 5 values, then the total number of combinations is  $1 \times 2 \times 3 \times 4 \times 5 = 120$  combinations.

The other common method, the random search, replaces the exhaustive grid search by randomly selecting hyperparameters within defined bounds. An algorithm randomly selects the hyperparameters and models are trained with the different combinations then applied to the validation dataset to evaluate performance. A benefit of the random search is the selection of parameter combinations that might not be defined in a grid search.

In this work the grid search is employed because prior knowledge of hyperparameters is unknown, thus the exhaustive grid search is necessary to explore a wide range of combinations. This grid search iterates over five parameters. The outermost parameter is the four fundamental architectures developed in Chapter II: MLP, simple RNN, GRU-RNN, and LSTM-RNN. The MLP is a common machine learning architecture and serves as the baseline. The simple RNN, GRU-RNN, and LSTM-RNN are variants of the general RNN and are searched to find if a specific variant is better or worse than the others when applied to this problem. As developed in Chapter II, these variants of RNNs each process the inputs as a time series, but differ in *how* they process. The next parameter is the input sequence variables used by the model. From Section 3.2.3, the available input sequence features (variables) are prior temperature, pressure, relative humidity, wind speed, solar irradiance, and  $C_n^2$  measurements. The *input features* parameter iterates over which features (variables) to train the model. Since there are six available features, and each feature can only be used or not used, there are  $2^6 = 64$  total combinations. However, a threshold is set to train on a minimum of four features which reduces the total number of input feature combinations to 22. This threshold is set to discourage the model from memorizing one or two features, and for a significant reduction in computation time.

The third search parameter is the *input sequence length*. Independent of the input features (variables), in a single sequence/forecast the amount of information available to the model is dependent on the time-length of the input sequence. Whether the model performs best with only 4 hours of input data or 16 hours of input data is a highly desired result. Thus, four lengths of the input sequence are searched: 4, 8, 12, and 16 hours. These lengths are chosen to be  $1\times$ ,  $2\times$ ,  $3\times$ , and  $4\times$  the 4 hour forecast length. Note that the train, validation, and test datasets are carefully formatted so the same forecasts are trained,

validated, and tested regardless of the input sequence length. This avoids an instance where a 4 hour input sequence might exist for a particular forecast but a 16 hour input sequence is not available due to missing data. This processing step is described in Section 3.2.2. The fourth parameter searched is the number of hidden layers in each architecture: 1 or 2. The fifth and final searched parameter is the number of hidden nodes per hidden layer: 10 through 50 in steps of 10. The final two parameters essentially search over the number of parameters in the model with some variation in the interaction of those parameters. Each fundamental architecture in total iterates over  $22 \times 4 \times 2 \times 5 = 880$  combinations of parameters. Due to the stochastic nature of model training, a single model could perform significantly different than another model trained with the same parameters, thus a total of 10 models are trained per combination per fundamental architecture to ensure the stability of results. In this search a total of  $880 \times 4 \times 10 = 35,200$  models are trained.

For each model trained in the grid search the following parameters are fixed: mini-batch size, optimization algorithm, initial learning rate, learning rate decay (step and decay factor), and weight decay. The mini-batch size, the number of training examples used per model parameter update, is set to 32 yielding a total of 30 parameter updates (933/32) per epoch (iteration through the entire dataset). The optimization algorithm is AdamW[15] [14]. The initial learning rate is 0.01 and decays by a factor of 10 every 10 epochs. This results in learning rates 0.01, 0.001, 1e-4, 1e-5, and 1e-6 from epochs 1 - 10, 11 - 20, 21 - 30, 31 - 40, and 41 - 50, respectively. The high initial learning rate is to ensure suitably-high gradients are back-propagated through the model to allow each model 10 epochs (300 total parameter updates) to escape any local minima. This training method consistently leads to a strong model convergence in only a few seconds. The weight decay is a regularization

technique applied to the optimization algorithm [14] and is 0.001. This value performed well in early results and motivation to change it never presented itself.

## 4.2 Grid Search Results

The analyses of the grid search are performed independently on each architecture. From the four grid searches, four 2d-arrays of RMSE loss scores, the performance metric between validation truth and output  $\log_{10}(C_n^2)$ , are recorded for analysis. The 2d-arrays are shape  $880 \times 10$  for 880 parameter combinations and 10 models each. From these four 2d arrays, the average and standard deviation of the RMSE scores are calculated per parameter combination yielding four arrays of 880 averages and standard deviations. The standard deviation, the square root of the average of the squared deviations from the mean, is calculated by

$$\sigma = \sqrt{\frac{\sum (x - \bar{x})^2}{N - ddof}} \quad (4.2)$$

where  $\sigma$  is the standard deviation,  $x$  is the data,  $\bar{x}$  is the average of the data,  $N$  is the number of data points, and  $ddof$  is the delta degrees of freedom. Using  $ddof = 1$  provides an unbiased estimator of the variance of the infinite population. It is standard practice to use  $ddof = 1$ .  $ddof = 0$  should be used in the situation of measuring the variance of a distribution whose mean  $\bar{x}$  is known a priori rather than being estimated from the data [19].

If the average,  $\bar{x}$  in Equation 4.2, were calculated many times with different sets of sampled data the values of  $\bar{x}$  would themselves have a standard deviation. This is called the *standard error* of the estimated mean  $\bar{x}$ . Assuming the underlying distribution is Gaussian, the *standard error* is given approximately by

$$\sigma_{\bar{x}} = \frac{\sigma}{\sqrt{N}}, \quad (4.3)$$

where  $\sigma_{\bar{x}}$  is the standard error of the mean,  $\sigma$  is the standard deviation from Equation 4.2, and  $N$  is the number of samples used to calculate  $\bar{x}$  [19]. In the calculation of the standard error of the average loss scores,  $N$  is 10 for the number of models trained for each iteration of the grid search. From these statistics the best model as applied to the validation dataset is determined and significance quantified.

#### 4.2.1 Results Sorting

The four arrays of average RMSE scores are sorted from best to worst and the sort indices are applied to the array of grid search parameters. From these sorted arrays the best model and its parameters are extracted. Figure 4.1 illustrates the validation average  $\log_{10}(C_n^2)$  RMSE loss as a function of the sorted index. Figure 4.1a plots all 880 sorted scores for each fundamental architecture. Figure 4.1b plots only the first ten to focus on the best performers. In each plot MLP is drawn in blue, simple RNN in orange, GRU-RNN in green, and LSTM-RNN in red. The curves in each figure are monotonically increasing because the sorted losses are plotted. Figure 4.1b additionally plots the standard error. The

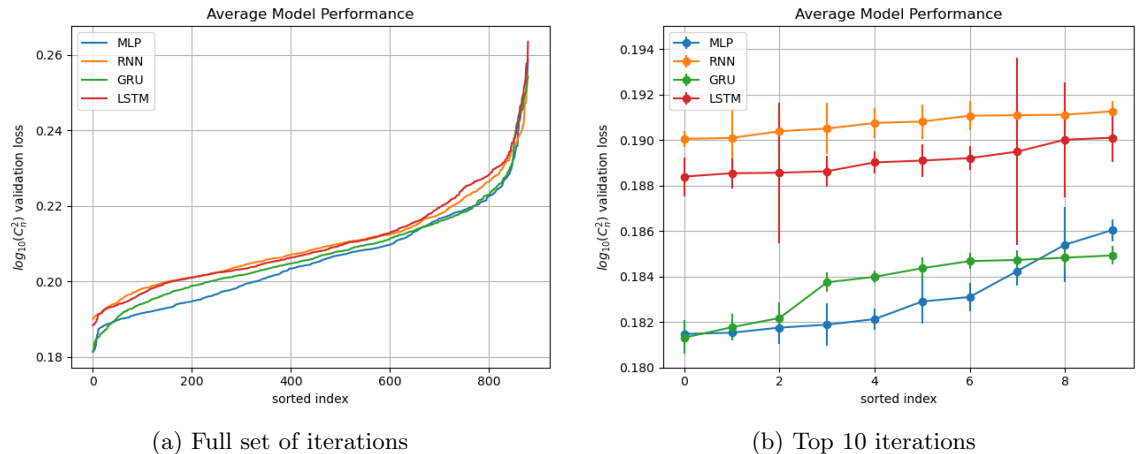


Figure 4.1: Grid search results.

general shape of the sorted loss curves are highly correlated from architecture to architecture and their slopes are consistent from sorted index 100 through 800. On either side, between sorted indices 0 through 100, and 800 through 880, the curves exponentially increase. This is an indication that there are a general set of modeling parameters which are notably better than all the others, and likewise a set that are far worse than the others.

In terms of model performance, the curves in Figure 4.1a generally indicate that over the grid search space the MLP dominates the ensemble of RNN architectures. Throughout the sorted indices, but most importantly at the beginning (left) of the sorted indices, the MLP (blue) and GRU-RNN (green) architectures perform better by a large margin compared with the simple RNN (orange) and LSTM-RNN (red) architectures. This is further shown in Figure 4.1b which illustrates the first ten sorted indices of Figure 4.1a. The loss curves illustrate that on average the best ten models of the simple RNN is the worst of the four architectures and the best ten models of the LSTM-RNN models are a small scale factor better. This result is interesting since the MLP is the baseline architecture and the ensemble of RNNs are designed to handle time series data. Another notable feature of the top ten LSTM-RNN models in Figure 4.1b is the large standard error of the mean calculated from Equation 4.3. This is an indication of significant variance in performance over the 10 models trained per grid search iteration. During brief analysis two LSTM-RNN models trained on the same parameters could illustrate impressive then poor performance. This high variability is not desirable and leads to high average RMSE, but does reveal the capability of the LSTM-RNN if the right set of training parameters can consistently result in a good model.

Further evaluation of the loss curves in Figure 4.1b shows that the best ten MLP and GRU-RNN models are very similar, even crossing each other twice. Of the top ten MLP

and GRU-RNN models, the very best of each (sorted index 0) show that the GRU-RNN is slightly better with a validation average  $\log_{10}(C_n^2)$  of 0.181316 vs. 0.181476 for the MLP. The standard errors are also very similar, 0.000697 vs. 0.000605, for the GRU-RNN and MLP, respectively. Thus the consistency of model convergence for one model is not notably better than the other. Generally the standard error bars of the MLP and GRU-RNN architectures in Figure 4.1b are smaller (better) than the bars of the simple RNN and especially the LSTM-RNN architectures. These results illustrate that of the four architectures, the MLP and GRU-RNN are proving to be best suited for this problem as evaluated on the validation dataset.

#### 4.2.2 Statistical Significance

The results presented in Figure 4.1 clearly show that specific architectures and corresponding training parameters perform better on the validation dataset than others. However, from the top performing models there is little discrepancy in performance metric which introduces ambiguity into which model and parameter combination is the very best. To sort through these similar models is the *Student's t-test* which is a test of whether two sample means are different to a specific level of significance. Performing tests of significance on the results in Figure 4.1b statistically distinguishes the models to show if a model is significantly better than another.

##### *Student's t-test* Foundation

The *Student's t-test* is a statistical test of the null hypothesis  $H_0$  that two samples have equal means. The alternative hypothesis  $H_a$  is that samples do not have equal means. The foundation of the test is as follows. Take one set of measurements, then some event

happens, then take another set of measurements. Did the event, like a change in a control parameter, make a difference? In this work the measurements are model performances on the validation dataset and the event is a change in the model training parameters. There are several variations of the *Student's t-test* including the *independent t-test* for equal and unequal variances, and the *dependent t-test* for paired samples. The *independent t-test* for unequal variances is used in this work because the samples are independent and the variances are not assumed to be equal. This specific test is known as *Welch's t-test* and given samples  $x_A$  and  $x_B$  defines the statistic  $t$  as

$$t = \frac{\bar{x}_A - \bar{x}_B}{\sqrt{\frac{Var(x_A)}{N_A} + \frac{Var(x_B)}{N_B}}}, \quad (4.4)$$

where  $\bar{x}_A$ ,  $Var(x_A)$  and  $N_A$  are the sample A mean, variance and size, respectively. Likewise,  $\bar{x}_B$ ,  $Var(x_B)$  and  $N_B$  are the sample B mean, variance and size. The two-tailed  $p$ -value or significance of this value of  $t$  is calculated with  $dof$  degrees of freedom

$$dof = \frac{\left[ \frac{Var(x_A)}{N_A} + \frac{Var(x_B)}{N_B} \right]^2}{\frac{[Var(x_A)/N_A]^2}{N_A-1} + \frac{[Var(x_B)/N_B]^2}{N_B-1}}. \quad (4.5)$$

The  $p$ -value is a number between 0 (zero) and 1 and is the probability that  $|t|$  (hence two-tailed) could be this large or larger just by chance under the assumption that the null hypothesis  $H_0$  is correct [19]. A very small  $p$ -value ( $\leq 0.05$ ) means that the observed difference in means is very significant and the null hypothesis  $H_0$  is rejected at the 5% significance level. This does not, however, prove that the null hypothesis  $H_0$  is false or that the alternative hypothesis  $H_a$  is true. A low  $p$ -value means *either* that the null hypothesis is true and a highly improbable event has occurred *or* that the null hypothesis is false.

### *Student's t-test* Results

The *Student's t-test* is robustly implemented as a function from *SciPy*, a Python-based open-source software for mathematics, science, engineering, and most importantly in this

case, statistics [20]. Using the `ttest_ind` function and setting parameter `equal_var` to False performs the *Welch's t-test* given two arrays of measurements.

The *t-test* is performed on each of the top ten models in Figure 4.1b where sample A in Equations 4.4 and 4.5 is the 10 validation  $\log_{10}(C_n^2)$  RMSE scores from the best GRU-RNN model. The best model is sorted index 0 in Figure 4.1b. Sample B in Equations 4.4 and 4.5 iterates through the 10 validation RMSE scores of the rest of the models in Figure 4.1b. This results in *p*-values of the best GRU-RNN model evaluated against the next nine best GRU-RNN models and the best ten MLP models, simple RNN models, and LSTM-RNN models. A significance level ( $\alpha$ ) of 0.05 is predefined to reject the null hypotheses  $H_0$  if the *p*-value is  $\leq \alpha$ . Figure 4.2 summarizes these results by plotting the two-tailed *p*-value as a function of the sorted index, the same x-axis as in Figure 4.1b. The *p*-values are again parsed by fundamental architecture. The MLP *p*-values are in blue, simple RNN

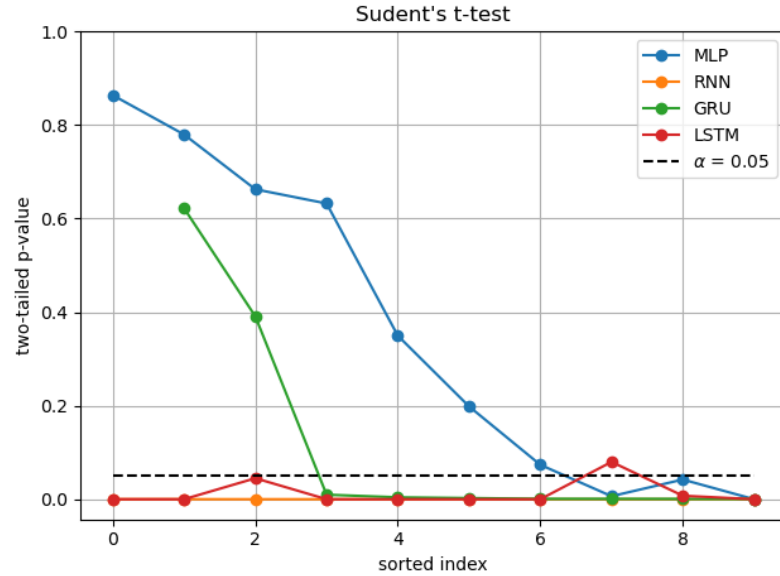


Figure 4.2: *Welch's t-test* of the grid search results

in orange, GRU-RNN in green, and LSTM-RNN in red. The black dashed line in Figure 4.2 is the  $p$ -value threshold  $\alpha = 0.05$ . The GRU-RNN  $p$ -value at sorted index 0 (zero) is omitted because performing the *Welch's t-test* on the best GRU-RNN model against itself is irrelevant.

Any markers below the black dashed line ( $\alpha$ ) in Figure 4.2 represent models whose mean performance is statistically different from the best GRU-RNN model at the 5% significance level, a rejection of the null hypothesis  $H_0$ . Since the best GRU-RNN model is the best performing model in the entire grid search, the models below the  $\alpha$  line are statistically worse at the 5% level. Any markers above the  $\alpha$  line represent models whose performance is not statistically worse, i.e., the null hypothesis  $H_0$  is not rejected at the 5% level. A total of ten markers in Figure 4.2 are above the  $\alpha$  line: two are the next two best GRU-RNN models, seven are the seven best MLP models, and one is the eighth best LSTM-RNN model. The LSTM-RNN model which does not reject the null hypothesis is a result of the high variance in the model illustrated by the large standard error bars in Figure 4.1b at sorted index 8 on the x-axis. Likewise, the standard error bars at sorted index 3 in Figure 4.1b also correspond with the  $p$ -value that is nearly to the  $\alpha$  line in Figure 4.2.

The other markers above the  $\alpha$  line from MLP and GRU-RNN are consistent with the average RMSE scores in Figure 4.1b. The first three GRU-RNN scores in Figure 4.1b hover around 0.182 with the first three MLP scores. Then the GRU-RNN scores step up to nearly 0.184 and steadily increase. The MLP scores steadily rise until the seventh sorted index where there is a notable step above 0.184. The indices of these steps, 3 for GRU-RNN and 7 for MLP, also are the first models where the null hypothesis is rejected at the 5% level. This is illustrated in Figure 4.2 by the GRU-RNN (green) marker at sorted index 3 being

the first GRU-RNN model below the  $\alpha$  line and the MLP marker at sorted index 7 being the first MLP model below the  $\alpha$  line.

### 4.3 Evaluation of Best Models

#### 4.3.1 Comparative Analysis

From the results in Figure 4.2, the top three GRU-RNN models and top seven MLP models are selected for further evaluation because they fail to reject the *Welch's t-test* null hypothesis. The LSTM-RNN model which also does not reject the null hypothesis is not considered for further evaluation because its rejection is explained by the very high standard error. Mentioned above, the indices to sort the validation average  $\log_{10}(C_n^2)$  RMSE scores are used to sort the corresponding grid search parameters. Table 4.1 summarizes the grid search parameters associated with the top three GRU-RNN models. The three rows in

Table 4.1: Top GRU-RNN Model Parameters

Model	Sequence Features	Sequence Length (hours)	Layers	Nodes
GRU-RNN 1	Press, RH, SI, $C_n^2$	12	2	40
GRU-RNN 2	Press, RH, SI, $C_n^2$	12	2	50
GRU-RNN 3	Press, RH, SI, $C_n^2$	12	2	30

Table 4.1 (ignoring the header) represent the best GRU-RNN model, GRU-RNN 1, then the next two best GRU-RNN models, GRU-RNN 2 and GRU-RNN 3. The columns in Table 4.1 sort the grid search parameters into “Sequence Features” which is the input sequence features (variables) used by the model, “Sequence Length (hours)” that is the length of input sequence data used by the model and is reported in number of hours, “Layers” which

is the number of hidden layers used by each model, and “Nodes” which is the number of nodes per hidden layer in each model.

The summary in Table 4.1 is remarkably consistent. The input sequence features used by all three of the best models are pressure, relative humidity, solar irradiance and  $C_n^2$ , the sequence length of each model is 12 hours, the number of GRU-RNN layers for each model is 2, and the number of nodes per GRU-RNN layer is 40, 50, and 30 in order of the top three GRU-RNN models. The consistency of the parameters indicates a specific type of model has been found to best perform on the validation dataset. It is also encouraging that the best three GRU-RNN models use 40 nodes per layer, then 50, and finally 30. If the best GRU-RNN used 50 nodes, for example, a concern would arise of whether the bounds of the grid search were wide enough, i.e., the number of nodes covered in the grid search should have been higher than 50.

Similarly to Table 4.1, Table 4.2 summarizes the grid search parameters for the top seven MLP models. Evaluation of Table 4.2 again yields consistency of the best MLP models. For

Table 4.2: Top MLP Model Parameters

Model	Sequence Features	Sequence Length (hours)	Layers	Nodes
MLP 1	Temp, Press, RH, SI	16	2	30
MLP 2	Temp, Press, RH, SI	16	2	40
MLP 3	Temp, Press, RH, SI	16	2	50
MLP 4	Temp, Press, RH, SI	16	2	20
MLP 5	Temp, Press, RH, SI	12	2	40
MLP 6	Temp, Press, RH, SI	12	2	30
MLP 7	Temp, Press, RH, SI	12	2	50

each of the models the input sequence features are temperature, pressure, relative humidity,

and solar irradiance. The input sequence length is 16 hours for the first four models, then 12 hours for the last three. The number of hidden MLP layers is 2 for all seven models. Finally, the number of nodes is 30, 40, 50, then 20 for the 16 hour sequence lengths (first four models), then 40, 30, and 50 for the 12 hour sequence lengths (last three models).

The consistency of input sequence features in the best MLP models is encouraging because like the best GRU-RNN models, a specific type of MLP model has been found to perform best on the validation dataset. It is also encouraging that the number of hidden layers in the MLP model is consistently 2 across all seven models. The ordering of the sequence lengths and number of nodes per hidden layer in Table 4.2 illustrates that using 16 hours of input sequences and at least 20 nodes per layer is better than using 12 hours of input sequences and at least 30 nodes per layer. Most importantly, though, is shows that that using 12 hours of input sequences and at least 30 nodes is better than 16 hours of input sequences with only 10 nodes. This is an indication that using only 10 nodes per layer in the MLP likely does not yield the model complexity to perform well on the validation dataset.

There are two major distinctions between the best GRU-RNN and MLP models summarized in Tables 4.1 and 4.2. First, the input sequences each only use four features (variables), but the features used by each architecture are different. Both architectures use pressure, relative humidity, and solar irradiance, but the GRU-RNN architecture uses  $C_n^2$  and MLP uses temperature. It is interesting that the use of temperature, one of the most fundamental weather variables and oscillatory in character, is not used by the best GRU-RNN models. It is more interesting, however, that the best MLP models do not use prior  $C_n^2$  measurements as an input. It is expected that the prior  $C_n^2$  measurements would be a significant driver of the model outputs since generally the trend of recent measurements would continue in

the future, so it is curious that the best MLP models deviate from this expectation. The second major distinction is the input sequence lengths. The best GRU-RNN models only require 12 hours of inputs, whereas the four best MLP models require 16 hours of inputs. From a practical perspective, requiring four less hours of input sequences is highly desirable in a real-world application.

In addition to the different input features used by the best GRU-RNN and MLP models, another curious result is that only four input features are used by each architecture when up to six variables are available. To investigate further, the “Sequence Features” column in Tables 4.1 and 4.2 are expanded to evaluate more models, the best 88 (10%) and worst 88 (10%). The simple RNN and LSTM-RNN are also included in this analysis. The number of times each input feature (variable) is used by the best 88 and worst 88 models is recorded per architecture. Figure 4.3 illustrates bar charts of these results. Each category on the

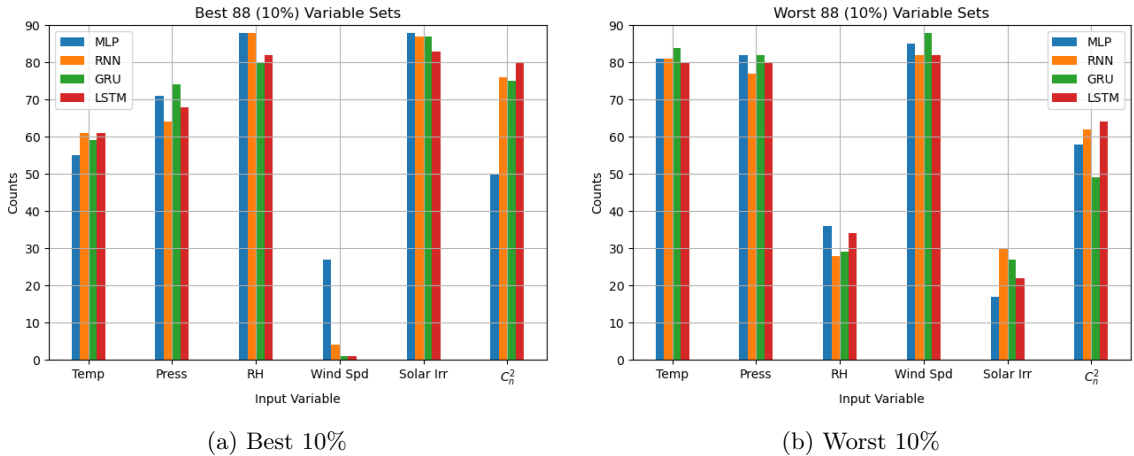


Figure 4.3: Best 10% and worst 10% variable sets.

x-axis is an input feature, and the y-axis is the number of counts. There are four bars for

each category representing the fundamental architectures. The blue bars are MLP, orange bars are simple RNN, green bars are GRU-RNN, and red bars are LSTM-RNN. Figure 4.3a is the counts of each input feature for the best 88 models of each architecture, and Figure 4.3b is the counts for the worst 88 models of each architecture.

Evaluation of best 88 models of each architecture in Figure 4.3a illustrates several interesting results, but one stands out in particular: wind speed is rarely used as an input feature in the best 10% of models. Specifically, the ensemble of RNN architectures almost never use wind speed: the simple RNN uses wind speed four times, and the GRU-RNN and LSTM-RNN models only use wind speed once each. The best 88 MLP models, however, use wind speed just under 30 times. Concurrent evaluation of the worst 88 models of each architecture in Figure 4.3b further reveals information about wind speed: all four fundamental architectures use wind speed in nearly all of the worst 88 models. The ensemble of RNNs almost universally ignoring wind speed in the best models, combined with the almost universal inclusion in the worst models, is strong evidence that the exclusion of wind speed as an input feature for the best GRU-RNN and MLP models is not by chance. Rather, this is conclusive insight that prior wind speeds are not beneficial to the forecasting of  $C_n^2$  in this problem. It is possible that this is due to the large spatial gap between the weather station and  $C_n^2$  path, i.e., the wind conditions at the weather station are not correlated well with the  $C_n^2$  measurements.

For the MLP, the wind speed counts in Figures 4.3a and 4.3b offer some insight into how the MLP is learning compared with the ensemble of RNN architectures. The processing of the RNNs essentially forces the model to learn the input sequences as a function of time, whereas the MLP, which uses the same information in a flattened layer, is free to learn any relationships. Specifically the MLP is not bounded to learn the temporal relationship

between the input variables, thus it is reasonable to theorize that the MLP is more prone to learning relationships that are not as physical.

Two more categories of input features stand out in Figures 4.3a and 4.3b: relative humidity and solar irradiance are nearly universally used in the best 88 models of each architecture, and are seldom used in the worst 88 models of each architecture. This result reveals the opposite conclusion about wind speed: relative humidity and solar irradiance are strong drivers of  $C_n^2$  and the spatial separation between weather measurements and  $C_n^2$  path does not significantly impact the models' performances, i.e., these two variables are reliably transferred across space.

Temperature and pressure in Figures 4.3a and 4.3b are two input features whose counts require careful evaluation. In the best 88 models, temperature has an average around 57 - 58 counts across the four architectures, but has 80+ counts for each architecture in the worst 88 models. Similarly, pressure has around 68-69 counts on average in the best 88 models, and around 80 counts on average in the worst 88 models. The counts in the best 88 models suggest that pressure is not as sensitive to the problem as relative humidity and solar irradiance, and temperature is even less sensitive. The counts in the worst 88 models initially suggest that temperature and pressure are generally poor input features, but the very low counts of relative humidity and solar irradiance influence that conclusion, possibly incorrectly. Because a minimum of four input variables are required by the grid search's bounds, the low counts for relative humidity and solar irradiance already account for the maximum two dropped variables, which means that temperature and pressure by default will often get used as an input to the worst 88 models. This argument is not valid for wind speed because the counts are extremely low in the best 88 models *and* the counts are extremely high in the worst 88 models. As a final note about temperature and pressure, if

the minimum number of input features was set to three instead of four it is possible they would be entirely excluded from the best GRU-RNN models based on the counts in Figure 4.3a, leaving only relative humidity, solar irradiance, and  $C_n^2$ .

The final input feature of discussion in Figures 4.3a and 4.3b is  $C_n^2$ . This is another input feature (wind speed) in which there is a strong difference between MLP and the ensemble of RNN architectures. For the best 88 models,  $C_n^2$  is utilized 75+ times by the ensemble of RNN architectures, but only 50 times by the MLP. Most importantly, though, is that *none* of the best seven MLP architectures from Table 4.2 use  $C_n^2$ . This is further evidence of the fundamental difference between the processing of the ensemble of RNNs and the MLP. It is expected that prior  $C_n^2$  measurements is a strong driver of future  $C_n^2$  and the ensemble of RNNs strongly learn this relationship. The MLP has not learned this relationship as strongly possibly because  $C_n^2$  is only relevant to forecasting  $C_n^2$  if it is processed temporally.

The counts in Figures 4.3a and 4.3b have been shown to behave as a top-level input sensitivity analysis. Many useful conclusions have been derived about how the architectures use the inputs. Further evaluation would require a significant level of time-series analysis which is beyond the scope of this effort.

#### 4.4 Selection of the Best Model and Chapter Summary

The results presented in this Chapter have revealed the best performing model as applied to the validation dataset. By *Welch's t-test* it has been shown to be significantly better than all but nine other models at the 5% level. The best model (GRU-RNN) has been evaluated against the next two best GRU-RNN models to show strong consistency in the model parameters. This same evaluation and result has been shown for the seven MLP models. The next step in this work applies a model to the test dataset so a single model

is chosen. This single model is “GRU-RNN 1” in Table 4.1. It has two GRU-RNN layers with 40 nodes each and uses 12 hours of pressure, relative humidity, solar irradiance, and  $C_n^2$  as input features. This model is chosen for many reasons.

1. It results in the lowest average RMSE as applied to the validation dataset.
2. The next two best GRU-RNN models, which are not significantly different in performance, share the same input features, input sequence length, and number of layers.
3. This model uses 40 input nodes and the next two best GRU-RNN models, which are not significantly different in performance, use 50 and 30 nodes which shows strong consistency.
4. This model requires only 12 hours of input sequences compared with MLP’s requirement of 16 hours for the best models. In a real-world application this is highly desirable.

In addition to the reasons to use the selected GRU model, no evidence has been shown to support the use of an MLP model instead.

## CHAPTER V

### TEST DATASET MODEL EVALUATION

#### 5.1 GRU-RNN Test Dataset Performance Summary

After determining the best model as applied to the validation dataset in Chapter IV, the train and validation datasets are combined into an updated train dataset. The selected model is trained on the updated train dataset and then applied to the test dataset. Like in the grid search, ten individual models are trained for a robust result. Figure 5.1 illustrates the model training process by plotting the  $\log_{10}(C_n^2)$  RMSE loss (evaluated between forecast and measured truth) as a function of training epoch. The blue curves represent each model's

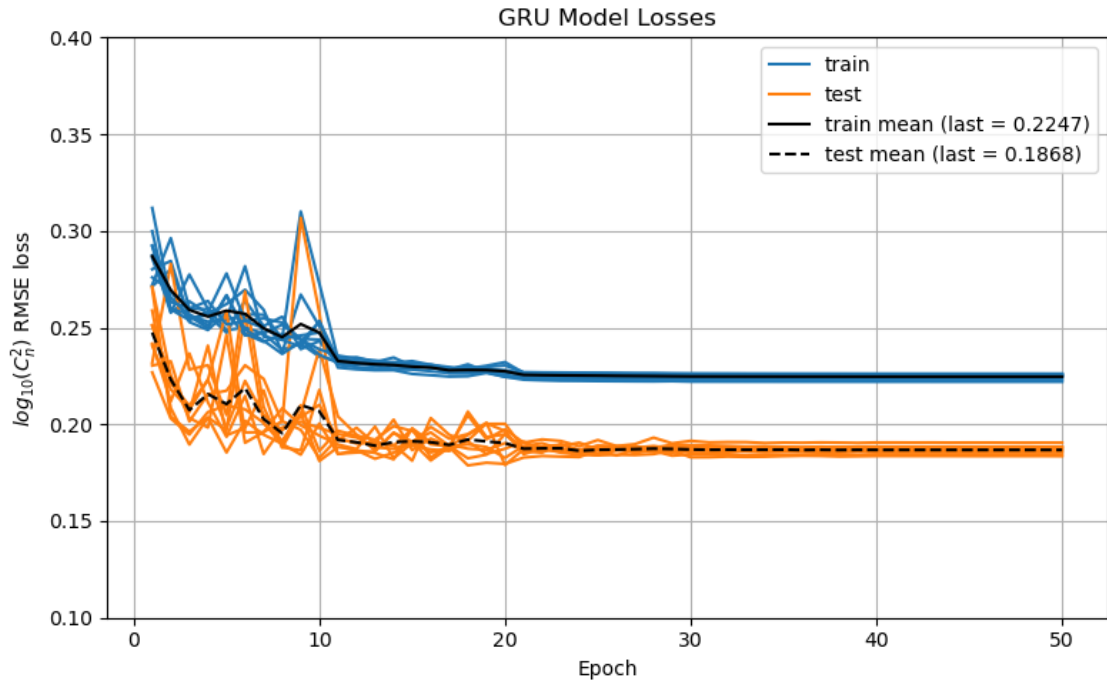


Figure 5.1: GRU-RNN train and test loss curves of 10 models.

performance on the train dataset and the orange curves represent the performance on the

test dataset. The solid and dashed black lines are the per-epoch average of the train and test dataset performances, respectively. The loss curves in Figure 5.1 indicate that convergence rates of the models as applied to the train and test datasets are consistent with each other, an indication that the test dataset is a good representation of the train dataset. This is further illustrated by bumps in the loss scores in both train and test loss curves like the single blue and orange spike at epoch 9. The per-epoch variability in the test dataset is higher than the train dataset since the test dataset is much smaller and thus more prone to changes in loss score with an update in model parameters. The 50th (last) epoch loss scores averaged over the ten models are reported in the legend as 0.2247 and 0.1868 for the train and test dataset, respectively. The standard deviations of the 50th (last) epoch loss scores for the train and test datasets are 0.0013 and 0.0020, respectively. As a point of comparison, the best MLP model was also trained then applied to the test dataset ten times. The average 50th epoch loss scores are 0.2457 and 0.1938 with standard deviations of 0.0027990 and 0.0020191 for the train and test dataset, respectively. These results indicate that as applied to the test dataset, on average the chosen GRU-RNN model is better than the best MLP model by a large margin, further validating the selection of the GRU-RNN model. The standard deviations of the test dataset loss scores are nearly identical, indicating the stability of the models are similar.

Another way to visualize model convergence is to apply the ten individually-trained models to the test dataset and parse performance by test date. The test dataset spans 08/03 and 08/05 - 08/10, so each model is evaluated on these seven days. The  $\log_{10}(C_n^2)$  RMSE loss scores as a function of test date are illustrated in Figure 5.2. Evaluated over the ten models, in black is the mean, red the mean  $\pm$  the standard deviation, and blue the minimum and maximum scores. The day-to-day change in average error score, illustrated

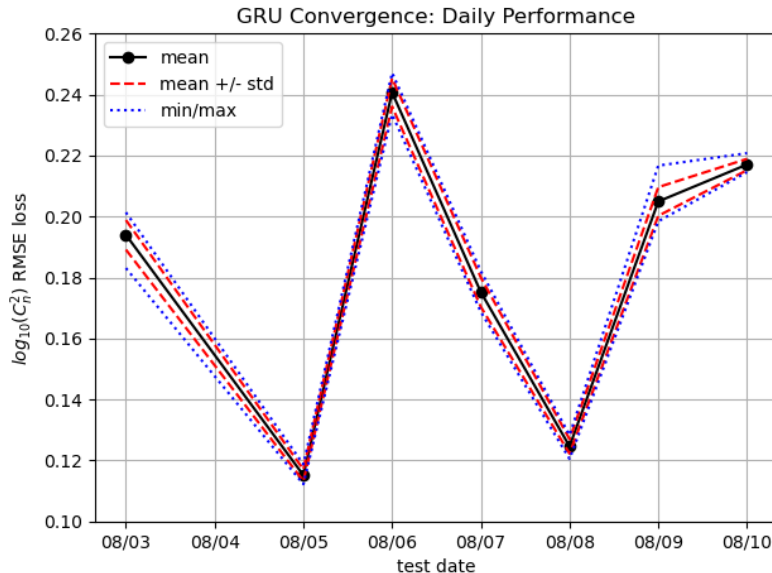


Figure 5.2: GRU-RNN daily summary performance: mean, standard deviation, and min/max.

by the large jumps in error score like from 08/05 to 08/06, indicate that model performance varies by daily  $C_n^2$  conditions. However, the tightness of the red and blue curves about the black markers indicate the models are converging to consistent solutions when evaluated on a daily basis. On a single date, the largest difference between minimum and maximum loss scores is just less than 0.02 on 08/03 which is still a small variation in model performance for a given day. On 08/05 and 08/08 the red and blue lines are on top of the black markers indicating the model convergence is highly consistent when applied to these two dates. These day-by-day results further confirm the interpretation of the test dataset loss curves in Figure 5.1 which indicate the models converge to a consistent solution when applied to the entire test dataset.

Another visualization of average model performance from the ten model ensemble is presented in Figure 5.3 which is the  $\log_{10}(C_n^2)$  RMSE loss score of the test dataset parsed

by the first timestamp in each forecast. To make the plot in Figure 5.3, the 148 forecasts in the test dataset are sorted by the time of day of the first timestamp in the forecast. The black markers are the loss scores of each model (from the ensemble of ten) applied to each of the 148 forecasts. The location of the markers on the x-axis represents the first timestamp of the forecast. The average of the ten loss scores for each forecast are plotted as red markers. For example, evaluating the 06:00 (far left) time of day in Figure 5.3 shows six red markers.

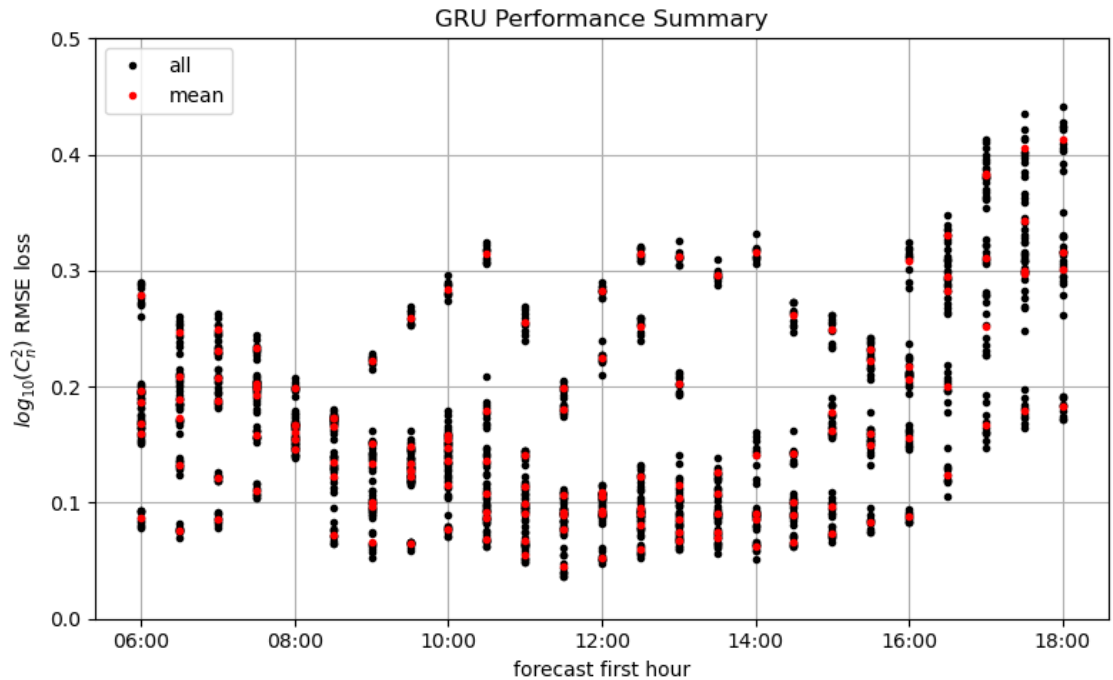


Figure 5.3: GRU-RNN hourly summary performance: individual and average.

This means that in the test dataset there are six forecasts whose first timestamp is at 06:00, and each red marker is the average loss (from the ten-model ensemble) for each of the six forecasts. The black dots at 06:00, of which there are 60 markers, are the loss scores for each of the six forecasts for each of the ten models. Note there are only six average (red) markers and 60 total (black) markers because in the seven-day test set there are only six

forecasts starting at 06:00. In fact, the first forecast on 09 August is not until 10:00, so 10:00 is the first time with seven red markers and 70 black markers.

Still evaluating the 06:00 time of day, there is one red marker around 0.275 on the y-axis that is on top of a cluster of black points. This individual red marker is the average of the black markers which surround it. Thus, this cluster of black markers and their average, the red marker, is an evaluation of the ensemble model performance on one of the six forecasts whose first timestamp is at 06:00. Overall, Figure 5.3 shows 148 red markers for the 148 forecasts in the test dataset, and 1480 black markers for the ten models per 148 forecasts.

Figure 5.3 is a summary of model performance as a function of time of day. The trends indicate that best model performance starts around 0.2 (on the y-axis) in the beginning of the day, drops down to around 0.1 in the middle of the day, then rises in the evening to around 0.3. The morning forecasts tend to be around the overall test dataset performance, about 0.18 to 0.20. On average, best performance is in the middle of the day between 11:00 and 15:00 since most of the black and red markers are clustered around 0.1 on the y-axis. In this window a few forecasts are consistent outliers in terms of error score indicated by the red markers also being an outlier from the trend. These individual forecasts are of interest for analysis. The high error scores at the end of the day, 16:00 to 18:00, is indicative that there are features of these late-day forecasts which are present in the measurements but are consistently not being captured by the ensemble of models. Generally, Figure 5.3 indicates the model performs best in the middle of the day, slightly worse in the morning, and generally poorly in the late afternoon and evening.

## 5.2 Daily $C_n^2$ Forecasts

After the ensemble study of the GRU-RNN models applied to the test dataset, a single GRU-RNN model is applied to the test dataset and carefully evaluated in this section. Figures 5.4 and 5.5 are daily- $C_n^2$  plots of the test forecasts and measured truth as a function of local time. Figures 5.4a, 5.4b, 5.4c, and 5.4d plot the forecasts on 08/03 and 08/05 - 08/07, respectively. Figures 5.5a, 5.5b, and 5.5c plot the forecasts on 08/08 - 08/10, respectively. Each daily- $C_n^2$  plot contains multiple curves. The black curve represents the truth  $C_n^2$  measured conditions. The other curves which transition in color from cyan to magenta represent the model forecasts throughout the day. The brightest cyan is the earliest forecast in the day, and the brightest magenta is the latest forecast in the day. The forecasts in between are appropriately colored to smoothly transition between the two end colors. The colorbar of each plot in Figures 5.4 and 5.5 illustrate the curve color scheme by labeling the forecast's first timestamp next to the color with which it is associated. Additionally, the  $\log_{10}(C_n^2)$  RMSE loss score between each forecast and measured truth is also labeled in parenthesis next to the colorbars. For example in Figure 5.4a, the earliest forecast's (furthest left) first timestamp is at 06:00 and is correspondingly labeled in the colorbar as 06. The color of this earliest curve is brightest cyan which is consistent with the label on the colorbar. The error score for this forecast is 0.282. Likewise, the last forecast of the day in Figure 5.4a is at 17:00 and is the brightest magenta curve. The colorbar label is 17 and is the top color in the colorbar. The loss score for this individual forecast is 0.316. Note that in these daily- $C_n^2$  plots only the forecasts whose first timestamp is at the top of the hour are illustrated. This is done purely for aesthetics to avoid cluttered plots.

The daily- $C_n^2$  plots in Figure 5.4 illustrate many unique features. Starting with 08/03 in Figure 5.4a, the morning (cyan) forecasts all forecast a similar trend in  $C_n^2$ : a steady

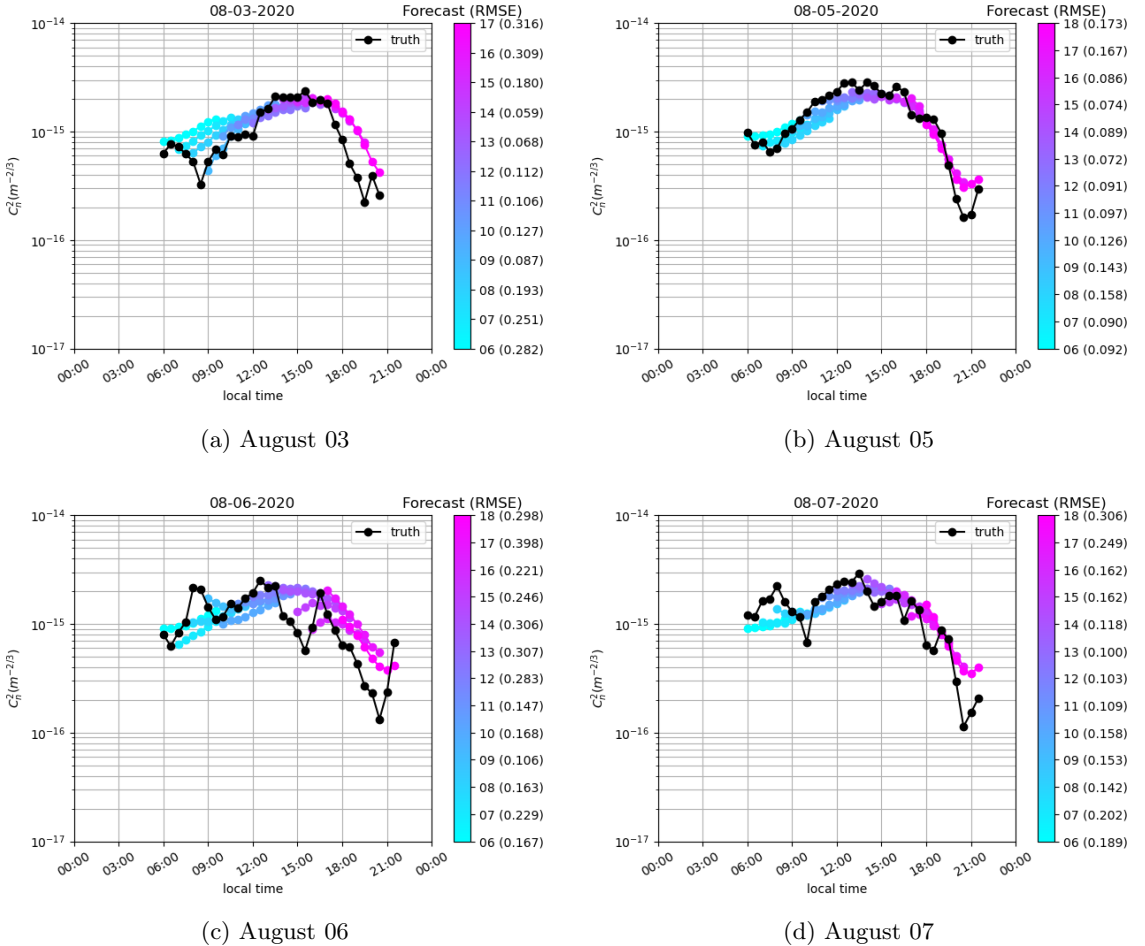


Figure 5.4: August 03 and 05 - 07 daily  $C_n^2$  forecasts.

rise. Interestingly, the magnitude of the forecasted conditions seems to be different by a scale-factor between the first three forecasts at 06:00 - 08:00. This illustrates the impact of including prior  $C_n^2$  conditions as an input sequence into the model. At the 07:00 and 08:00 forecasts, the model is given information that the most recently measured  $C_n^2$  is trending down in magnitude. So the forecasts, while still trending upward, lowers in overall magnitude because the model has learned that its forecast should start near the most recently measured conditions. This feature is consistently seen throughout all test forecasts. An-

other interesting feature is the evening forecasts in Figure 5.4a. The 15:00 - 18:00 forecasts predict  $C_n^2$  to significantly weaken in magnitude starting around 18:00 until 20:30. The measured strengths significantly weaken, but temporally earlier than predicted. This is a rare case where the model gets the evening neutral event magnitude mostly right but misses the temporal component. Generally, the model on this day forecasts a mostly standard diurnal trend, but the measurements are weather impacted. At 10:00 there is a slight drop in measured turbulence, then from 10:30 - 12:00 the measured conditions are steady around  $9 \times 10^{-16}(m^{-2/3})$ . A standard diurnal trend occurs from 12:30 to 17:00, and the model accurately forecasts this.

Forecasts on 08/05 in Figure 5.4b are consistent with a standard diurnal trend. Specifically, the forecasts accurately predict the weak morning neutral event indicated by the drop in  $C_n^2$  around 07:00 to 08:00 then a steady rise in strength until 12:00. The forecasts predict slightly lower  $C_n^2$  strength than measured, but the difference is small. The forecasts then accurately predict the drop in  $C_n^2$  strength starting around 15:00. These forecasts are accurate temporally and in strength of neutral event until the deepest part around 21:00. The measured  $C_n^2$  strength continues to drop but the model does not reach this depth. However, the model does accurately forecast the slight rise in  $C_n^2$  at the very end of the day. Every forecast in Figure 5.4b has an error score lower than the average error score of 0.1868 from the ten model ensemble as applied to the entire test dataset. More specifically, 8 of the 12 forecasts have error scores less than 0.01. These scores indicate that 08/05 is an illustration of great model performance for an entire day.

Model performance on 08/06 in Figure 5.4c is the worst of the seven test days (see Figure 5.2). The first three forecasts of the day at 06:00 - 08:00 have average to above-average error scores because the forecasts predict a steady rise in  $C_n^2$  strength which generally is

measured, but a weather-induced rise in  $C_n^2$  strength at 08:00 is not captured. The 09:00 forecast, which is the lowest error score of the day at 0.106, benefits from knowledge of the prior  $C_n^2$  measurements as an input. The forecast starts high, around  $2 \times 10^{-15}(m^{-2/3})$ , drops down in  $C_n^2$  strength then continues upward in  $C_n^2$  strength with the other forecasts which is accurate with the truth measurements. Forecast performance is poor again starting at 14:00 because another weather-induced turbulence event has occurred, but this time it is a 2-hour drop in  $C_n^2$  strength which the forecasts beforehand do not predict. The 15:00 forecast is the first to see the prior measured  $C_n^2$  conditions which include the weather event and so the model tries to compensate for the suddenly-lower  $C_n^2$  strength by starting lower then rising for a few timestamps to reach the conditions it expects around this time. The 16:00 forecast captures the first timestamp, but misses the very high strength  $C_n^2$  at 15:30, then sharp and consistent drop in  $C_n^2$  as part of the evening neutral event from 15:30 till 20:30. The 17:00 and 18:00 forecasts also miss this long and deep evening neutral event. Overall, 08/06 illustrates where the model struggles: highly-weather impacted conditions.

The fourth test day, 08/07 in Figure 5.4d, illustrates a unique combination of forecasts. In the morning, the model forecasts a slow rise in  $C_n^2$  strength until around 13:00 which is generally consistent with measurements, but does not predict the weather-induced rise in  $C_n^2$  at 08:00 then subsequent drop at 10:00. These two events are very short, only consisting of a single timestamp (30 minutes) each. After this mini-event, the measured conditions are generally diurnal trend through 19:00. There are a few dips in measured  $C_n^2$  strength but they are high frequency and bounce back to a normal diurnal trend which the model accurately forecasts. The forecasts from 11:00 through 14:00 all have error scores below 0.15, well below the average on the entire test dataset of 0.1868 from the ensemble results. The forecasts at 17:00 and 18:00 have high error scores because the model does not accurately

predict the extremely sharp drop in  $C_n^2$  strength from  $7 \times 10^{-16}(m^{-2/3})$  at 19:30 to about  $1 \times 10^{-16}(m^{-2/3})$  at 20:30, only 1 hour later. These late forecasts accurately predict the slight rise in turbulence at 21:00 and 21:30 after the deepest part of the evening neutral event, but the error scores are high because the model could not reach the depth. The 18:00 forecast is a good example of the model accurately forecasting the temporal nature of turbulence conditions but missing the very low magnitude of the neutral event.

The final three test days, 08/08 - 08/10, are presented in Figures 5.5a, 5.5b, and 5.5c, respectively. On average over the ten model ensemble study, 08/08 is the second best day of model performance. Throughout the day, the model generally predicts diurnal trend: a slow rise in  $C_n^2$  strength until around 15:00 when conditions steady then start to decrease again. The 09:00 through 13:00 forecasts all yield low error scores with 4 of them below 0.01. The first three forecasts from 06:00 through 08:00 have error scores around the ensemble average due to two factors. The 06:00 forecast first predicts turbulence conditions around  $1 \times 10^{-15}(m^{-2/3})$ , which is the nighttime filled  $C_n^2$  strength, but the measured conditions are actually low. Then the 06:00 forecast altogether misses the weather-induced sharp rise in turbulence conditions from 07:00 to 08:30. The 07:00 and 08:00 forecasts also miss this high-frequency event. It is not until the 09:00 forecast which has the information about the prior turbulence conditions that the forecasts accurately settle into the diurnal trend.

From the ten model ensemble study, average model performance on 08/09 ranks 4/7 and is also one of the most variable from model to model (Figure 5.2). Analysis of the forecast  $C_n^2$  conditions in Figure 5.5b illustrate how an average over the entire day can be misleading. The first forecast at 10:00 has an error score of 0.136 which is below the ten model ensemble average (0.1868), then the 11:00 - 15:00 forecasts each boast error scores less than 0.01. The measured conditions are mostly diurnal and is accurately forecasted

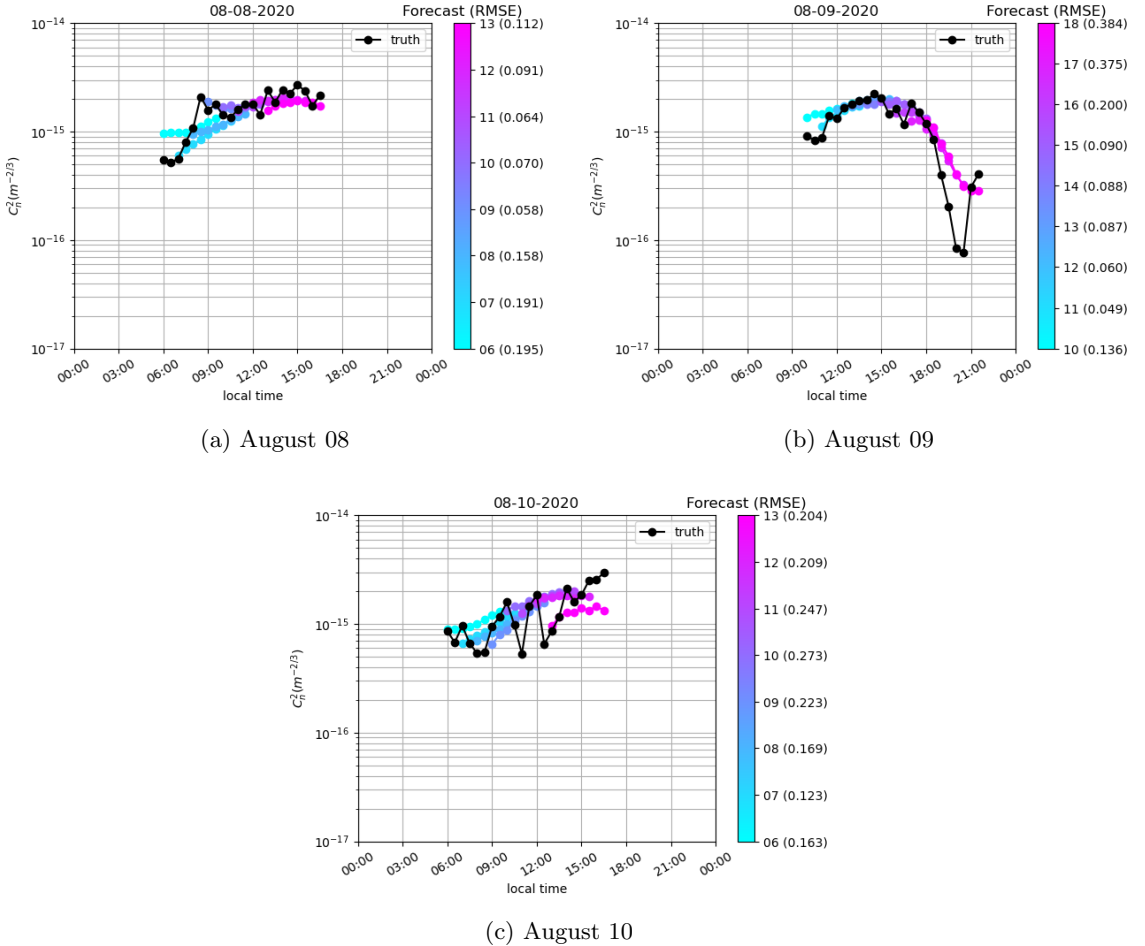


Figure 5.5: August 08 - 10 daily  $C_n^2$  forecasts.

by the model. The only deviations are the very slight morning neutral event from 10:00 to 11:00 then a weather-induced slight drop in  $C_n^2$  strength around 16:00. The two forecasts which raise the day's average error score are at 17:00 and 18:00. These forecasts accurately predict the temporal nature of the evening neutral event, but strongly miss the sharp decline and depth of the event. From 18:00 to 20:00, measured  $C_n^2$  strength drops from just over  $1 \times 10^{-15}(m^{-2/3})$  to  $8 \times 10^{-17}(m^{-2/3})$ , over 1 order-of-magnitude change. In fact, this evening neutral event is just one of only a handful of cases in the entire dataset in which

the evening neutral event dips below  $1 \times 10^{-16} (m^{-2/3})$ . The 17:00 and 18:00 forecasts yield error scores of 0.375 and 0.384, respectively, which are two of the highest error scores in the entire test dataset. Beside this uncharacteristically deep neutral event, model performance on 08/09 is notably better than average.

The last day of the test dataset, 08/10, is the second worst day of model performance from the ten model ensemble average in Figure 5.2. The morning forecasts, which begin at 06:00, generally all predict standard diurnal trends: a slow increase in  $C_n^2$  strength through about 15:00 then a decline. The measured conditions, however, are highly variable both temporally and in  $C_n^2$  strength. Between 06:00 and 15:00 there are five instances of a drop in  $C_n^2$  strength. Likely, at least four of them are weather-induced (possibly the 08:00 is morning neutral event). The model forecasts a diurnal trend which follows the trend of the high-strength  $C_n^2$  points over this time period. The 12:00 and 13:00 forecasts predict  $C_n^2$  strength to lower as the afternoon moves into early evening, but the measured conditions actually rise to the highest point in the entire day from 15:30 to 16:30. The 13:00 forecast starts at a lower  $C_n^2$  strength than the surrounding forecasts due to the model having the input sequence information about the very low  $C_n^2$  strength at 12:30. This day again illustrates the model's inability to accurately forecast high-frequency weather-induced  $C_n^2$  fluctuations. Instead, the model has learned a trend in  $C_n^2$  based on the time of day. The model has also learned to adjust its starting  $C_n^2$  strength based on prior  $C_n^2$  measurements, then settle back into the expected trend.

### 5.3 General Forecast Analysis

The model forecasts and corresponding truth measurements from Figures 5.4 and 5.5 are rearranged by forecast length. Figure 5.6 presents a scatter plot of measured  $C_n^2$  on

the x-axis and forecasted  $C_n^2$  on the y-axis for each time in the 4-hour model forecasts: 0.5 hour, 1 hour, 1.5 hour, and so on through 4 hours. In each scatter plot, the black markers are the truth values plotted as measured  $C_n^2$  vs. measured  $C_n^2$  to yield the linearly arranged markers. The green markers are the model forecast at the scatter plot's designated forecast time plotted as forecasted  $C_n^2$  vs. measured  $C_n^2$ . These scatter plots are visually evaluated by how closely the green markers cluster around the black markers. A set that is well clustered around the black points is better than a set that is not well clustered. If the model was perfect, the black markers would directly overlay the green markers. The average  $\log_{10}(C_n^2)$  RMSE loss is reported in each legend as a quantitative metric of model performance at each forecast time step.

The scatter plot of the first forecast time, 30 minutes, in Figure 5.6a shows a strong clustering of the model forecasts about the measured  $C_n^2$ . Excluding one outlier, the range of measured  $C_n^2$  the model is tasked with forecasting is only from  $5 \times 10^{-16}(m^{-2/3})$  to  $3 \times 10^{-15}(m^{-2/3})$ , a narrow window. This forecast time also benefits from being closest to the most recently measured  $C_n^2$  and other input sequence variables. Thus, it is expected for this forecast time to do well overall. The RMSE loss score is 0.128, well below the ten model ensemble average over the whole dataset of 0.1868. The scatter plot of the second time of the model forecasts, 1 hour, in Figure 5.6b shows a slightly worse performance than the 30 minute forecast time. The set of measured points looks very similar to that of 30 minutes, but the clustering of the green model markers about the black truth markers is not as tight. The error score of 0.157 confirms this visual analysis.

The 1.5 and 2 hour forecasts in Figures 5.6c and 5.6d start to clearly show a different set of measured  $C_n^2$  conditions illustrated by the additional black markers toward the middle and lower left corner of the scatter plots. Most of the green model markers have

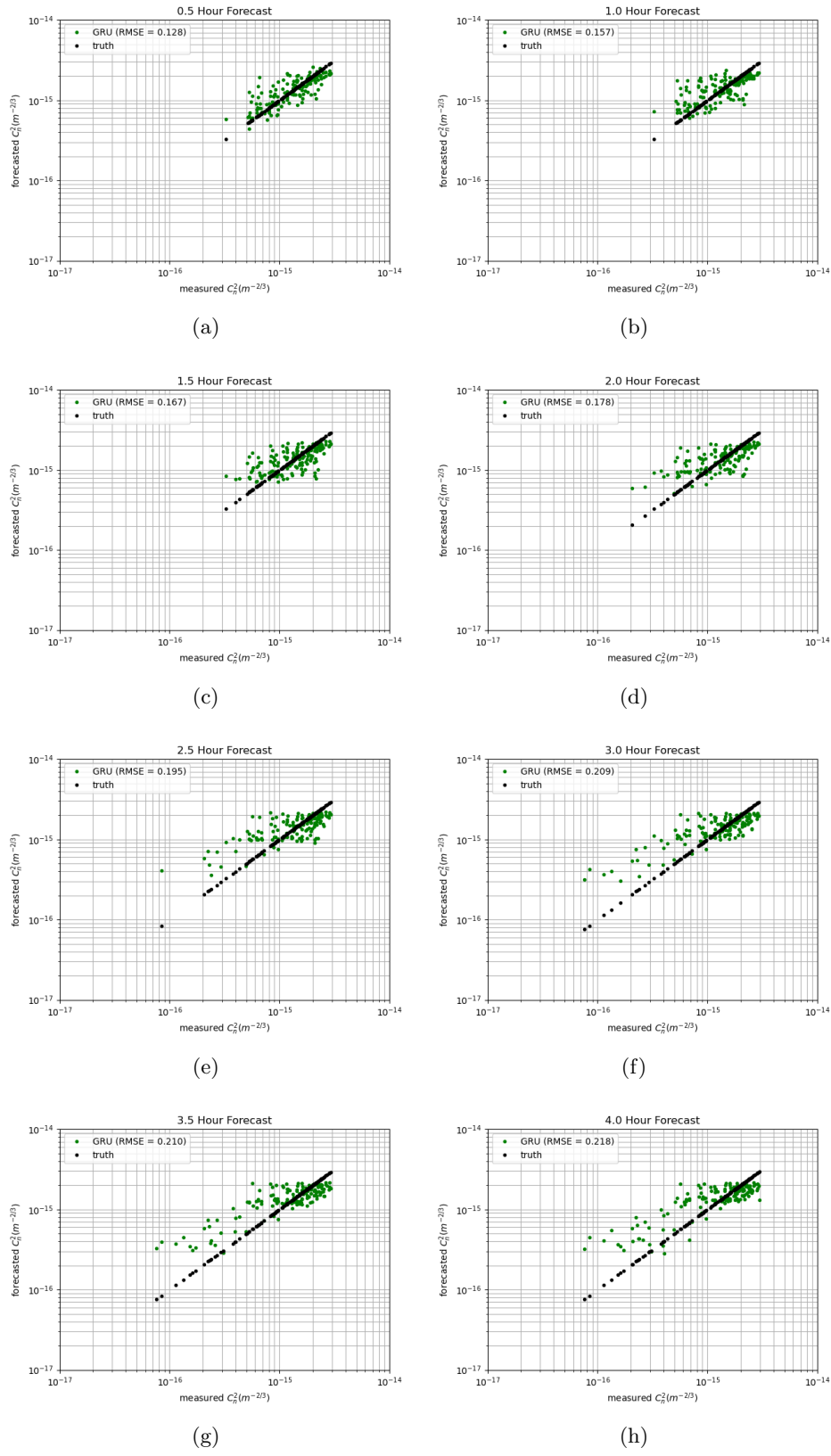


Figure 5.6: Scatter plots.

a reasonable cluster around the mid- and high-strength  $C_n^2$  black markers. However, the model struggles to capture measurements below  $7 \times 10^{-16}(m^{-2/3})$  as illustrated by the black markers continuing left on the x-axis below this strength, but the green markers staying above  $7 \times 10^{-16}(m^{-2/3})$  on the y-axis in Figure 5.6c. In Figure 5.6d is a similar trend, but a couple of model points are beginning to drop into lower strength  $C_n^2$  conditions. The average error scores continue to climb, reaching 0.167 and 0.178 at the 1.5 and 2 hour forecast times, respectively.

The 2.5 and 3 hour forecasts in Figures 5.6e and 5.6f further shown a different set of measurements the model attempts to forecast. Most notable are the increased number of low-strength  $C_n^2$ . As forecast time extends further out the number of evening neutral events included in the examined sets also increases. The clustering of the higher-strength  $C_n^2$  conditions continues to slightly deteriorate. The clustering of the green model markers is not as tight about the black truth markers, and more importantly the slope of these green markers is angling more with respect to the slope of the black markers. At low-strength  $C_n^2$  evening neutral events the model is still struggling to forecast  $C_n^2$  that reaches the measured strength. One positive element of these scatter plots is that there are no green markers which are wildly off from its corresponding black marker. For example, there are no green modeled markers at  $2 \times 10^{-15}(m^{-2/3})$  when its black marker is nearing  $1 \times 10^{-16}(m^{-2/3})$ . This means the model has generally learned the turbulence conditions well, understanding when to forecast high, medium, and low-strength  $C_n^2$ . The error scores for the 2.5 hour and 3 hour forecasts are 0.195 and 0.209, respectively, which follows the trend of increasing error with forecast length.

Finally, the 3.5 and 4 hour forecasts in Figures 5.6g and 5.6h continue to illustrate the trend shown so far: the set of measured  $C_n^2$  to forecast further evolves to include

more evening neutral event low-strength conditions. Interestingly, the group of green model markers around the higher-strength  $C_n^2$  is very well clustered with itself, but is at a significant angle with respect to the black truth markers' angle. The model's struggle to capture the deep neutral events is most clearly observed in Figures 5.6g and 5.6h. The model still has learned when to forecast low-strength  $C_n^2$ , but cannot reach the required depth. The average loss scores for the 3.5 and 4 hour forecasts are 0.210 and 0.218, respectively.

Summarizing the scatter plot error scores from Figure 5.6 is Figure 5.7 which plots the loss scores as a function of forecast length. The plot illustrates that as the forecast length increases so does the model performance error. This is an expected result as any forecasting application is expected to decline in performance as forecast time increases.

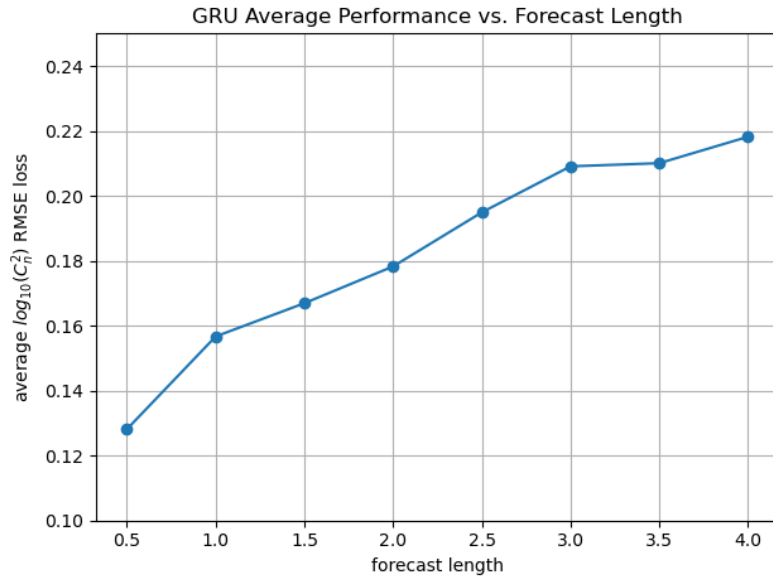


Figure 5.7: Average performance as a function of forecast length.

## 5.4 Individual Forecast Analysis

The final analysis of this model is to understand why it performs well and poorly in specific cases. This section uses the cumulative distribution function (CDF) to statistically illustrate the model's strengths and weaknesses. The CDF is a tool which sorts the given data by magnitude then assigns each sorted data point a percentile from zero (noninclusive) to one (inclusive). The percentile represents the percentage of data points that are less than or equal to the data point's magnitude.

### 5.4.1 Examining 2020/08/09 18:00 EST

A single trend has been abundantly clear throughout the model analysis: the model struggles to capture the deep evening neutral events. In Section 5.2, Figure 5.5b, one of the worst model forecast in terms of RMSE (0.384) is the August 9th 18:00 EST forecast. This is the latest forecast of the day (and all days) and the deep neutral event was noted above to be one of the deepest in the entire dataset, making it an excellent candidate for further analysis which goes as follows.

First, every forecast and input sequence from the train dataset is gathered whose first timestamp matches the forecast in question, 18:00. There are a total of 40 train forecasts whose first timestamp is 18:00. Next, the 40 train forecasts are sorted by measured (truth)  $C_n^2$  magnitude at each timestamp in the 4-hour forecast, so in this case that yields a 40 x 8 array where each column is sorted by magnitude. The CDF is then computed per timestamp, yielding eight CDFs in this case where percentiles are associated with specific  $C_n^2$  strengths. Finally, the CDFs of  $C_n^2$  values are interpolated to subjectively selected percentiles of 20%, 50%, and 80% for each timestamp, yielding a 3 x 8 array of  $C_n^2$  values.

The next step in this analysis applies the trained model to the 40 training input sequences associated with the forecasts just evaluated to CDF 20%, 50%, and 80%. The exact same process just described - sorting the  $C_n^2$  values per timestamp, calculating the CDF, then interpolating to the desired percentiles - is performed on the 40 model forecasts.

Figure 5.8 illustrates the results of this analysis.  $C_n^2$  is plotted as a function of local time of day, where the only forecasts considered are those whose first timestamp is at 18:00. The black markers represent the train dataset truth (measured)  $C_n^2$  at each timestamp. Thus at 18:00, 18:30, and so on through 21:30 there are 40 black markers each. The solid blue, orange, and green lines with circle markers represent the CDF 20%, 50%, and 80%, respectively, of the truth  $C_n^2$  at each timestamp. The dashed blue, orange, and green lines with “X” markers represent the CDF 20%, 50%, and 80%, respectively, of the model forecast  $C_n^2$  at each timestamp. Finally, the solid red and purple lines with “+” markers represent the truth  $C_n^2$  and model’s prediction of the test forecast whose first timestamp is 08/09 18:00.

The analysis in Figure 5.8 reveals that the model has generally learned the ability to forecast  $C_n^2$  from prior weather measurements very well, but lacks the ability to forecast extreme scenarios like the deep neutral event on 08/09. This is illustrated in the plot by comparing the solid and dashed lines of the same colors. Comparing the solid and dashed orange lines, which represent the CDF 50% of the truth and model forecasts, shows that the model has learned the relationship between input sequences and output forecasts because the two lines are nearly on top of each other. However, the dashed blue line is generally a scale factor above the solid blue line, and similarly the dashed green line is a scale factor below the solid green line. This indicates that even when the model is applied to the train

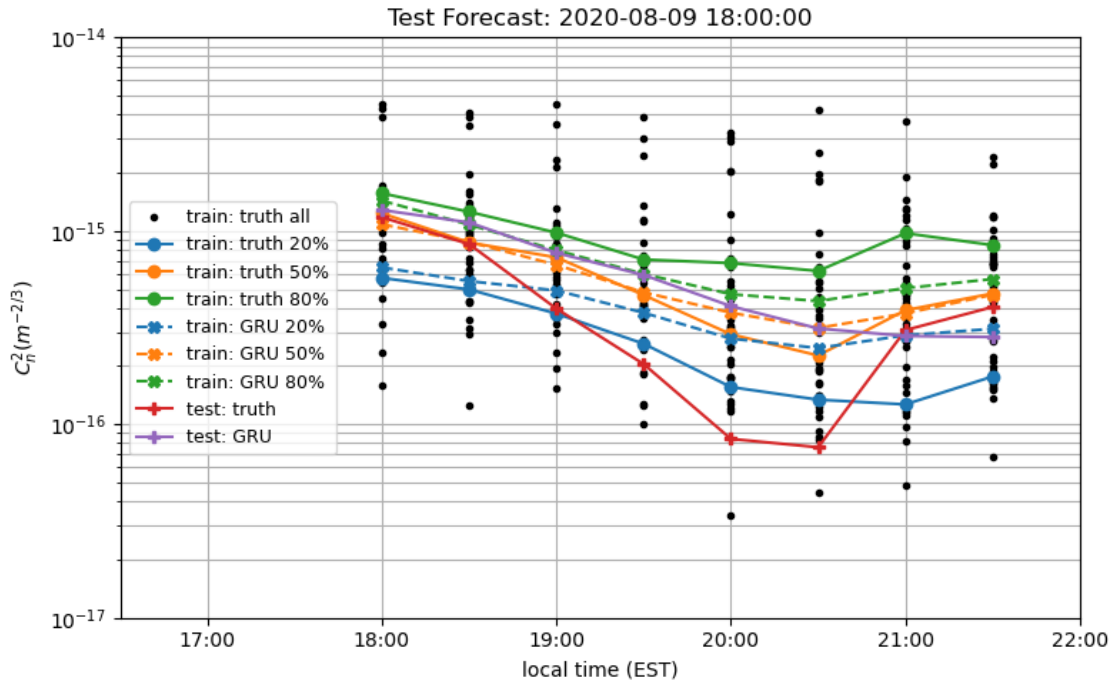


Figure 5.8: GRU-RNN performance analysis of the August 9th 18:00 EST forecast.

dataset, a biased result, the model cannot forecast very high and low  $C_n^2$  conditions from the measurements.

Figure 5.8 also reveals why the model performs so poorly on the August 9th 18:00 EST forecast. The solid red line, which is the truth, starts almost at the truth CDF 80% line (solid green) at 18:00 then proceeds to fall below the truth CDF 20% line (solid blue) at 19:30, 20:00, and 20:30. The model's August 9th 18:00 EST forecast (solid purple line) starts very closely with the truth (solid red line) but does not match the steep decline in measured  $C_n^2$  strength. Interestingly, the model's forecast does fall to the CDF 20% of the model's output on train data (dashed blue line) but takes the entire 4-hour forecast to do so. This is an indication that the model has learned that  $C_n^2$  is expected to be low, but does not have the ability to forecast the very deep events.

### 5.4.2 Examining 2020/08/06 14:00 EST

Another example of poor model performance on the test dataset is the August 6th 14:00 EST forecast from Figure 5.4c. This forecast is chosen for further analysis because it is an example of poor performance (RMSE is 0.306) that does not incorporate an entire neutral event. Rather, this forecast is in the middle of the day when  $C_n^2$  trends are typically very diurnal. Figure 5.9 illustrates the same analysis described above. The most revealing as-

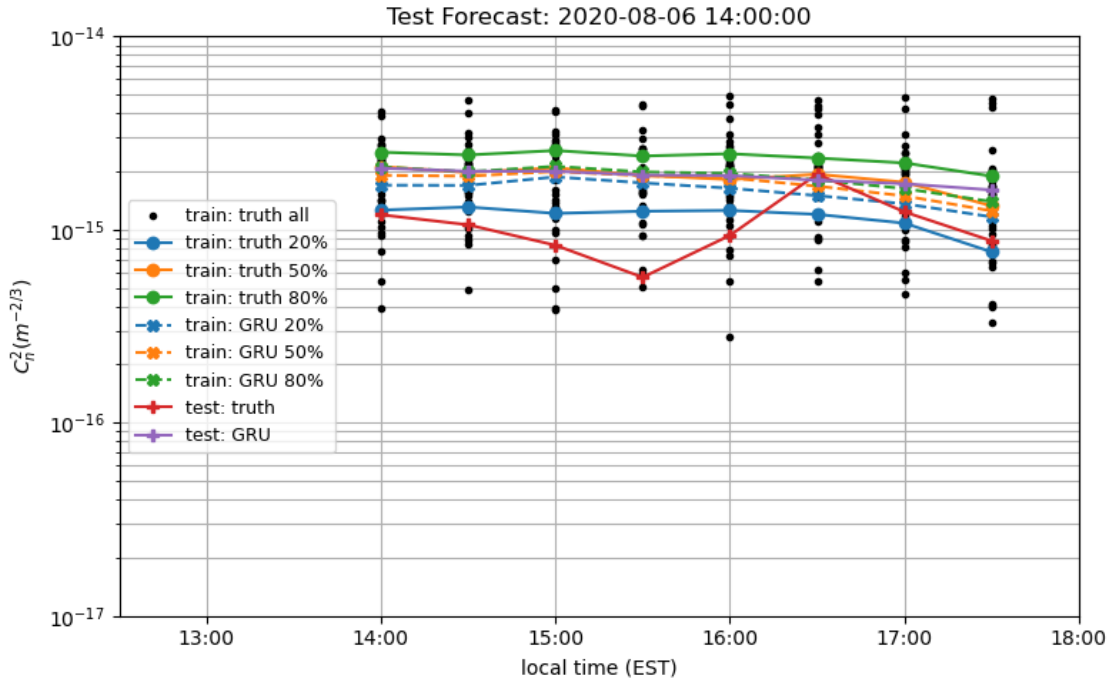


Figure 5.9: GRU-RNN performance analysis of the August 6th 14:00 EST forecast.

pect of Figure 5.9 is that the bounds of the truth CDF 20% and 80% (solid blue and green lines) are very narrow, generally separated by a factor of 2. Furthermore, the train dataset model CDF 20% and 80% (dashed blue and green lines) are nearly on top of each other. The proximity of the CDF percentile lines are so close that the CDF 50% lines are covered

throughout most of the plot. This evaluation further shows that the model has generalized the  $C_n^2$  conditions similarly to the August 9th 18:00 EST forecast analysis above. In this case the bounds are especially narrow since the model has learned to generalize *and* the bounds of the measured conditions at this time are narrow. Thus, Figure 5.9 clearly shows that the model’s performance on the August 6th 14:00 EST forecast is poor because the measurements throughout this time are in the extremes of all training conditions. Specifically, the first five time steps from 14:00 through 16:00 of the truth (solid red line) are below the truth CDF 20% line (solid blue). Especially at 15:30, the  $C_n^2$  measurement is the second lowest of any measurement in the train dataset evidenced by only one black marker being below the red marker.

#### 5.4.3 Examining 2020/08/05 16:00 EST

The final test forecast analyzed using this CDF method is the August 5th 16:00 EST forecast from Figure 5.4b. This forecast is chosen to illustrate an example of a model’s good forecast with respect to RMSE score, a low 0.086 in this case. Like the two prior examples, the bounds between the truth CDF 20% and 80% lines is narrow throughout the forecast. There is a slight increase in width from about a factor of 2 at 16:00 to more than a factor of 3 at 19:30 but is not significant over the course of the forecast. Also like the prior examples, the model forecast CDF 20% and 80% lines (dashed blue and green) are again narrower than the truth CDF lines, further indication of the model’s generalization. The model forecast CDF 50% line (dashed orange) nearly overlaying the truth CDF 50% line (solid orange) also further indicates that the model has learned the general  $C_n^2$  forecast at this time of day from the train dataset and is effectively applying it to the test dataset. Model performance on this test forecast is good because the truth (red line) mostly oscillates about the model

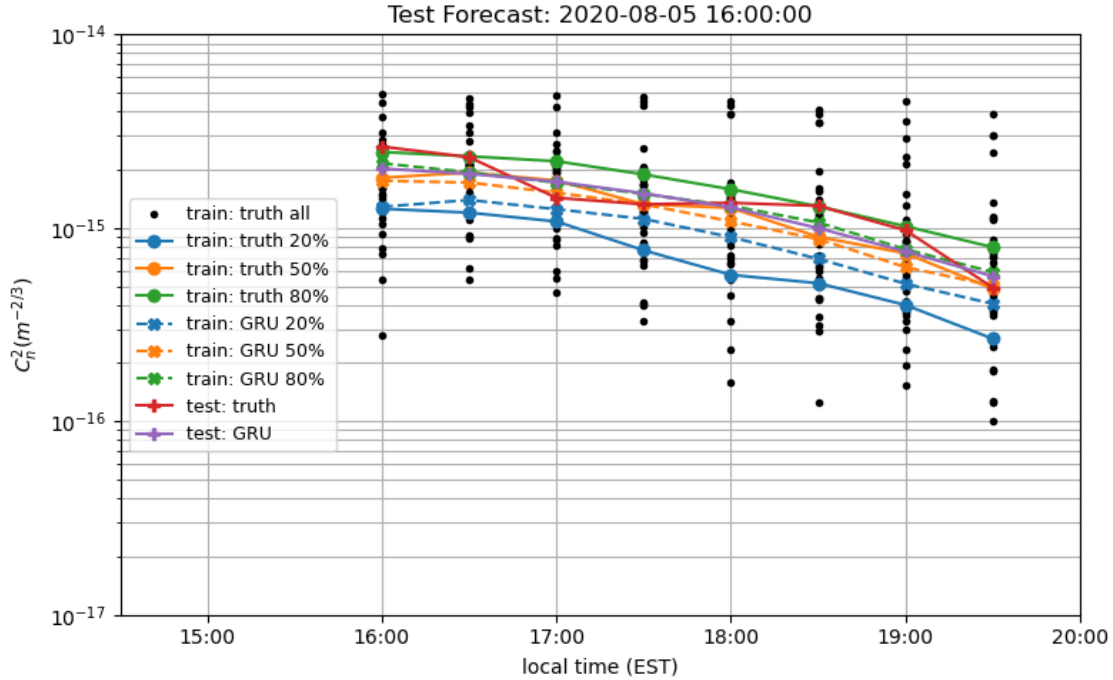


Figure 5.10: GRU-RNN performance analysis of the August 5th 16:00 EST forecast.

output CDF 80% values throughout the forecast, and the model forecast nearly overlays this same CDF line. Since the measurements are within the bounds of the model’s learned relationship, and the model has correctly forecasted stronger conditions at this time of day, the model’s performance is quantified as good.

## 5.5 Chapter Summary

This Chapter began by training an ensemble of ten models (the best GRU-RNN model) on the combined train and validation dataset, then applying the models to the test dataset. In Figure 5.1 it is shown that model performance as applied to the entire test dataset is consistent. Figure 5.2 shows model performance is quite variable by date, but performance on each date is highly consistent. Figure 5.3 illustrates the model is best in the middle of

the day, has moderate performance in the morning, and is generally worst in the evening. An ensemble of the best MLP model was also trained and compared with the GRU-RNN model. This comparison further confirmed selection of the GRU-RNN model.

The following sections illustrated model forecasts for the seven test days and analyses were presented. These analyses have resulted in an understanding of where and why the model performs well and poorly. Capturing the depth of evening neutral events is a common issue with this model as illustrated by the daily- $C_n^2$  plots in Figures 5.4 and 5.5, and by the scatter plots in Figure 5.6. The analysis of the August 9th 18:00 EST forecast, an extreme example, shows that the model has generally learned to forecast an evening neutral event from this time, but only is able to forecast a limited range of  $C_n^2$  strengths. In the analysis of the mid-day conditions on August 6th 14:00 EST in Figure 5.9 it is shown that the model has learned to forecast similar  $C_n^2$  strengths mostly around  $2 \times 10^{-15}(m^{-2/3})$  with a very narrow window. Significant deviations, like high frequency weather induced events, are difficult to forecast and is missed entirely in the case of the August 6th 14:00 EST forecast analysis. Finally, in Figure 5.10 is has been shown that the model performs very well when the forecast predicts a smooth transition of  $C_n^2$  conditions which is the case for many of the forecasts in the test dataset.

## CHAPTER VI

### SUMMARY AND FUTURE WORK

#### 6.1 Summary

This thesis has meticulously stepped through the process of training a machine learning turbulence ( $C_n^2$ ) model to forecast four hours of future turbulence conditions at 30-minute intervals from prior environmental measurements. The objective of this thesis, *forecasting* turbulence conditions, is novel, as is the approach. The technique uses a turbulence sensor and weather station deployed simultaneously for about two months, carefully formats the data into sequence/forecast pairs, then trains a recurrent neural network that is shown to accurately predict the general trend of future turbulence conditions from prior environmental measurements. The model struggles to capture turbulence events which significantly deviate from the diurnal trend. Even when the model is applied to the train dataset, a highly biased result, the model is not able to capture significant turbulence events.

The grid search resulted in the selection of the GRU-RNN model based on ensemble model performance with assistance from *Welch's t-test*. This result is consistent with the expectation that a RNN architecture is better than the MLP because it processes the input data as a time series. The model requires only 12 hours of prior weather and  $C_n^2$  measurements at 30-minute intervals. The best weather parameters for modeling turbulence (pressure, relative humidity, and solar irradiance) are from a station nearly 9 km away from the turbulence sensor platform. Despite this significant geographical separation the model is still able to learn the relationship between weather and turbulence conditions. The technique for filling nighttime turbulence measurements is a suitable method for retaining morning forecasts when nighttime measurements are not available. The model is effective

for a nine day test window given a very small dataset of only 1107 sequence/forecast pairs for training. Model training time is only a few seconds so computation requirements are minimal.

## 6.2 Future Work

This thesis proposed a novel idea and presented basic techniques to achieve its goal. For example, the nighttime filling of  $C_n^2$  measurements is a technique that appeared to be effective, but no other techniques were tested for improved performance. Another example is the initial hidden state of the RNN architectures. Initializing the hidden state  $h_0$  with zeros is the default behavior and the only initialization used in this thesis. The following is a comprehensive list of topics for future work encountered in this thesis.

- Improve data preprocessing techniques to fill small gaps in weather or  $C_n^2$  measurements. In this work a sequence/forecast pair was removed for any missing measurement. Filling small gaps with a technique like interpolation could retain many more training examples.
- RNN architectures can process variable-size input sequences. Analyze how model performance is impacted by input sequences with padded, interpolated, or missing inputs.
- Investigate how the model is impacted by input sequences that are beyond the dynamic range of the training examples. The dataset used in this work is nearly ideal because the test dataset is a great representation of the train dataset.

- Expand the grid search to iterate over many more hyperparameters like learning rate and learning rate decay, number of epochs, optimization algorithms, input variables, etc.
- Explore shorter (like 2 hour) and longer (like 8 hour) forecasts.
- Train a model on more data (like the last four months) and on less data (like the last two weeks) to analyze the data requirement for an effective model.
- Model  $C_n^2$  at specific DELTA bins (screens), like the first or second, to isolate the forecasting to a particular part of the propagation path.
- Analyze if a geographical separation between weather and  $C_n^2$  measurements has been learned by the model.
- The RNN was employed to process the input sequence as a time series, but the model output is simply the hidden RNN nodes fully-connected to eight output nodes which has no temporal processing. Use a recurrent architecture as the *output* to process the forecast as a time series.

## BIBLIOGRAPHY

- [1] R. Tyson, *Principles of Adaptive Optics*. Boca Raton, FL: CRC Press, 2011.
- [2] G. C. Valley, “Isoplanatic degradation of tilt correction and short-term imaging systems,” *Appl. Opt.*, vol. 19, no. 4, pp. 574–577, Feb 1980. [Online]. Available: <http://ao.osa.org/abstract.cfm?URI=ao-19-4-574>
- [3] C. Jellen, J. Burkhardt, C. Brownell, and C. Nelson, “Machine learning informed predictor importance measures of environmental parameters in maritime optical turbulence,” *Appl. Opt.*, vol. 59, no. 21, pp. 6379–6389, Jul 2020. [Online]. Available: <http://ao.osa.org/abstract.cfm?URI=ao-59-21-6379>
- [4] C. Su, X. Wu, T. Luo, S. Wu, and C. Qing, “Adaptive niche-genetic algorithm based on backpropagation neural network for atmospheric turbulence forecasting,” *Appl. Opt.*, vol. 59, no. 12, pp. 3699–3705, Apr 2020. [Online]. Available: <http://ao.osa.org/abstract.cfm?URI=ao-59-12-3699>
- [5] Y. Wang and S. Basu, “Estimation of optical turbulence in the atmospheric surface layer from routine meteorological observations: an artificial neural network approach,” in *Laser Communication and Propagation through the Atmosphere and Oceans III*, A. M. J. van Eijk, C. C. Davis, and S. M. Hammel, Eds., vol. 9224, International Society for Optics and Photonics. SPIE, 2014, pp. 300 – 307. [Online]. Available: <https://doi.org/10.1117/12.2063168>
- [6] A. Paszke, S. Gross, F. Massa, A. Lerer, J. Bradbury, G. Chanan, T. Killeen, Z. Lin, N. Gimelshein, L. Antiga, A. Desmaison, A. Kopf, E. Yang, Z. DeVito, M. Raison, A. Tejani, S. Chilamkurthy, B. Steiner, L. Fang, J. Bai, and S. Chintala, “Pytorch: An imperative style, high-performance deep learning library,” in *Advances in Neural Information Processing Systems 32*, H. Wallach, H. Larochelle, A. Beygelzimer, F. d’Alché-Buc, E. Fox, and R. Garnett, Eds. Curran Associates, Inc., 2019, pp. 8024–8035. [Online]. Available: <http://papers.neurips.cc/paper/9015-pytorch-an-imperative-style-high-performance-deep-learning-library.pdf>
- [7] C. Nwankpa, W. Ijomah, A. Gachagan, and S. Marshall, “Activation functions: Comparison of trends in practice and research for deep learning,” *CoRR*, vol. abs/1811.03378, 2018. [Online]. Available: <http://arxiv.org/abs/1811.03378>
- [8] J. Chung, Ç. Gülcühre, K. Cho, and Y. Bengio, “Empirical evaluation of gated recurrent neural networks on sequence modeling,” *CoRR*, vol. abs/1412.3555, 2014. [Online]. Available: <http://arxiv.org/abs/1412.3555>
- [9] S. Hochreiter and J. Schmidhuber, “Long Short-Term Memory,” *Neural Computation*, vol. 9, no. 8, pp. 1735–1780, Nov. 1997. [Online]. Available: <https://direct.mit.edu/neco/article/9/8/1735-1780/6109>

- [10] C. Olah, “Understanding lstm networks.” [Online]. Available: <https://colah.github.io/posts/2015-08-Understanding-LSTMs/>
- [11] K. Cho, B. van Merriënboer, C. Gulcehre, D. Bahdanau, F. Bougares, H. Schwenk, and Y. Bengio, “Learning phrase representations using rnn encoder-decoder for statistical machine translation,” 2014.
- [12] R. M, “The ascent of gradient descent,” Jun 2020. [Online]. Available: <https://blog.clairvoyantsoft.com/the-ascent-of-gradient-descent-23356390836f>
- [13] “Coding deep learning for beginners - linear regression (part 3): Training with gradient descent.” [Online]. Available: <https://towardsdatascience.com/coding-deep-learning-for-beginners-linear-regression-gradient-descent-fcd5e0fc077d>
- [14] I. Loshchilov and F. Hutter, “Decoupled weight decay regularization,” 2019.
- [15] D. P. Kingma and J. Ba, “Adam: A method for stochastic optimization,” 2017.
- [16] “Vantage Pro2 Plus Technical Specs.” [Online]. Available: \url{<https://www.davisinstruments.com/vantage-pro2/tech-specs/>}
- [17] “Atmospheric Characterization Devices.” [Online]. Available: \url{<https://www.mza.com/products.php?page=productsAtmosChar>}
- [18] C. R. Harris, K. J. Millman, S. J. van der Walt, R. Gommers, P. Virtanen, D. Cournapeau, E. Wieser, J. Taylor, S. Berg, N. J. Smith, R. Kern, M. Picus, S. Hoyer, M. H. van Kerkwijk, M. Brett, A. Haldane, J. F. del Río, M. Wiebe, P. Peterson, P. Gérard-Marchant, K. Sheppard, T. Reddy, W. Weckesser, H. Abbasi, C. Gohlke, and T. E. Oliphant, “Array programming with NumPy,” *Nature*, vol. 585, no. 7825, pp. 357–362, Sep. 2020. [Online]. Available: <https://doi.org/10.1038/s41586-020-2649-2>
- [19] W. H. Press, S. A. Teukolsky, W. T. Vetterling, and B. P. Flannery, *Numerical Recipes 3rd Edition: The Art of Scientific Computing*, 3rd ed. USA: Cambridge University Press, 2007.
- [20] P. Virtanen, R. Gommers, T. E. Oliphant, M. Haberland, T. Reddy, D. Cournapeau, E. Burovski, P. Peterson, W. Weckesser, J. Bright, S. J. van der Walt, M. Brett, J. Wilson, K. J. Millman, N. Mayorov, A. R. J. Nelson, E. Jones, R. Kern, E. Larson, C. J. Carey, İ. Polat, Y. Feng, E. W. Moore, J. VanderPlas, D. Laxalde, J. Perktold, R. Cimrman, I. Henriksen, E. A. Quintero, C. R. Harris, A. M. Archibald, A. H. Ribeiro, F. Pedregosa, P. van Mulbregt, and SciPy 1.0 Contributors, “SciPy 1.0: Fundamental Algorithms for Scientific Computing in Python,” *Nature Methods*, vol. 17, pp. 261–272, 2020.